

Nano-bioceramics : process routes and characterization

Xu, Jinling

2006

Xu, J. (2006). Nano-bioceramics : process routes and characterization. Doctoral thesis,
Nanyang Technological University, Singapore.

<https://hdl.handle.net/10356/5432>

<https://doi.org/10.32657/10356/5432>

Nanyang Technological University

Downloaded on 20 Mar 2024 17:37:39 SGT

NANO-BIOCERAMICS: PROCESS ROUTES AND CHARACTERIZATION



XU JINLING

**SCHOOL OF MECHANICAL AND AEROSPACE ENGINEERING
NANYANG TECHNOLOGICAL UNIVERSITY**

2006

Nano-Bioceramics: Process Routes and Characterization

Xu Jinling

School of Mechanical and Aerospace Engineering

**A thesis submitted to Nanyang Technological University
in fulfilment of the requirement for the degree of
Doctor of Philosophy**

2006

Statement of originality

I hereby certify that the work embodied in this dissertation is the result of original research and has not been submitted for a higher degree to any other University or Institution.

Xu Jinling
(Signed)

April 2006

ABSTRACT

ABSTRACT

The present research was carried out to explore modified bioceramic materials with suitable bioactive properties for tissue bonding. The focus concerned improving bio-mechanical performance of the synthetic calcium phosphates especially hydroxyapatite (HA, $\text{Ca}_{10}(\text{PO}_4)(\text{OH})_2$). To attain this purpose, suitable processing techniques were pre-requisite. Nano-structured HA doped with 0, 1, 3, and 5 weight % of a secondary silica (SiO_2) was produced using spray drying and/or radio frequency (RF) induction plasma spraying techniques. A spark plasma sintering (SPS) system was employed to obtain dense bioceramic with enhanced bio-mechanical properties. *In vitro* investigation of the sintered bioceramic disks revealed bioactive behavior inherent of its original powder characteristic.

The starting HA slurry was synthesized through a wet chemical reaction method, which was followed by a spray drying process. These spray dried powders were subsequently processed in a RF induction plasma. A systematic study was performed to analyze the properties of these RF plasma synthesized powders. The results showed that the working plate power levels of the RF plasma system were the major influence on the decomposition of the feedstock into alpha-tricalcium phosphate (α -TCP, $\text{Ca}_3(\text{PO}_4)_2$), tetra-calcium phosphate (TTCP, $\text{Ca}_4\text{P}_2\text{O}_9$), calcium oxide (CaO), and/or amorphous calcium phosphate. An increase in working plate power from 15 kW to 21 kW led to different trends of the decomposition of the HA feedstock in the flame. The obtained powders experienced significant decomposition at 15 kW and 21 kW; with

ABSTRACT

other working parameters kept constant whereas there was relatively moderate decomposition at the working power level of 20 kW. This was attributed to the combined influence of the plasma flame temperature and flame velocity. Nano sized powders from the RF plasma processing were found to agglomerate. The particle size of the powder was in the range of 10-100 nm. Rietveld refinement results indicated that there was about 75 weight % of amorphous phase in the nano-sized CaP powders. After heat treatment at 800 °C for 3 hrs in air, the amorphous phase crystallized mainly into beta dicalcium pyrophosphate (β -Ca₂P₂O₇). This was attributed to the extreme decomposition of the starting HA during the RF plasma processing that rapidly solidified into amorphous phase.

The densification behavior of these powders was investigated through a SPS system and a dilatometer. The results demonstrated that starting powders were effectively sintered to high densities within several minutes. The nano particles first coalesced together, and then the micron sized particles sintered at higher temperature. The powder morphology and the aggregation were the two key factors controlling sintering behavior. The characteristics exhibited by the agglomerate powders were closely related to the powder processing techniques.

The results indicated that the presence of doped amorphous silica introduced the decomposition of HA into other phases after RF plasma and/or SPS steps. Raman spectra, lattice parameters and XPS results proved the possibility of silicate substitution in these biomaterials.

ABSTRACT

An *in vitro* study was conducted to evaluate the biological properties regarding bone-like apatite formation and osteoblast cell adhesion of these SPS compacts. In the simulated body fluid environment, these sintered compacts showed excellent bioactivity by inducing an apatite layer on their surfaces under physiological conditions. The different dissolution rate of calcium phosphate resulted in the precipitation of apatite. These apatite crystals grew on (0001) planes. Their c-axes were approximately consistent with the assembled state of bone. This finding implied that the biomineralization could be highly regulated by this assembled crystallographic directions. The investigation of relationship between the cell response and the ceramic surfaces indicated that osteoblasts displayed cellular attachment and proliferation on the ceramic surfaces. Furthermore, the results indicated that the surface chemistry contributed primarily to the cellular attachment. The *in vitro* cell culture results also indicated that the presence of silica in apatite enhanced the cell proliferation and differentiation rates due to the soluble silicate compared with those samples without doping silica.

In summary, this study concentrated on the assessment of nano-structured biomaterials that experienced RF plasma processing and spark plasma sintering. Characterization was carried out on the microstructure, chemical compositions, thermal analysis, bio-mechanical properties, sintering and *in vitro* analysis. Furthermore, recommendations for further study on these new biomaterials were presented.

Acknowledgements

Firstly, I would like to express my sincere gratitude to my supervisor - ***Prof. Khor Khiam Aik*** for his kind guidance, patience and encouragement throughout my PhD study on this project. He gave me a lot of valuable suggestions and comments in progressing this project and writing this thesis, and his wisdom and knowledge will last forever in my life!

I would also like to be grateful to the research members in Prof. Khor's group - ***Dr. Yu Ligen, Dr. Li Hua, Dr. M.E. Pons, and Dr. Chen Xiaojun*** for their valuable discussions and suggestions on my study.

I appreciated ***Dr. Yu Ligen*** for his kind and patient discussion, suggestions and corrections for my PhD thesis.

Dr. Rajendra Kumar is acknowledged for his kind and valuable discussion, suggestions and analysis.

Thanks to ***Dr. Dong Zhili*** for his advice, cooperation and willingness to help me on HR TEM.

Special thanks to ***Dr. Gu Yanwei***, for her kind assistance in the operation of RF plasma system and characterization at SIMtech.

Thanks also extend to the technicians in Materials Lab of MAE for their cooperation and assistance. Without them, this project could not proceed smoothly.

Special thanks to my husband-Mr. Wang for his encouragement during my study! My parents and my sisters are also appreciated for their encouragement throughout my work! Thank you!

Table of contents

Chapter 1 Introduction.....	1
1.1 Background	1
1.2 Objectives.....	3
1.3 Scope	4
Chapter 2 Literature Review	6
2.1 Introduction	6
2.1.1 Bone structure.....	8
2.1.2 Implant materials	8
2.2 Properties of hydroxyapatite	11
2.3 Application of hydroxyapatite.....	15
2.3.1 HA for surface modification of implant substrate	15
2.3.2 Production of HA compacts	17
2.3.3 Production of HA powders	20
2.3.3.1 Wet chemical synthesis of HA.....	21
2.3.3.2 Spherical HA powders	23
2.4 Production of Nano-structured HA	25
2.5 Problems involved with high temperature processed HA	29
2.6 Post deposition heat treatment.....	32
2.7 Modified calcium phosphate	33
2.8 <i>In vitro</i> tests	37
2.8.1 Simulated body fluid	38
2.8.2 Cell culture	39
2.9 Summary	40
Chapter 3 Experimental Techniques	41
3.1 Spray drying system	41
3.2 RF induction plasma system	42
3.3 Spark Plasma Sintering system	44
3.4 Dilatometer system.....	45
3.5 X-ray Diffraction analysis	46
3.6 Scanning Electron Microscopy	47
3.7 Transmission Electron Microscopy.....	47
3.8 Raman Spectrometry	48
3.9 Differential Scanning Calorimetry	50
3.10 Micro-indentation test.....	50
3.11 <i>In vitro</i> tests	52
3.11.1 Simulate body fluid.....	52
3.11.2 Cell culture.....	55
3.12 Other analysis	57
Chapter 4 Production of HA and Silica doped HA (SiHA) Feedstock.....	58
4.1 Preparation	59
4.2 Results	60

4.2.1	Phase compositions of the powders	60
4.2.2	Raman spectra.....	62
4.2.3	Morphology and size distribution.....	65
4.2.4	TEM analysis	67
4.3	Discussion	68
4.3.1	Reaction conditions for Stoichiometric HA	68
4.3.2	Structural and compositional study of the powders.....	69
4.3	Chapter summary	72
Chapter 5 Production and characterization of radio frequency plasma synthesized calcium phosphate powders.....		73
5.1	Production of radio frequency plasma CaP powders	74
5.2	Characterization of RF plasma processed spherical powders	75
5.2.1	Results	75
5.2.1.1	Morphology analysis and particle size analysis.....	75
5.2.1.2	Phase composition studies	78
5.2.1.3	Heat-treatment effect	80
5.2.2	Discussion.....	84
5.2.2.1	RF plasma processing	84
5.2.2.2	Phases and structure analysis	88
5.3	Characterization of nano RF plasma synthesized powders.....	92
5.3.1	Results	92
5.3.1.1	Morphological analysis.....	92
5.3.1.2	XRD analysis	95
5.3.1.3	HR TEM results	98
5.3.1.4	Thermal analysis	101
5.3.2	Discussion.....	103
5.3.2.1	XRD analysis	103
5.3.2.2	Phases contents	105
5.3.2.3	HR TEM analysis.....	108
5.3.2.4	Thermal analysis	111
5.4	Chapter summary	113
Chapter 6 Spark plasma sintering of RF plasma synthesized and spray dried calcium phosphate powders		114
6.1	Preparation of SPS samples.....	115
6.2	Characterization of SPS RF plasma processed HA powders	116
6.2.1	Results	116
6.2.1.1	XRD and Raman analysis	116
6.2.1.2	Fracture surfaces analysis	119
6.2.1.3	SEM images after polishing.....	121
6.2.1.4	Shrinkage behavior of SPS samples	125
6.2.2	Discussion.....	129
6.2.2.1	Spark plasma sintering behaviors	129
6.2.2.2	Phases analysis.....	131
6.3	SPS of silica doped HA (SiHA)	134

6.3.1	Results	135
6.3.1.1	Phases analysis of SPS SiHA.....	135
6.3.1.2	Effect of silica on densification of SiHA	139
6.3.1.3	Shrinkage behaviors.....	142
6.3.1.4	XPS analysis of silica doped CaP ceramics	145
6.3.2	Discussions	149
6.3.2.1	Sintering behaviors analysis	149
6.3.2.2	Phases analysis.....	150
6.4	Chapter summary	153
Chapter 7	Sintering behavior of RF plasma synthesized and spray dried calcium phosphate powders assessed by a dilatometer	154
7.1	Processing of samples	154
7.2	RF plasma processed powders	155
7.2.1	Results	155
7.2.1.1	Effects of sintering temperature	155
7.2.1.2	Effects of sintering duration and heating rates	161
7.2.1.3	Shrinkage behaviors	165
7.2.2	Discussion.....	168
7.3	Effect of silica to the densification	172
7.3.1	Results	172
7.3.2	Discussion.....	174
7.4	Chapter summary	177
Chapter 8	<i>In vitro</i> tests of SPS ceramic.....	178
8.1	In vitro tests through SBF	179
8.1.1	Results of SBF	179
8.1.2	Discussion of SBF	183
8.2	Cell culture	186
8.2.1	Samples' characterization.....	187
8.2.2	Cell culture results and discussion.....	188
8.2.2.1	Morphology of osteoblasts	188
8.2.2.2	Cell proliferation on SPS compacts from RF plasma processed powders	191
8.2.2.3	Effects of silica on the Cell proliferation and cell differentiation.....	193
8.3	Chapter summary	196
Chapter 9	General Discussion	198
Chapter 10	Conclusions and Recommendations	204
10.1	Conclusions	204
10.2	Recommendations	206
References.....		208

List of Figures

Chapter 1	
Figure 1.1	Project flow chart.5
Chapter 2	
Figure 2.1	Actual requirements of orthopedic applications..... 7
Figure 2.2	Crystal structure of HA. 12
Figure 2.3	(0001) plane of HA at $z=3/4$ 12
Figure 2.4	Phase diagram of $\text{CaO-P}_2\text{O}_5$ under a partial pressure of water $p(\text{H}_2\text{O})=500\text{mm}$ 14
Figure 2.5	Pulsed current flow through powder particles.....20
Figure 2.6	Schematic illustration of the wet chemical reaction method.....22
Figure 2.7	A proposed model for nano-sized powders production by RF plasma28
Figure 2.8	A proposed model for phase formation in plasma-sprayed HA coatings 31
Figure 2.9	A schematic shows the proposed mechanism facilitating the bonding of bone to certain implants.....38
Chapter 3	
Figure 3.1	A schematic of the spray dryer LT-8.....41
Figure 3.2	A schematic of the radio frequency induction plasma system.43
Figure 3.3	A radio frequency plasma flame43
Figure 3.4	Main components of the spark plasma sintering apparatus.....45
Figure 3.5	Load-displacement curves, showing the maximum indentation depth h_{max} and minimum indentation depth h_{min}51
Figure 3.6	A schematic representation of indentation showing various quantities used in the analysis.....51
Chapter 4	
Figure 4.1	XRD patterns: (a) silica precipitated; (b) spray dried powders doped with various dopant level of silica. 61
Figure 4.2	XRD pattern of spray dried HA powders after heat treatment at 850 $^{\circ}\text{C}$ in air for 1.5 hr. 62
Figure 4.3	XRD pattern of spray dried HA powders after heat treatment at 1000 $^{\circ}\text{C}$ in air for 5 hrs..... 62
Figure 4.4	Raman spectrum of synthesized spray dried HA powders after heat treatment 63
Figure 4.5	Raman spectra: (a) silica doped HA powders; (b) silica precipitated 64
Figure 4.6	SEM morphologies of SD HA (a-c); heat treated HA (d); Silica(e); 1 wt% SiHA (f) and 5 wt% SiHA (g) powders..... 66
Figure 4.7	Particle size distribution of spray dried HA powders.....67
Figure 4.8	TEM images of fragment from Spray dried HA powders (a) and the SAD of the HA(b).....67

Chapter 5

Figure 5.1	Morphologies of: (a) Spheroidized HA powders under SEM; (b) Hollow-structured powders under SEM; (c) Fine particles filtered from spheroidized powders under high magnification SEM; (d) Fine particles filtered from the spheroidized powders under TEM; (e) Cross-section of spheroidized powders under SEM; and (f) Particle size distribution of spheroidized powders.....	77
Figure 5.2	XRD results of spray dried HA powders and spheroidized HA powders	79
Figure 5.3	Raman spectra of spheroidized HA powders obtained at various working conditions.....	80
Figure 5.4	XRD results of RF plasma processed powders (20kW, 10rpm) with and without heat treatment at 850°C for 1.5hr.....	81
Figure 5.5	Raman spectrum of the heat treated RF plasma synthesized CaP powder which obtained at 20kW, 10 rpm.....	81
Figure 5.6	HRTEM views of RF plasma synthesized powders after heat treatment at 850°C for 1.5 hrs.	83
Figure 5.7	SEM images of broken particles after RF plasma processing.....	85
Figure 5.8	Phase contents in spheroidized HA powders obtained from various working conditions.....	91
Figure 5.9	SEM images (a-c) and TEM images (d-e) of nano HA powders obtained from RF plasma thermal spraying.....	94
Figure 5.10	XRD patterns of nano-sized powders after RF plasma processing at various working plate power level.....	96
Figure 5.11	XRD results of nano powders after heat treatment at 800 °C for 1.5 hr in air, the nano powders are obtained under various working conditions.....	97
Figure 5.12	Nano domains within the nano sized powders after RF plasma processing.	99
Figure 5.13	An HRTEM image showing amorphous/HA phases interfaces in nano HA powders along [111] direction.....	99
Figure 5.14	(a) HA/amorphous interfaces in nano powders showing the unit cells of HA along c axis; (b) a schematic of atoms diffusion from liquid or amorphous to solid or crystalline phase.....	100
Figure 5.15	HRTEM images: (a) Distorted lattices;	100
Figure 5.16	DSC results: (a) nano-sized powders obtained at various working plate power levels, and the curve at 15kw shows two overlapped exothermic peaks; (b) spray dried HA feedstock.....	102
Figure 5.17	Fitting deviation of XRD pattern of 50% nano powders mixture with 50 weight % alumina powders with Rietveld analysis.	107
Figure 5.18	Phases contents in the nano sized powders.....	108
Figure 5.19	HRTEM images of nano powders (c-d), after heat treatment.....	110

Chapter 6

Figure 6.1	XRD results of SPS ceramics sintered at various temperatures.	117
Figure 6.2	Raman patterns of SPS compacts.	118
Figure 6.3	Fracture images of SPS compacts sintered at various temperatures for 3 min: (a)-(b)900°C; (c)-(d)1000°C;(e)-(f)1100°C;(g)-(h)1150°C; (i)-(j)1200°C	120
Figure 6.4	Etched optical morphology images of SPS ceramics sintered at: (a-b) 1000°C (c-d)1100°C, (e-f)1150°C, (g-h)1200°C	122
Figure 6.5	Low vacuum SEM morphologies of SPS samples after etching in nitric acid for 10 s: (a-b) 1000°C (c-d)1100°C, (e-f)1150°C, (g-h)1200°C at 34MPa for 5 min.	124
Figure 6.6	Elements mapping results of SPS ceramic sintered at 1000°C	125
Figure 6.7	Kinetic curves of rCaP ceramic in the SPS system at the heating rate of 20°C/min to 1200°C, duration at 1200°C for 10 min and then followed cooling to 600°C at 50°C/min.	127
Figure 6.8	Effect of sintering temperature on the sintered densities.	128
Figure 6.9	Effect of sintering temperature on Young's Modulus and Hardness of the sintered samples.	129
Figure 6.10	XRD patterns: (a) SPS ceramics doped with different amount of silica; (b) RF plasma processed HA powders doped with 1wt% of silica.	136
Figure 6.11	Raman spectra: (a) SPS ceramics doped with different amount of silica; (b) RF plasma processed HA powders doped with 1wt% of silica.	139
Figure 6.12	Fracture morphologies of SPS ceramics: (a) HA, (b) 1SiHA, (c) 3SiHA, and (d) 5SiHA.	140
Figure 6.13	Vickers Hardness (H) and Young's Modulus (E) of the SPS ceramics doped with different amount of silica.	142
Figure 6.14	Kinetic curves of spark plasma sintering: (a) RF plasma processed 1SiHA powders; (b) Spray dried 1SiHA powders.	143
Figure 6.15	SEM images of the powders used for SPS processing: (a) RF plasma processed prSi; and (b) spray dried p1SiHA.....	144
Figure 6.16	XPS spectra of SPS specimen sintered at 1000°C for 3 min.	145
Figure 6.17	Binding energies of P2p, Ca2p, O1s, Si2p and C1s in 3SiHA ceramic	148
Figure 6.18	A schematic illustration of primary particles (nanocrystalline), an agglomerate and packing of agglomerates.....	149

Chapter 7

Figure 7.1	SEM images of R15 sintered at (a)1100°C,(b)1200°C, (c)1300°C, and (d)1400°C.	159
Figure 7.2	XRD patterns of sintered of R15 powders in the dilatometer at various temperatures with a heating rate of 5 °C/min.....	160
Figure 7.3	Raman spectra of sintered of R15 powders in the dilatometer at various temperatures with a heating rate of 5°C/min.....	160

Figure 7.4	Microstructure images of R15 sintered at 1200°C under the heating rate of 5°C/min for: (a-b) 5 hrs, (c-d) 10 hrs; (e-f) 20hrs.....	162
Figure 7.5	Influence of the heating rate on the microstructures of the ceramics sintered at 1200°C for 5 hrs: (a) 10°C/min; (b) 20°C/min.	164
Figure 7.6	XRD patterns of the ceramic sintered at 1200 °C for 5 hrs under various heating rates.	164
Figure 7.7	Densification curves of R15 during heating to 1300°C: (a) shrinkage behavior; (b) densification rate.	167
Figure 7.8	Dilatometer results of green compacts with a heating rate of 5°C/min: densification behavior; (b) shrinkage rates.	174
Figure 7.9	Microstructures of 3SiHA (a) and SD HA (b) after sintered in the dilatometer.	176
Chapter 8		
Figure 8.1	Bone-like apatite layers on the surface of SPS samples sintered at 1100°C for 3 min after immersion various periods in SBF: (a) 0 days; (b) 1 day; (c) 3 days; (d) 1 week; (e) 2 weeks; (f) 4 weeks; and (g-h) high magnification of apatites.....	180
Figure 8.2	Thin film XRD patterns of apatite layers on SPS compacts sintered at 1100°C for 3 min after immersion for various periods in SBF...	181
Figure 8.3	The curves of Ca and P concentration versus immersion periods in SBF.	182
Figure 8.4	A schematic showing the formation of preferential apatite along [0001] on the SPS ceramic surface in the SBF.	186
Figure 8.5	SEM images of human osteoblast-like cells on the SPS disks.....	190
Figure 8.6	MTT results of the SPS disks after cell culture for 2 and 4 days, respectively. Cell seeding density: $2 \times 10^4/\text{cm}^2$	192
Figure 8.7	XRD patterns of SPS ceramic surfaces.	193
Figure 8.8	Relative osteoblast viability on the SPS disks doped with different amount of silica. Cell seeding density: $2 \times 10^4/\text{cm}^2$	194
Figure 8.9	Effect of silica to the relative secretion of AKP on the silica dope HA disks. Cell seeding density: $2 \times 10^4/\text{cm}^2$	196
Chapter 9		
Figure 9.1	HA powder becomes dense and spherical after treatment by RF induction plasma processing.	199
Figure 9.2	A selected area diffraction pattern of nano particles prepared in RF plasma.	200

List of Tables

Chapter 2

Table 2.1	Physical properties of HA.....	13
Table 2.2	Main properties of silicon/silica modified CaP compared to pure HA..	36
Table 2.3	Description of different approaches to fabricate silica/silicon modified HA	36

Chapter 3

Table 3.1	Typical Radio Frequency Plasma experimental conditions.....	44
Table 3.2	Compositions of the SBF solution with the comparison to human blood plasma	53
Table 3.3	Reagents required for preparing 1 liter of simulated body fluid (SBF)	54
Table 3.4	Components in the cell culture medium for osteoblast propagation ...	55

Chapter 5

Table 5.1	Particle size distribution of RF plasma synthesized CaP powders ($d_{0.1}$, $d_{0.5}$, $d_{0.9}$ refer to the measured particle size of 10%, 50% and 90% of the powder particles)	86
Table 5.2	Specific surface areas of the RF Plasma spheroidized CaP powders ...	88
Table 5.3	Quantification of the phases and crystallinity for the nano powders.....	107

Chapter 6

Table 6.1	Chemical analysis results of the powders and ceramic	118
Table 6.2	SPS ceramic feedstock and classification	135
Table 6.3	Lattice parameters of SPS compacts	137
Table 6.4	Phases fraction in the RF plasma processed silica powders	137
Table 6.5	Densities and relative densities of spark plasma sintering specimen. (Theoretical density of HA is 3.156 g/cm^3)	141
Table 6.6	Particle size distribution of the r1SiHA and 1SiHA powders ($d_{0.1}$, $d_{0.5}$, $d_{0.9}$ refer to the measured particle size of 10%, 50% and 90% of the powder particles).	145
Table 6.7	Binding energies obtained from XPS of prSi and SiHA ceramics.	147

Chapter 7

Table 7.1	Densities of the ceramics various sintering conditions	163
-----------	--	-----

Chapter 8

Table 8.1	Powder feedstock used and surface roughness of SPS ceramic	187
Table 8.2	Surface energies of various SPS ceramic	188

Symbols and Abbreviations

Symbols

A	Contact area
S	Contact stiffness
R_a	Roughness
R_{wp}	The residual being minimized in Rietveld analysis
R_{exp}	The expected value in Rietveld analysis model
C	Measured compliance
$^{\circ}C$	Centigrade
E	Young's modulus
E_r	Reduced modulus
E^*	Apparent elastic modulus
P_{max}	Peak indentation load
R	Indenter radius
d	Average grain size
h	Depth of the elastic penetration of the indenter
h_c	Contact depth
(hkl)	Crystal plane indice, $i=-(h+k)$
(hkl)	Crystal plane indice
$[hkl]$	Crystal orientation, $i=-(h+k)$
$[hkl]$	Crystal orientation
h_{max}	Maximum depth at peak indentation load
h_{min}	Minimum depth
i	Subscript referring to the indenter
α	Alpha
β	Beta
ρ	Density
λ	X-ray wavelength
ν	Poisson's ratio
θ	Bragg angle
σ_i	Yield stress
σ_0	Friction stress
k_y	Stress intensity factor

Abbreviations

ACP	Amorphous calcium phosphate
AKP	Alkaline phosphatase
BET	Brunauer-Emmett-Teller
CaO	Calcium oxide
CaP	Calcium phosphate
CCD	Charge coupled device
DC	Direct current
DMEM	Dulbecco's Modified Eagle's Medium

Symbols and Abbreviations

DNA	Deoxyribonucleic acid
DSC	Differential scanning calorimetry
FBS	Fetal bone bovine serum
FWHM	Full width at half-maximum of a diffraction peak
FTIR	Fourier transformation infrared
GOF	Goodness-of-fit
H	Hardness
HA	Hydroxyapatite
HMDS	Hexamethyldisilazane
HR TEM	High resolution transmission electron microscopy
ICP	Inductively coupled plasma
IPVS	Induction plasma vacuum spraying
IR	Infrared
J	Joule
JCPDS	The Joint Committee on Powder Diffraction Standards
K	Kilo, 1000
M	Mole per liter
MTT	Methylthiazoltetrazolium
N	Newton, unit of force
OA	Oxyapatite
OHA	Dehydroxylated hydroxyapatite
Pa	Pascal, unit of pressure equal to one Newton per square meter
PBS	Phosphate buffered saline
PFVD	Plasma flash vaporization and deposition
PMMA	Polymethylmethacrylate
QPA	Quantitative Phase Analysis
RF	Radio frequency
SAS	Selected area diffraction
SBF	Simulated body fluid
SEM	Scanning electron microscopy
SiHA	Silica doped hydroxyapatite
SPS	Spark plasma sintering
TEM	Transmission electron microscopy
TCP	Tricalcium phosphate
TTCP	Tetracalcium phosphate
XPS	X-ray photoelectron spectroscopy
XRD	X-ray diffraction
cm	Centimeter
deg	Degree
eV	Electron-volt
g	Gram
hr	Hour
nm	Nanometer
m	Meter
mA	Milliampere
min	Minute
mJ	Millijoule
ml	Milliliter
kW	Kilowatt

Symbols and Abbreviations

ppm	Part per million
rpm	Rotations per minute
rCaP	RF plasma sprayed calcium phosphate powders
s	Second
vol	Volume
wt	Weight

PUBLICATIONS (In chronological order)

1. **J.L. Xu**, R. Kumar, K.A. Khor, P. Cheang. Materials Research Society Symposium - Proceedings, v 777, 2003, p 171-176, Amorphous calcium phosphate nano-powders made from radio frequency (RF) plasma spraying.
2. K.A. Khor, **J.L. Xu**, L.G. Yu, P. Cheang. Proceedings of Materials Processing for properties and performance, 8-13 October, 2003, Yokohama, Spark Plasma Sintering of the Bimodal sized HA powders produced by Radio Frequency (rf) plasma.
3. **J.L. Xu**, K.A. Khor, Z.L. Dong, Y.W. Gu, R. Kumar, P. Cheang. Materials Science and Engineering A, 15(2004), p 101-108, Preparation and characterization of nano-sized hydroxyapatite powders produced in a radio frequency (rf) thermal plasma.
4. **J.L. Xu**, K.A. Khor, Y.W. Gu, Cheang, P. Proceedings of the International Thermal Spray Conference, Proceedings of the International Thermal Spray Conference, 2004, p 843-845, Inductively coupled plasma processing of nano-sized calcium phosphate powders.
5. **J.L. Xu**, K.A. Khor, Y.W. Gu, W.M. Soon, P. Cheang. Proceedings of Materials Processing for properties and performance, 24 – 26 November, 2004, Singapore, Spark Plasma Sintering and *In Vitro* Study of RF Plasma Processed HA powders.
6. **J.L. Xu**, K.A. Khor, P. Cheang. Proceedings of International Conference on Advanced Materials Processing, 29 November--1 December 2004, Melbourne, Spark Plasma Sintering of Silica-doped Hydroxyapatite.
7. **J.L. Xu**, K.A. Khor, Y.W. Gu, R. Kumar, P. Cheang. Biomaterials, 26(2005), p 2197-2207, Radio frequency (rf) plasma spheroidized HA powders: powder characterization and spark plasma sintering behavior.
8. **J.L. Xu**, K.A. Khor, R. Kumar, P. Cheang; Bioceramics, 18(2005), p511-514, RF induction plasma synthesized calcium phosphate nanoparticles.
9. K.A. Khor, L.G. Yu, **J.L. Xu**, P. Cheang; Transactions - 7th World Biomaterials Congress, Transactions - 7th World Biomaterials Congress, 2004, p 240, Spark Plasma Sintering (SPS) of nanostructured hydroxyapatite and flame-modified hydroxyapatite.
10. **J.L. Xu**, K.A. Khor, L.G. Yu., P. Cheang; Proceedings of 4th Materials Processing for properties and performance, Tsukuba, Japan, 28 November- 1 December, 2005, p87-89, Effects of silica on the densification behavior of hydroxyapatite.

11. **J.L. Xu**, K.A. Khor, R. Kumar, P. Cheang; Proceedings of 1st Asian thermal spray conference, Nagoya, Japan, November, 2005, p28-29, Nano-particles of calcium phosphate synthesized through radio frequency (rf) plasma spray.
12. **J.L. Xu**, K.A. Khor, S.Y. Teo, P. Cheang. The effects of sintering temperature and duration on RF plasma processed HA powders. Materials Science and Engineering A, to be published.
13. **J.L. Xu**, K.A. Khor, P. Cheang, W. Chen, Y. Kadarusman, Y.W. Lu, Y.W. Gu. Characterization of silica doped hydroxyapatite ceramics obtained from spark plasma sintering process. Acta Biomaterialia, to be published.
14. **J.L. Xu**, K.A. Khor, R. Kumar, S.Y. Teo, P. Cheang. Effects of pressureless sintering parameters on RF plasma processed calcium phosphate powders. Journal of Biomedical Materials Research, to be published.
15. **J.L. Xu**, R. Kumar, K.A. Khor, P. Cheang. Investigation of decomposition during RF plasma synthesis of calcium phosphate nanoparticles; Journal of Biomedical Materials Research Part A, to be published.
16. **J.L. Xu**, K.A. Khor, R. Kumar, X.Q. Go, P. Cheang. Investigation of spark plasma sintering temperature effects on microstructure and mechanical properties of titanium oxide, to be published.
17. **J.L. Xu**, K.A. Khor, Y.W. Lu, W.N. Chen, R. Kumar, P. Cheang. Osteoblast Interactions with calcium phosphate and silica doped apatite ceramics prepared by spark plasma sintering. Biomaterials, to be published.
18. **J.L. Xu**, K.A. Khor, R. Kumar, Y.W. Gu, P. Cheang; *In vitro* analysis of RF plasma processed nano-structured CaP particles sintered by spark plasma sintering route. Journal of biomedical materials research, to be published.

Chapter 1 Introduction

1.1 Background

A biomaterial may be a natural or man-made material and may comprise a whole or part of living structure or a biomedical device that performs, augments, or replaces a natural function [1]. The ideal biomaterials should have appropriate mechanical properties. The surface should have good biocompatibility in the sense of not producing any inflammatory tissue reaction. Synthetic biomaterials for tissue repair function physically and/or biologically in intimate contact with living hard or soft tissue. They are generally non-vital and sometimes of poor bonding with the host tissue [2].

Bioceramic materials are the main material sources that provide biological tissue-integration in tissue defects in situ. Calcium phosphates have been widely studied as bone scaffold biomaterials and this is because bone mineral has a similar chemical composition to synthetic HA. HA exhibits high levels of bioactivity and biocompatibility, which is characterized by the acceptance of the implant by the tissues [3]. However, though the Ca/P ratio of HA is close to the Ca/P found in fully mature bone [3], HA is not a complete model for bone mineral. Compared with biological bone, it is difficult for the clinical use of HA when used as a load bearing implant, since it does not offer sufficiently mechanical strength and appropriate pore size. There is evidence that natural bone contains other calcium phosphate species and subtle but significant chemical elements such as magnesium, carbonate and silicate. These elements help natural bone exhibit a higher bioactivity and mechanical properties compared with the synthetic HA.

Along with the advances in clinical applications, attention has focused on the formation of biomaterials similar to that of physiological bone with respect to chemical and bio-mechanical properties. This new biomaterial should also have enhanced physical, chemical and biological functions.

Grain size reduction has become an important approach in the pursuit to improve the mechanical properties [4]. The nano-structured material allows efficient deformation mechanism and crack dissipation that is an important factor in the application of HA [5]. Also, it has been proven that nano-structured HA has great biological efficacy [6]. The natural bone is actually made of nano-sized HA and fibers. Design of biomaterials with surface properties similar to natural bone (characterized by surface grain sizes in the nanometer regime) would undoubtedly aid in the formation of new bone at the tissue/biomaterial interface, and improve orthopedic/dental implant efficacy. A novel silicon doped calcium phosphate bulk ceramic is conducive to both osteoblast deposition and osteoclast resorption, allowing it to participate fully in the bone remodeling processes of the body.

A RF induction plasma spray technique was used to produce nano-structured powders. Compared with the conventional DC plasma system, the main advantage of the RF plasma is its large plasma flame that enhances the efficiency of nano-sized particle production. The ability to operate without the presence of any electrode is another advantage, which enables nano particles to be obtained as pure as the raw materials without suffering contamination from the erosion of the electrode.

An SPS system has been developed for fabricating fully dense ceramics at low temperature in short soaking time. With the SPS method, starting powders in a graphite die are pressed uniaxially. A DC pulse voltage is applied. At the early stage of

the sintering, the powders are heated by a spark discharge between the particles. The microscopic electric discharge enables processing conditions to form fine-grained ceramics with less thermal decomposition compared with conventional sintering steps.

Calcium phosphate materials implanted into bone defects bond spontaneously to living bone by the formation of a bone-like apatite layer on their surfaces. Osteoblast cells are then activated on this formed layer. This biological performance of bioceramic implants has been evaluated through *in vitro* assessments. It has been confirmed [5, 6] that the formation of the bonelike apatite layer can be reproduced in a SBF with ion concentrations almost equal to those of the human blood plasma. Moreover, this layer has been demonstrated, *in vitro*, to promote the adhesion of extracellular matrix, and stimulate cellular activity, and positively influence bonelike cell proliferation and differentiation. The chemical composition and structure of the implanted materials play an important role in the *in vitro* performance.

This project aims to produce new nano-structured CaP with high bioactivity and acceptable mechanical properties, which requires a precise knowledge of the characteristics of the bioceramic including the nature of starting materials and processing methods.

1.2 Objectives

The objectives of this thesis are listed below:

- To produce and characterize spray dried HA and silica doped HA powders (0, 1, 3, and 5 weight %) as the feedstock for RF plasma processing and/or spark plasma sintering.

- To produce and evaluate nano structured CaP powders using a RF induction plasma technique under different working conditions. Two main working parameters were selected to study the influence on the plasma processed powders: the working plate power level was set in the range of 15-21 kW; and the powder feed rate was set at 5 rpm (2.5 ± 0.1 g/min, calculated) and 10 rpm (5.4 ± 0.2 g/min, calculated), respectively.
- To demonstrate the densification mechanism of the CaP powders using a SPS system and a dilatometer. The working parameters such as: temperatures, heating rates, and durations, were selected to evaluate the densification behavior.
- To produce and characterize silicon substituted apatite using RF plasma and/or SPS systems. Different characterization techniques were employed to analyze the possibility of silicate substitution in phosphate.
- To analyze the biological performance of the SPS ceramic through *in vitro* tests. The bioactivities were tested in SBF. The osteoblast differentiation and proliferation were examined thoroughly.

1.3 Scope

This thesis aimed to provide an evaluation and discussion from the structural, morphological, thermal, bio-mechanical and bioactive points to study the RF plasma processed powders and SPS CaP ceramic samples. The topics covered in the present study were illustrated in Figure 1.1.

The starting HA was obtained in the form of a slurry through a wet chemical reaction. Various amounts of silica were doped into the starting HA slurry. The formed slurry was then spray dried into powders. These spray dried powders were processed

through a RF plasma system. A spark plasma sintering system was used to sinter these RF processed and spray dried CaP powders. The powders and SPS ceramic samples were characterized by advanced methods such as XRD, Raman spectroscopy, and TEM. The shrinkage behavior of these powders was extensively investigated. The biological properties of the SPS ceramic were studied through *in vitro* tests. The silicate substitution possibility in the apatite structure was evaluated through an XPS.

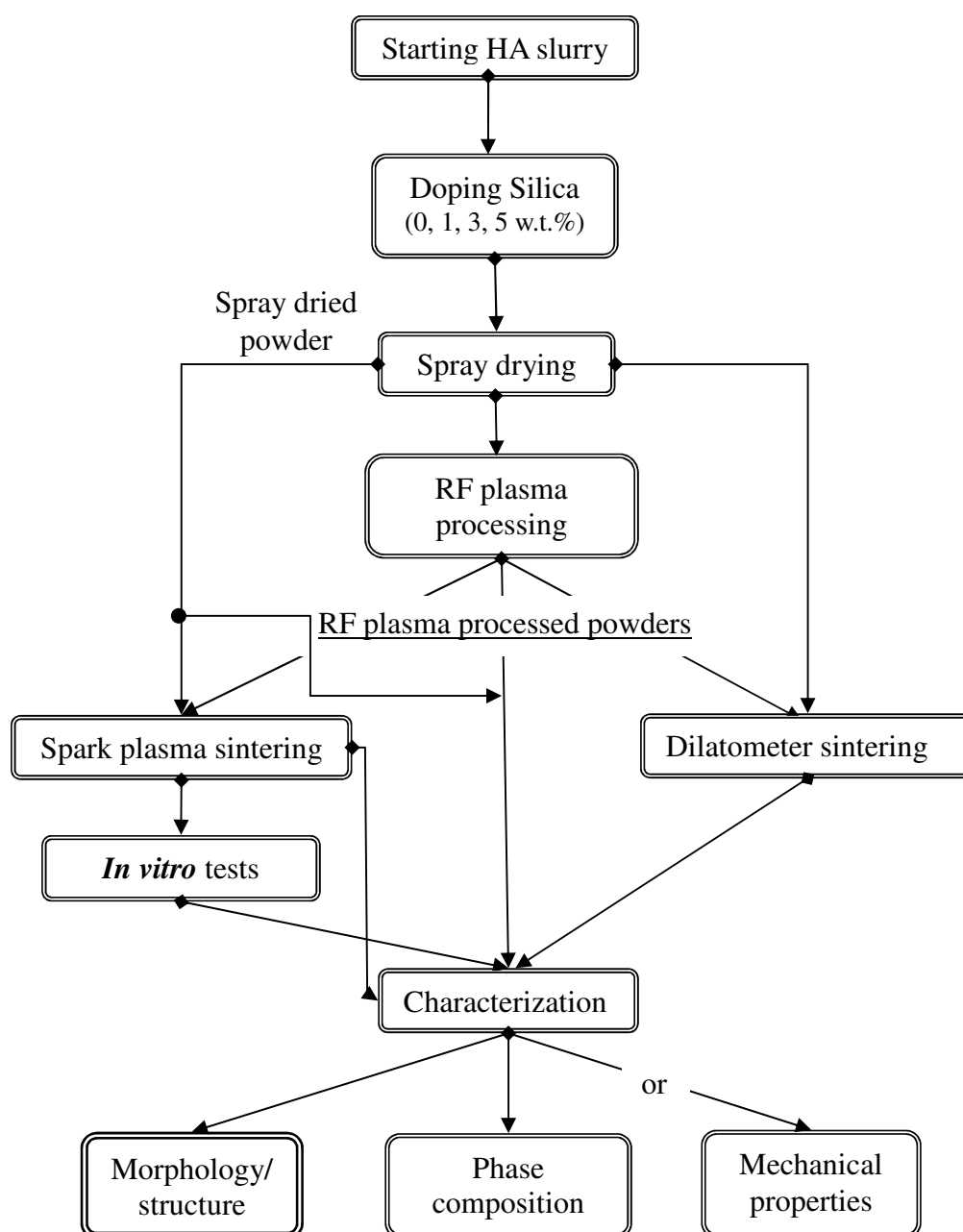


Figure1.1 Project flow chart.

Chapter 2 Literature Review

2.1 Introduction

Attempts have been made to find suitable materials to repair or replace any deficient tissue or body organ throughout the history of mankind. With the development of modern science, biomaterials have attracted increasing attention especially in the replacement of body parts. It is defined [1] that a biomaterial is a nonviable material used in a medical device and intended to interact with a biological system. Another definition of biomaterials is “either naturally occurring materials in living organisms or materials designed to repair humans” [1].

Since a biomaterial is a material in contact with fluids, cells and tissues of the living body utilized to evaluate, repair or replace any tissue or organ of the body [4], a prerequisite for any synthetic materials implanted in the body is that it should have good mechanical strength, high chemical stability, high corrosion resistance, very low toxicity and high biocompatibility [4]. The main requirements for the biomaterials are summarized in Figure 2.1.

Biomaterials can be classified into four distinct categories based on their specific tissue response. They are: bioinert, bioactive, bioresorbable, and biodegradable [5]. Bioinertness implies a minimal interfacial response between the implants and tissue. A bioinert material does not actively encourage bone growth. Thus, it does not result in tissue bonding or rejection. A bioactive material, instead, releases ions into its environment thereby influencing bone remodeling in the adjacent tissues. Its interfacial response results in tissue bonding. It has also been defined as a material being designed to induce specific biological activity [6]. Bioresorption is a continuous removal process of ions from the material through cell activity and/or through

dissolution when placed in the biological environment. Biodegradation is the gradual breakdown of a material mediated by specific biological and/or biochemical activity.

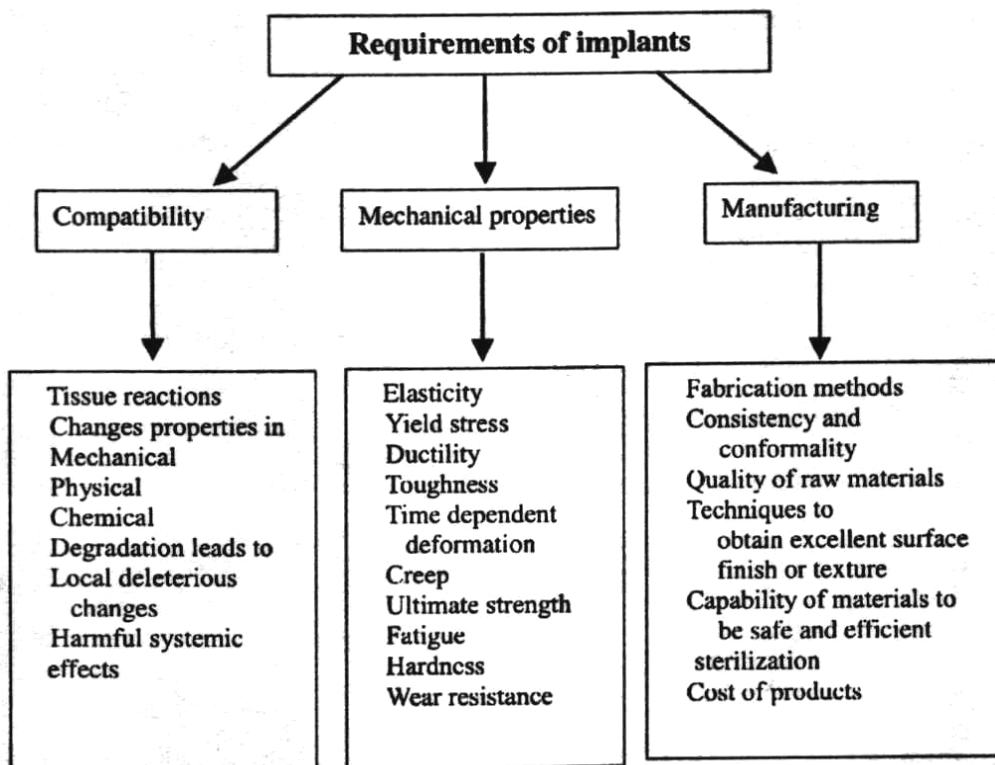


Figure 2.1 Actual requirements of orthopedic applications [1].

Biomaterial provides an alternative approach in the treatment of bone defects, with initial emphasis placed on the replacement of the missing tissue with biomaterials designed to induce minimal or no immune response. Bioactive implants normally act as a scaffold for cells, enabling them to anchor, attach and differentiate. It is critical for the development of new bone substitute materials to have precise knowledge of the physical, chemical and mechanical properties of bone and implanted materials.

2.1.1 Bone structure

Bones are organs composed of hard living tissue that serves as scaffold providing structural support to the body. They comprise a hard matrix of calcium salts deposited around protein fibers [3]. Minerals make bone rigid, and proteins (collagen) provide strength and elasticity.

Human bone contains three main kinds of cells (osteoblasts, osteocytes, and osteoclasts), mineralized extracellular matrix (65 wt%, hydroxyapatite and tricalcium phosphate), and organic extracellular matrix (35 wt%, collagen I and non-collagenous proteins such as osteocalcin, osteopontin and growth factors). The structural-functional unit of bone is an osteon, a microscopic system of osseous tubes (cylinders) inserted in one another. In the center of the system, there is a nutrient canal 10 to 100 μm in diameter, containing a blood capillary [3].

2.1.2 Implant materials

Metals such as titanium, titanium alloys, stainless steel, and cobalt-chromium based alloys are popularly used as implant materials because of their superior properties in terms of static and dynamic mechanical strength. In the past few years, researchers have been trying to develop a new series of materials that could guarantee not only superior mechanical performance but also an excellent biological response. For this purpose, different materials have been produced to meet almost every conceivable need. However, problems related to cell migration distance, breakage, stress shielding, reactivities and growth restriction are still unsolved [7]. In addition, the problem of ion release from the metallic substrate to the surrounding tissues exists when they are used in the corrosive environment of the human body.

Ti-6Al-4V alloys [8] show many desirable features, such as biocompatibility, high corrosion resistance, and excellent strength-to-weight ratio. They have been widely used in orthopedic applications. Their corrosion resistance can be attributed to a passivation layer that is formed on the surface. However, the layer can be easily worn away. Wear-corrosion failure can occur because of electric cell reactions between the passivated layer and non-passivated one.

Polymers are widely used in medicine, and cover a broad field of applications [7]. In general, they have physical properties that are most similar to these of soft tissues or non-mineralized tissues. Bioresorbable polymer devices may offer good alternatives to metals in terms of cell adhesion, but the main drawback still remains in their inherent low strength. Moreover, many polymers lack of bioactivity and poor bonding strength with the bone tissue.

Composite materials consist of two or more chemically distinct phases [9]. The objective of a composite material is to combine the properties of both materials to achieve specific properties for a particular application. Generally two different types of composites are used for medical applications: fiber reinforced composites and particulate reinforced composites. The most common reinforcement materials are carbon fibers, poly fibers, bioceramics and glasses [10]. In the natural body environment, the composite retains its bioactive properties, while undergoing continuous physio-chemical degradation [11, 12].

A bioceramic [13] is defined as a ceramic used as a biomaterial, which is designed to achieve a specific physiological behavior for use as a material of construction for prosthetic devices or artificial internal organs. Bioceramics have good chemical stability and biocompatibility within the physiological environment. The compatibility

of bioceramics comes from the fact that they are composed of ions commonly found in the physiological environment (calcium, potassium, magnesium, sodium.) and of ions that have very limited toxicity in body tissue.

The application of bioceramics can be traced back to ancient Egypt [13]. Both filled and artificial teeth made by bioceramics have been found in the mouths of mummies. According to a dentistry book from the late 1700s, dental implantation and transplantation were already popular in the eighteenth century. In 1892, Dreesman [13] published a report on the use of plaster of Paris to fill bone defects. Almost 30 years later, Albee and Morrison were the first to report on the use of TCP to fill bone gaps. However, it was not until the 1960s that research into the application of ceramic as a bone replacement material increased, with osteoceramic (a composite ceramic of TCP and MgAl_2O_4) being one of the first to be proposed, and used successfully in experiments on dogs [13].

The common characteristic of bioactive ceramics (e.g., HA) is a time-dependent, kinetic modification on the surface that occurs upon implantation. According to Leonelli [14], when exposed to physiological solutions, bioactive HA forms an amorphous calcium-phosphate layer on the surface; this layer crystallizes into a biologically active hydroxycarbonate apatite layer in a few days. This phase is chemically and structurally equivalent to the mineral phase in bone and responsible for interfacial bonding.

2.2 Properties of hydroxyapatite

Natural bone is mainly composed of mineral nano-crystals, water and collagen fibers. A typical wet cortical bone [15] is composed of 22 wt % organic matrix, 69 wt

% mineral, and 9 wt % water. The chemical composition of HA is very similar to the mineral component of natural bone. It is known that HA can form strong biological bonds with bony tissue without the presence of soft fibrous tissues. The provision of a high calcium and phosphorus-rich environment promotes rapid bone formation within the vicinity of the HA implant. HA also establishes strong interfacial bonds with titanium implants. Its excellent biointegration makes it as an ideal choice for use in orthopaedic and dental applications [16]. Moreover, some authors [17] claimed that HA might act as a biological barrier to reduce toxic responses caused by the release of metallic ions from the metal substrate into the bone.

The chemical formula of HA is “ $\text{Ca}_{10}(\text{PO}_4)_6(\text{OH})_2$ ” which is also presented as $\text{Ca}_4(\text{I})\text{Ca}_6(\text{II})(\text{PO}_4)_6(\text{OH})_2$. The Ca(I) atoms are on the fourfold symmetry $4(f)$ position and the Ca(II) atoms are in the sixfold symmetry $6(h)$ position [18]. The OH groups occupy disordered positions above and below the triangles formed by the Ca(II) atoms. The disorder of the OH groups gives rise to a "macroscopic" space group $\text{P6}_3/\text{m}$ (as determined by X-ray diffractometry), which is lost at the level of the individual columns [18].

As shown in Figure 2.2 and Figure 2.3, biological HA has a hexagonal lattice with the space group of $\text{P6}_3/\text{m}$ [19] and with dimensions of $a=b=9.418\text{\AA}$ and $c=6.884\text{\AA}$, respectively. The representative of z axis of hexagonal cells from the HA lattice is shown in Figure 2.3. Hydroxyl ions and four Ca ions at Ca(I) sites lie along columns parallel to the c axis. OH atoms are sited along the c axis, and the O-H bond direction is parallel to it, which are represented by the solid dots from the HA unit cell; the remaining six Ca atoms, positioned at Ca (II) sites, are associated with the two hydroxyl groups in the unit cell, where they form triangles centered on, and

perpendicular to, the OH axis and laying on the mirror planes. Ca atoms form a smaller hexagonal cell (without an identical point in the center). The phosphate tetrahedral PO_4 forms the remaining basic structural unit of HA. The size ratio of the HA unit cell to the Ca cell is about $\sqrt{3}$. The crystal data of HA and some other physical properties are shown in Table 2.1. The stoichiometric Ca:P ratio of HA is 10:6. Its calculated density is 3.21 g/cm^3 .

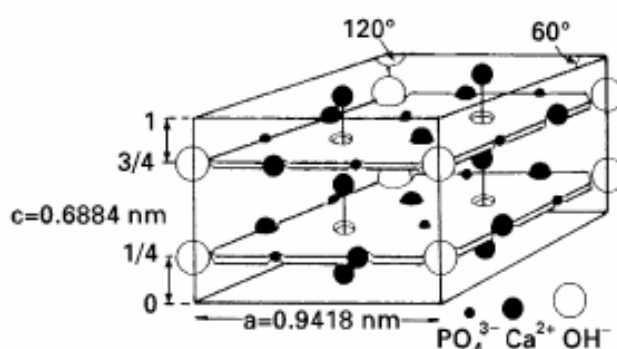


Figure 2.2 Crystal structure of HA [19]: $a=b=9.418\text{\AA}$ and $c=6.884\text{\AA}$.

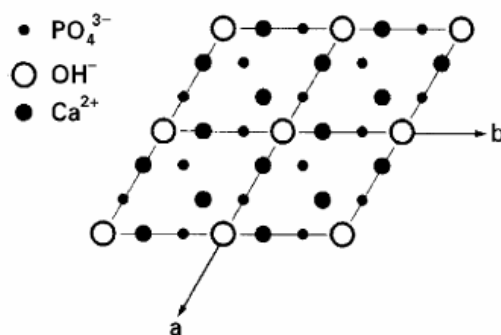


Figure 2.3 (001) plane of HA at $z=3/4$ [20].

Calcium phosphate-based bioceramics have been used in medicine and dentistry for over 20 years, because of their excellent biocompatibility with human tissues. Application of HA bioceramics include dental implants and percutaneous devices; or

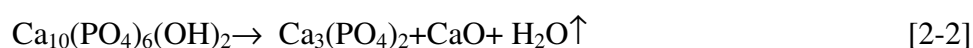
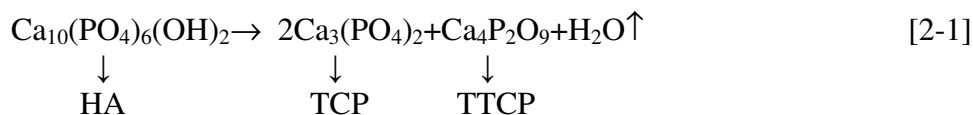
periodontal treatment, alveolar ridge augmentation, orthopedics, maxillofacial surgery and spinal surgery [15].

Due to the high impact that HA has in bio-medical applications, it is important to investigate the production methods and the properties/processing parameters. Many methods have been used for the production of HA powders and HA coatings on different substrates.

Table 2.1 Physical properties of HA [21].

Molecular weight	1004.8
Space group	P6 ₃ /m
Lattice constants	a = 0.9423~0.9418nm, c = 0.6881~0.6884nm
Chemical unit number	Z=1
Theoretical density	~3.156g/cm ³
Thermal diffusivity	~5×10 ⁻³ cm ² /s

According to the equilibrium phase diagram of CaO-P₂O₅-H₂O at a water vapor pressure of 500 mm (Figure 2.4), the melting point of HA powder is around 1570 °C. HA may be decomposed into different Ca-P phases at elevated temperatures, which include TCP, CaO and TTCP [22]. The following decomposition reactions represent the possible chemical decomposition of HA while it is heated [13]:



It has been shown that the HA crystal structure may be retained if water is partly removed to form a solid solution of HA and oxyapatite (Ca₁₀(PO₄)₆O), the loss of water gives rise to a HA-oxyapatite solid solution in which the chains of OH⁻ are

replaced by chains of OH^- , O^{2-} and vacancies. The difference in lattice parameter between HA and oxyapatite is reported to be sufficiently small that structural changes arising from loss of water are not obvious from XRD patterns. OH^- depleted HA has been shown to be very reactive, absorbing H_2O at $\sim 600^\circ\text{C}$ even in a vacuum of 1.33×10^{-2} Pa [23].

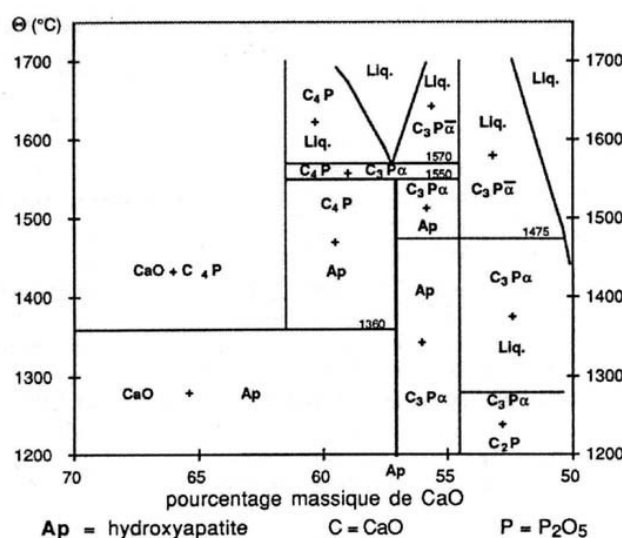


Figure 2.4 Phase diagram of $\text{CaO}-\text{P}_2\text{O}_5$ under a partial pressure of water $p(\text{H}_2\text{O})=500\text{mm}$ [24].

During the plasma spraying process, HA powder is injected to high temperature (around 20,000K) for a very short time (only few milliseconds). In this situation, HA may melt in a meta-stable manner without water loss. However, increasing loss of H_2O and P_2O_5 from the molten droplets might be expected as the temperature-time regime is increased [23]. In the presence of a high partial pressure of water vapor, the decomposition associated with elevated temperature could be partially suppressed according to Le Chatelier's principle [25].

2.3 Application of HA

Commercial HA bioceramics and their composites are available in different forms [26]: granules, blocks, specially designed forms for specific applications (wedges,

cylinders), and in injectable form in a hydroxypropylmethyl cellulose carrier. Dental and orthopedic applications of HA bioceramic include [27]: repair of large bony defects, periodontal defects, orthopedic lesions, lumbar spine fusion, correction of scoliosis, fillers for enchondroma of the metacarpals and phalanges of the hand and ophthalmic implant. It has also been used as carrier [27] for antibiotics related to repair of orthopedic lesions. Studies [28] on potential applications of HA include: carriers for growth factors, hormones, and as scaffold for tissue engineering using stem cells.

2.3.1 HA for surface modification of implant substrate

HA lacks sufficient strength; has low toughness ($0.8-1.2\text{MPa} \cdot \text{m}^{1/2}$) and low flexural strength ($<140\text{ MPa}$) for application in major load bearing parts of the skeleton. But this can be compensated by using HA as a coating on metallic substrates [29]. As coatings, they are not intended to substitute existing materials but to improve the characteristics of a fully functional implant [30]. A good prosthetic design should accommodate eventualities such as coating failure without jeopardizing the function of the implant. This perception is important to ensure that the role and purpose of coatings is not misunderstood. Coatings have specific functions ranging from improving fixation by establishing strong interfacial bonds, to shielding the metallic implant from environmental attack or leading effects [16]. Coatings used for biomedical applications are often subjected to many stringent constraints. An HA coating may provide the implant increased tolerance of the inevitable natural bone remodeling that occurs within its vicinity. It may help to provide a bone maintenance system around the coated area, a quite important long-term advantage [31].

When used in load-bearing applications such as dental and orthopedic implants, HA coating has the following advantages: fast bony adaptation, absence of fibrous tissue

seams, firm implant-bone attachment, reduced healing time, increased tolerance of surgical inaccuracies, and inhibition of ion release. These advantages are relatively short term in nature, but may provide factors that increase the long-term implant stability.

Many new techniques are used to produce HA coatings on metallic implants, such as plasma spraying [32-36], electrochemical co-deposition, RF magnetron sputtering [37], high-velocity oxygen fuel spraying [38] and sol-gel processes [39].

Generally, the mechanical properties and phase composition, as well as the operation feasibility, are the most considered factors as these methods are to be adopted. The HA coatings obtained from these various techniques differ in chemistry and crystallinity, which would affect, in return, the biological response of the coating and ultimately its performance. Among all the surface coating techniques, plasma spray is the most preferred in terms of: low substrate temperature, large coating thickness that can be up to several centimeters, good mechanical performance of the coating and low cost [40]. It also renders increased tolerance of surgical inaccuracies, fast fixation of the implants in bone, corrosion and wear resistance, and firm implant bone attachment [32-36].

2.3.2 Production of HA compacts

A question of major importance in the development of implant materials is their mechanical strength. Bioceramic must be close in strength to bone tissue; exhibit a high fatigue resistance under both static and dynamic loads, especially in the corrosive medium of the human organism; and possess good fracture toughness. Of particular importance is the problem of biomechanical compatibility.

Due to its poor mechanical properties compared with those of natural bone, much attention has been paid to the development of dense HA ceramic capable of withstanding mechanical loads, which can be obtained if the starting powder is stoichiometric with better powder properties like particle size, distribution and morphology [41-43]. Dense HA based ceramic can be fabricated by various techniques, depending on the desired microstructure and properties of the material. Sintering is one of the most important technological processes in the powder metallurgy and ceramic industry [44]. Synthetic HA can be sintered pressurelessly up to near theoretical density at moderate temperatures (1100-1200 °C) [45-47]. The densification process of HA is achieved [48] via compaction and sintering by methods such as pressureless sintering, microwave sintering and hot-pressed sintering process.

Sintering may be described as a thermal process that produces growth of contacts between particles and their coalescence. Theoretical concepts of sintering are originally based on ideas of a discrete organization of porous media. The sintering kinetics is determined not only by the properties of the powder particles and the nature of their interaction, but also by macroscopic factors. Among them are kinematic constraints (adhesion of porous sample's end face and furnace surface), externally applied forces and also, inhomogeneity of properties in the volume under investigation (inhomogeneity of initial density distribution caused by preliminary pressing of the porous sample).

Uni-axial pressing is the most common method of achieving compaction [49]. The influence of powder processing and sintering temperature on densification, microstructure and mechanical properties of HA ceramics has been studied [41]. Uniform and consistent microstructures are observed for the powder compacts that

have been calcined and milled for 6 hrs. It is found as well that calcination of HA could reduce the particle size, narrow its distribution, and improve the microstructure and mechanical properties. However, the sintered body tends to lose its uniformity and develop cracks [49].

Hot-pressing of HA [50] has been found to allow densification to take place at much lower temperatures than in the conventional sintering process. This is an advantage as lower temperatures prevent the formation of other calcium phosphate phases such as α -TCP and β -TCP that may form when sintered at temperatures above 900 °C [51].

Microwave heating of inorganic materials [52] has been studied for the last two decades. It is known as the speedy processing route for the sintering of various ceramic systems. Microwave couples effectively sinter certain materials by generating heat within the substance depending on their dielectric constant and dielectric loss factor properties. Microwave sintering is a unique processing method that not only offers shorter processing time but also imparts better physical and mechanical properties to the final sintered ceramic. It has been used [53] to prepare porous as well as dense HA ceramic starting from powders synthesized by hydrothermal methods. It is found that the nature of powders plays an important role in the microwave-assisted sintering of HA. Nanocrystalline HA has been successfully sintered [52] at a density as high as 95% in 5 min with the microwave couples working at low temperature. Cheang and Khor [54] reported that microwave treatment enhances the elastic modulus of the PMMA-HA composites by promoting interfacial bonding.

SPS is a novel and rapid sintering method, using the self-heating phenomena within the powder. It is capable of sintering ceramic powders rapidly to its full density at a

relatively low temperature compared with the conventional furnace sintering method [56-60]. A SPS system was developed in 1990 [61]. Since then, a variety of materials such as metallic materials [62-63], structural ceramics [64-65], oxide superconductors [66-67], ceramic composites [68-69], polymers [70] have been prepared by SPS. The SPS system resembles the conventional hot-press. However, in SPS, a pulse electric current and/or a direct current is applied directly to the graphite mold. In this way, the graphite mold and punches act as heating elements, which is different from the case of the hot-press [71].

During the SPS process, neck formation among the powders does happen, and it is attributed to the effect of spark plasma caused by the pulse electric current. The surface of the particles is activated electrically by the application of an ON-OFF pulse voltage and current, which generates momentarily DC plasma between the powder particles (Figure 2.5). Several advantages arise from using SPS as a consolidation method. Firstly, the high heating efficiency of particles significantly shortens the high temperature exposure of powders that is essential to preserve the initial microstructure. Also, the electrical energy supplied in combination with mechanical pressure shorten the consolidation times, avoiding the formation of coarse microstructures. Secondly, the plasma discharge generated between powder particles confers a significant surface cleaning ability that leads to enhanced particle sinterability.

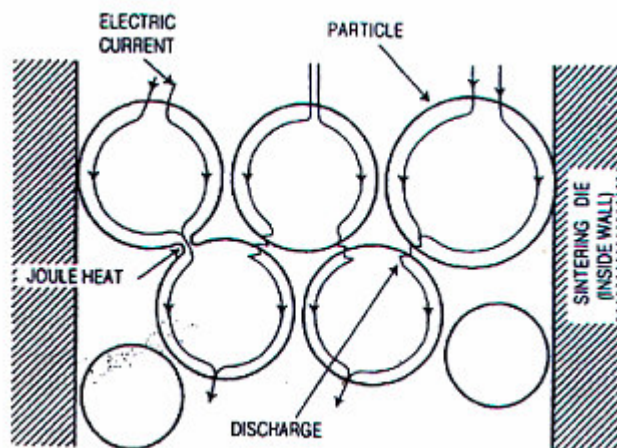


Figure 2.5 Pulsed current flow through powder particles [55].

SPS methods help preserve the initial grain size during the densification process; thus leading to pure extremely consolidated materials with improved mechanical properties [55]. This concept has attracted special interest from both industry and research institutes. Yu et al [72] used a SPS technique as a post-spray treatment on plasma sprayed HA coatings. Their results showed that SPS treatment could enhance the surface activity of plasma sprayed HA coatings.

2.3.3 Production of HA powders

HA in the form of particles or granules has been used as a substitute material for bone in bone graft surgery. The properties of medical implants depend on the powder properties of the HA used. It is known that the properties of the feedstock play an important role among all the considered factors that influence the coating and ceramic performance [73]. It is also essential to have complete control of the powder properties, such as particle size, surface area, morphology and crystallinity, which can be tailored for each specific application in order to maximize the properties of the final biomedical implant. Several manufacturing methods for the synthesis of HA

powders have been explored, which include liquid reaction, solid phase reactions, hydrothermal reaction, the alkoxide method and the flux method [74]. The main characteristics of the HA feedstock, including the size, shape, composition and structure of the powders, have been systematically investigated [75-77].

2.3.3.1 Wet chemical synthesis of HA

The wet chemical reaction method is a popular and well established method to fabricate HA. It is also known as sol or gel or physical gel method. In this method, an aqueous colloidal HA suspension is obtained through the reaction of orthophosphoric acid with calcium hydroxide. The slurry is either transported to a spray drier for atomization into fine HA powders or dried at high temperature in an oven to evaporate the water [78]. HA coatings or ceramics would then be processed by techniques such as plasma spraying or sintering methods [79].

An overview of the synthesis procedure is given schematically in Figure 2.6. It consists primarily of three steps: (1) preparation of the solution, (2) precursor synthesis, and (3) high temperature treatment to consolidate powder.

Among the techniques developed to produce powders, spray drying has proved to be the most versatile process [80]. In the spray drying method, a slurry containing finely dispersed particles of the materials is agglomerated. In order to prepare specific powders, two steps have to be mastered: the slurry stability and the spray drying operating conditions.

During spray drying, the solution is extracted from a feed tank and passed through the spray atomizer. It is a result of many interwoven complex mechanisms. The feed materials are either water-based suspensions with air as the drying gas or organic

solvent-based suspensions (usually ethanol) with nitrogen as the drying gas. Compressed air with a selected pressure is used during spraying. The atomized liquid is dried rapidly by a coaxial flow of air that is previously preheated to a specific temperature. The dried powder is cyclone separated from the flowing air stream.

The preparation of the suspension is believed to be more important than the operational parameters of the spray-dryer in terms of influencing characteristics of the dried powder. A low solid content in the suspension causes the particle size to decrease. An increase in density is obtained from an increase in the solid content.

Due to the high flowability and hence the high green density achieved, the spray-dried powder can provide sintered bodies with high densities and highly precise dimensions. Therefore, the particle size, the size distribution and the particle strength, which determines the behavior during cold compaction, are the most important parameters for a spray-dried powder with high sinterability [81].

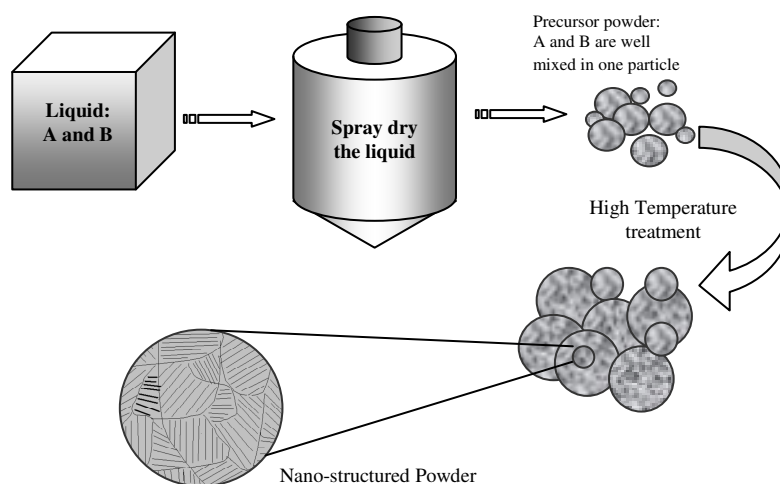


Figure 2.6 Schematic illustration of the wet chemical reaction method [15].

There are five factors that influence the characteristics of spray-dried powders: feeding rate, drying temperature, atomizing pressure, type of atomizer, and suspension composition [82].

The greater the feeding rate, the larger the particle size. But if feeding rate is too high, the feeding solution will not be able to dry. The effect of drying temperature is multifold. First, the higher the drying temperature, the larger the droplet ballooning, and therefore the larger the particle size; second, the higher the temperature, the lower the surface tension of the droplet, resulting in an increase of particle size; third, the warm-up period of drying is shortened by fast heating, and thus crust formation starts earlier in the drying process resulting in a decrease in particle size. The technique of the slurry atomization determines the powder particle grain size. The higher the working rotating speed, the higher of atomization pressure, thus the smaller the particle size.

However, this sol-gel formed powder is not useful particularly for forming dense monoliths, because of the extensive volume changes involved in converting wet and porous gels to fully sintered, dense monoliths. Furthermore, despite the high chemical homogeneity of sol-gel processed powders, low diffusion rates still present an obstacle to achieving high densities with coincident control of microstructure, especially using pressureless-sintering methods [83]. Therefore, this agglomerated powder would need to undergo a post-treatment like crushing and milling in order to obtain a well-distributed powder and those entire steps can potentially introduce contamination.

2.3.3.2 Spherical HA powders

Due to spherical particles good flowability, bioactivity and non-rigid contacts

between particles, it has been used as the feedstock for coatings and sintering processing. Spherical powders also have better rheological properties than the irregular sol-gel processed powder, and thus produce better coatings for hip implants and chromatographic separation [15]. A popular method used for spheroidization is thermal plasma technology which is a viable technique for the production of dense, monolithic, and composite forms [84].

During the plasma spheroidization process, a powder feedstock is injected into a high temperature plasma jet [85]. The powder can be injected through either an external or internally feed-port. The plasma jet can be generated by passing a gas through an electric arc. Ionization of the gas then takes place by excitation of RF, microwave, or electrons from a hot filament discharge. This gas stream is in return converted into an extremely hot plasma jet, then a process called ‘electrical breakdown’ takes place. The velocity of the plasma jet is in the range of 300-500 m/sec while the temperature of the plasma can reach in the order of 20,000 °C [86]. The high-density of ionized and excited species in the plasma can change the surface properties of normally inert materials. The whole process takes about 100 msec depending on the size of the plume and the particle velocity in the plasma. The thermal history of the particle in the plasma will greatly influence the characteristics of the spheroidized powders. Two situations can develop depending on the processing history of the particles. One situation is that micron sized feedstock undergoes surface melting, and their final diameter will be obtained upon reaching the tail end of the plasma. The other situation is that vaporized materials condense into the nano-sized particles.

2.4 Production of Nano-structured HA

Although HA has a similar chemical composition to that of natural bone, it lacks sufficient strength and toughness for use in major load bearing application. Very often it requires blending with a low modulus polymer to achieve adequate toughness [87]. In the field of advanced materials, grain-size reduction has been an important method to improve material properties. Most of the mechanical property data on the materials have pertained to hardness, which is a function of grain size. The small grain sizes allow more efficient deformation mechanism (e.g., diffusion creep) and more effective crack dissipation than that is normally available in coarse-grained materials [88]. The equation relating grain size to strength and hardness can be described by an equation known as the Hall-Petch relationship [89]. This expression is

$$\sigma_i = \sigma_0 + k d^{1/2} \quad [2-3]$$

This relationship serves to demonstrate that the yield stress increases with decreasing grain size. Similar results are obtained for hardness, with $H=H_0 + k d^{1/2}$.

The Hall-Petch effect is due to the dislocation motion/generation in materials that exhibit plastic deformation [89]. Nano-structured (or nano-crystalline) materials are characterized by a micro-structural length scale in the 1-200 nm regime. More than 50% of atoms are associated with grain boundaries or interfacial boundaries when the grain is small enough [90]. Thus, a significant amount of interfacial component between neighboring atoms associated with grain boundaries contributes to the physical properties of nano-structured materials. The nano structure is significant in the improvement of ductility in brittle materials such as ceramic.

Due to the high chemical reactivity and high specific surface areas, nanocrystalline CaP phases, are now increasingly being researched as binding and delivery agents for drugs, proteins and DNA and for vaccine production [91]. The high specific surface area of nano-structured CaP phases not only provides a large number of binding centers for attachment of DNA, but also allows for efficient condensation so that the CaP-DNA composite is in the suitable size range for efficient attachment and migration into the plasma membrane.

Natural bone is actually inorganic/organic composite mainly made up of nano-structured HA and collagen fibers. Therefore, to obtain high levels of bioactivity and bone bonding, it is reasonable to make both the composition and the microstructure (especially the surface topography) of the HA implant similar to those of the natural bone. Compared with conventionally crystallized HA, nano crystallized HA used in a scaffold [92] promotes osteoblast adhesion and proliferation, osseointegration, and the deposition of calcium-containing minerals on its surface. It also promotes the formation of new bone. Design of biomaterials with surface properties similar to physiological bone (characterized by surface grain sizes in the nanometer regime) would undoubtedly aid in the formation of new bone at the tissue/biomaterial interface and improve orthopedic/dental implant efficacy [93-95].

It is hypothesized that a sample composed mostly of nano-sized crystalline HA with some nano-sized amorphous phases distributed over the crystalline phase will provide enhanced bioactivity and osteoblast bonding. The nano-crystals of HA will be more soluble due to their very high interface area. The dissolution of the nano-sized amorphous phase will accelerate the precipitation of nano-structured apatite, but it will not cause the degradation of the whole coating due to the very small size.

Dissolution of amorphous regions would lead to formation of nano-porosity, which will subsequently enhance bone to grow into the porous coatings.

A number of techniques are used in the production of nano-structured materials: gas condensation, mechanical alloying/milling, crystallization of amorphous alloys, thermochemical method, spray conversion processing, vapor deposition, sputtering, electro-deposition, and sol-gel processing techniques. Of these techniques, only mechanical alloying /milling and thermo-chemical techniques have been used to produce large quantities of nano-structured materials for possible commercial use [90]. Many synthesis methods for nano HA have been published, but they are all essentially based on the chemical precipitation method.

Chemical coprecipitation [91] is a simple operation experiment at low temperatures. It has high yields of pure products. Nano-sized HA powders are prepared by a coprecipitation process using calcium nitrate and phosphoric acid as starting materials.

Rod-like HA [92] is synthesized by precipitating calcium nitrate tetrahydrate and ammonium dibase phosphate in the presence of polyacrylic acid followed by hydrothermal treatment. Both the polyacrylic acid and the hydrothermal treatment stabilize the HA and the hydrothermally treated HA contains nano-particles.

Nano-crystalline plate-shaped particles of HA [93] are directly precipitated from dilute calcium chloride and sodium phosphate solutions by submitting the aqueous solution to microwave irradiation immediately after mixing. The precipitated crystallites are loosely aggregated in spherulites of 2-4 μm .

The plasma processing method is also effectively used to produce ultrafine and spherical particles with interesting physical, chemical and mechanical properties.

During plasma processing, a raw material is evaporated instantaneously in a high temperature plasma flame. The produced vapor condenses into ultrafine particles by subsequent rapid cooling. Usually either a RF or DC plasma is used for this purpose. Since the RF plasma has a larger flame or reaction volume than the DC plasma [94], the efficiency of the ultrafine particles production is generally higher in the former than in the latter. A novel spraying system of HA powders has carried out by using a RF suspension plasma to produce ultrafine HA powders [87].

RF plasma experiments can be traced back [95] to Babat and Reed. The plasma is formed typically by the inductive coupling of oscillating electrical energy. It displays unique characteristics which can be used advantageously in the thermal processing of materials. These include powder densification and spheroidization, IPVS, PFVD, synthesis of ultra fine powders and recently, suspension plasma spraying. Figure 2.7 shows a model for the production of nano powders by the RF spray method [94].

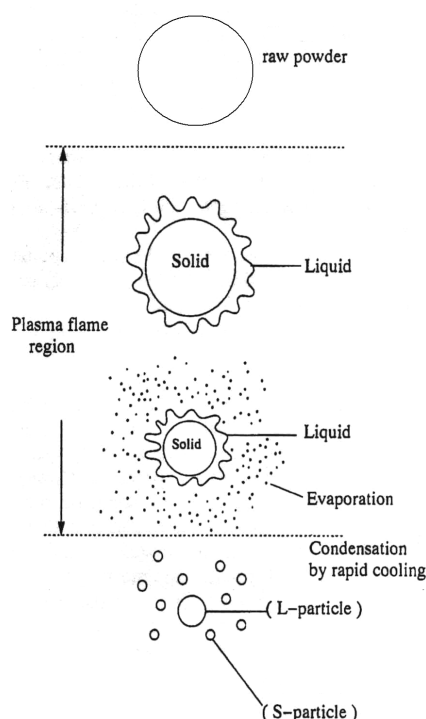


Figure 2.7 A proposed model for nano-sized powders production by RF plasma [94].

The RF generates a thermal plasma that offers a 10,000 K hot region free from electrode contamination. Compared with direct current plasma jet, the long residence time for particles injected into this kind of plasma jet makes it suitable for the production of ultrafine particles or coatings. Moreover, the electrodeless plasma generation process leads to a high-purity product without suffering contamination from the evaporation of the electrode [94, 96], which is a key requirement in the biomaterial field. In addition to plasma spray, where melting of injected precursor materials is sufficient, the plasma flash evaporation technique requires complete evaporation of the precursor to produce high performance coatings or nano-sized powders [97]. The method consists of an evaporation phase where the injected solid precursor materials are vaporized, and partly dissociated. Rapid quenching causes a limited growth of nucleating particles or condensation of a coating on an appropriate substrate.

Another advantage of the RF plasma is that it allows optimum treatment and melting of large particles at high throughput [98]. When coupled with the ease of axial injection of the powder into the plasma, homogeneous melting of relatively large particles can be obtained. In terms of temperature, a RF plasma possesses less severe thermal gradients within the plume than a DC plasma, which results in better control of the material heat treatment in the plasma. The process takes full advantage of the inherent features of an induction plasma discharge that allows sufficient dwell time for the droplet drying and consolidation steps.

2.5 Problems involved with high temperature processed HA

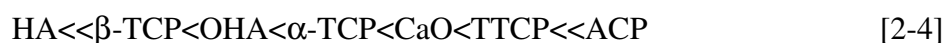
During plasma processing, particulate materials are injected into the high temperature heat sources where they are melted and propelled at high velocity

towards a substrate. A feature pertinent to the high temperature that the HA powder undergoes during plasma spraying is the generation of an amorphous phase, along with other non-bioactive calcium phosphate phases [34]. These transitional phases can elicit unfavorable resorption and toxicity effects. Therefore, the phase and crystallinity of the plasma sprayed HA have to be controlled to ensure the appropriate biological responses of the implant in the body.

The formation of an amorphous phase is associated with partial dehydroxylation of the HA during the plasma spray process [99-100]. Its presence especially at the interface between the substrate and coating has to be avoided as it could compromise the integrity of the coating during its service life. The rapid resorption of the amorphous phase causes mechanical and adhesive instability in the coating. However, Gross et al [101] believe that amorphous calcium phosphate phase is good for absorbing mechanical mismatch, improves fatigue behavior, and promotes fast remodeling and attachment. Thus, HA coatings with some amorphous phase are preferred for clinical applications.

Besides amorphous calcium phosphate phase, the extreme heating and cooling conditions of the plasma processing can also produce other calcium phosphate phases such as tricalcium phosphate TCP, TTCP, oxyapatite and calcium oxide (CaO) [102-105]. Variations in plasma-spraying parameters can, therefore, lead to profound effects on the dissolution behavior of the coatings.

It is reported that the dissolution behavior of different calcium phosphates increases as follows:



Since the dissolution behavior of the coatings reflects their phase distribution, the presence of metastable components (e.g., TCP, TTCP) in return leads to an increase in instability of the coatings. Therefore the phase balance of the plasma-sprayed coating may affect its long-term behavior under *in vivo* conditions.

The location of an amorphous phase, oxyapatite, TCP, TTCP within the lamellae has been discussed by Gross et al [104] in a proposed model for phase formation in plasma-sprayed HA coatings, which is shown in Figure 2.8. It is found that phase transformations are produced by: (a) preferential removal of hydroxyl and phosphate leading to a change in melt composition; and (b) the high cooling rate due to the thermal process. Hydroxyl group removal promotes the amorphous phase and oxyapatite. Further heating produces a less viscous melt; thereby facilitating decomposition of HA to TCP and TTCP. Phosphate removal during flight produces a more calcium-rich melt preferring TTCP and CaO formation.

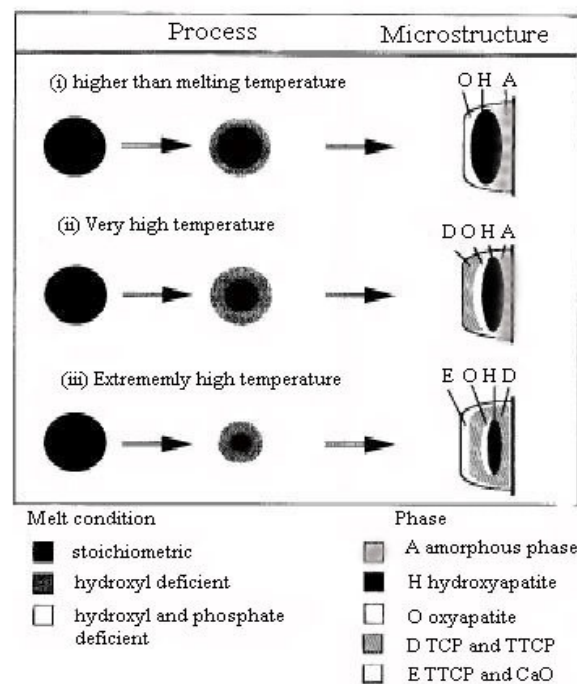


Figure 2.8 A proposed model for phase formation in plasma-sprayed HA coatings [104].

2.6 Post deposition heat treatment

The OHA, TTCP and TCP obtained from high temperature processing undergo dissolution and degradation more rapidly than HA in an aqueous environment, which decreases chemical stability, and enhances degradation of the implants *in vivo* [106]. Like other amorphous phases, the amorphous calcium phosphate in the as-sprayed coating is thermodynamically metastable. It enhances adhesion to the substrate but dissolves quickly in body fluids and, adversely affects bone formation [73]. Since HA coatings with lower crystallinity would result in an increased dissolution, a high crystallinity level is desirable in order for the materials to have appropriate bioactive properties [107] and/or good biointegration by minimizing the soluble phases. An appropriate thermal treatment could induce crystallization to occur; therefore several studies [108-114] suggested that the as-sprayed coatings may be subjected to a post heat-treating cycle.

To promote dissolution resistance and reduce the residual stress of HA-based coatings, post deposition heat treatments aim to recover the crystalline HA structure by inducing recombination of these secondary compounds with water vapour, and recrystallization of amorphous phase without the formation of OHA, and other undesirable compounds within the ceramics [108].

Gross et al [109] heated an amorphous phase of HA coating in dry and moist atmosphere. The latter gave rise to more extensive crystallization. McPherson et al [110] found that heat treatment of HA coatings in air at 600 °C resulted in crystallization of the glassy phase and a reaction with water vapor formed HA. Zyman et al [111] heated HA coatings at 630 °C. The amorphous calcium phosphate coating was completely crystallized. Chen et al [112] studied the effect of increasing the

crystallinity of HA coatings by post-heat treatment. It was found that TTCP and α -TCP could convert to HA by hydrolytic reaction in humid atmosphere. Lin et al [106] investigated the reconstruction behavior of quenched HA powder in air. It was found that, when quenched HA powders were reheated, TTCP gradually reconstructed into HA around 500 °C and yielded Ca(OH)_2 . TCP did not convert to HA at a temperature lower than 700 °C but the transformation of α -TCP to β -TCP was observed during heating. α -TCP reacted with CaO, and then converted to HA around 900 °C. Khor et al [113-114] used a laser as post heat treatment of the HA coating to improve the crystallinity. The results showed that the crystallinity of the sprayed coatings was increased significantly by transformation amorphous phase to crystalline HA without producing cracks.

Post spray heat treatment would further promote the interfaces bonding between the coating and substrate, and is deemed to be a necessary step to transform the amorphous calcium phosphate into the HA structure [33]. While, the cracks generated by heat treatment should also be considered [115].

2.7 Modified calcium phosphates

Although the Ca/P ratio of HA is close to the Ca/P found in fully mature bone, HA is not the complete model for bone mineral. Natural HA appears to have a higher bioactivity and mechanical properties compared to the synthetic HA. This has been attributed to the nano-crystalline characteristics and the subtle chemical differences found in the natural HA. It is reasonable to make the microstructure of the HA implants similar to those of natural bone to obtain high levels of bioactivity and bone bonding. It is, therefore, essential to improve the mechanical properties and bioactivity for the long-term application.

A number of approaches have been developed to improve the mechanical properties of HA biomaterials, which include producing a polyethylene-HA composite; the addition of a second, high-strength ceramic phase, such as yttria-doped zirconia; or the addition of a glass-reinforcing phase, such as, a CaO-P₂O₅ glass. An established and simple method of improving the rate of remodeling of an HA implant is to introduce appreciable levels of a more resorbable calcium phosphate phase, such as β -TCP. The most popular approach to speeding the rate of osseointegration of HA implants is to incorporate biological entities, such as growth factors, proteins, and cells, onto the surface of the HA implant.

Another approach to improve the biological properties of HA is to adjust its chemical composition close to that of bone mineral. Synthesis of chemically modified or ion-substituted HA has drawn great interest. The apatite structure can incorporate a wide variety of ions that can alter both the cationic and anionic sublattices. The most common substitutions can incorporate cations with the same oxidation state as Ca²⁺, such as Sr²⁺, Pb²⁺, Mg²⁺, etc. These ions play an important role in developing artificial bone with enhanced mechanical properties and bioactivities. The F⁻ and Cl⁻ anions could be substituted to the same oxidation state of OH⁻ in apatite. Ionic substitution with different oxidation states are also very common, and have an important role in the chemical, structural, and micro-structural properties. For example, in biological apatites CO₃²⁻, substitution for PO₄³⁻ or OH⁻ is a likely substitution. This substitution of carbonate ions into the HA structure (between 3 and 8 atomic % carbonate) resembles the levels detected in bone mineral. In the case of carbonated apatites, the incorporation of single valence cations (Na⁺ or K⁺) in the Ca²⁺ position is required to achieve the neutrality. Studies have shown that this type of substitution increases the solubility of HA, and also enhances the proliferation of human osteoblast cells *in vitro*.

2.7.1 Addition of silicon/silica into HA

Besides seeking for the appropriate mechanical properties, biocompatibility will be an important feature of an implant. The implant must be biologically compatible to the living tissues, and not produce any toxic, injurious, or immunological response to the environment [1]. Carlisle et al [116] have indicated the importance of silicon (Si) for bone formation and calcification through electron microprobe study. It has been shown that silicon is localized in active growth areas, such as the osteoid (bone matrix before calcification), of the young bone of mice and rats, and silicon levels up to 0.5weight % are observed in these areas [116]. Moreover, it has been observed that the addition of Si during the HA synthesis leads to an improvement of the bioactive behaviors [117] by formation of a poorly crystalline apatite layer at the surface of the implant after immersing it in SBF. This allows the implant to join chemically to the bone through a strong bond. In this way, good performance of the implant is ensured.

Si-substituted HA becomes an attractive alternative to conventional HA materials for use as bone substitute ceramics. Table 2.2 contrasts the main properties of the silica/silicon modified HA compared to HA samples. The ideas concerning the role of silica in biological functions are related to the ability of silica in the form of silicic acid ($\text{Si}(\text{OH})_4$).

The silicon substitution has the effect of increasing the sintering temperature of HA. In addition, silicon substitution reduces grain growth, and augments Vickers hardness values compared to stoichiometric HA. Moreover, the introduction of silicon substituting phosphorus in the hydroxyapatite improved the *in vitro* bioactive response of HA [117]. The *in vitro* bioactivity of the Si-substituted apatite is governed by the chemical nature of the surface rather than by its bulk composition. Samples

containing monomeric silicate anions showed higher bioactivity than those containing polymeric silicate species.

Table 2.2 Main properties of silicon/silica modified CaP compared to pure HA.

	Silica/silicon modified CaP
Chemical formula	$\text{Ca}_{10}(\text{PO}_4)_{6-x}(\text{SiO}_4)_x(\text{OH})_{2-x}$
Biological properties	Enhance the initial bioactivities of HA and significantly increase the rate of bone apposition to the implants.
Sintering behaviors	When compared with pure HA, the presence of silicon inhibits densification at low temperature and the sintering is comparable at high temperature.
Mechanical properties	Increased Vickers hardness by the relatively small grain sizes.

Many approaches have been used to achieve Si-substituted HA. Gibson et al [118] developed a popular method for attaining Si-substituted HA by an aqueous precipitation technique. Several other studies have prepared co-substituted HA through high temperature solid-state methods. However, this method requires the substitution of a second ion such as lanthanum in addition to silicon. Table 2.3 summarizes the silicon/silica modified CaP using different methods.

Table 2.3 Description of different approaches to fabricate silica/silicon modified HA

Methods	Descriptions
Wet chemical method[134]	The Si acetate is added into the structure of HA via an aqueous precipitation reaction between calcium hydroxide and orthophosphoric acid. The in vivo results indicated the bioactivity of HA is significantly enhanced with the addition of silicate ions into HA structure.

High temperature[135]	Silicate containing apatites are synthesized by a solid state reaction at high temperatures, which allowed the preparation of materials suitable for use as high performance matrices.
Surface modification[136]	HA are coated with varying amount of silica via hydrolysis of tetraethyl orthosilicate. The specific surface area of the silica-coated HA increase based on a heterocoagulation coating mechanism.
Bioglass addition[137]	The addition of bioglass enhanced HA phase decomposition and hydroxyl group breakdown processes, decreased HA density and micro-hardness, increase toughness and promoted micro-cracking.
HA-silica composite[138]	HA is synthesized by diffusion of calcium ions throughout an alkaline silica gel matrix set with phosphoric acid at pH higher than 10. The obtained crystals are elongated with a mean size of 100nm.

2.8 *In vitro* tests

The growth of apatite crystals on the surface of biomaterials determines the characteristics and performance of a number of biomaterials. Because body fluid is highly supersaturated with respect to apatite, apatite deposition may occur on the surface of any biomaterial immersed in body fluid. For biomaterials that could be used in contact with bone, it is desirable to enhance growth of apatite on the implant surface. This will subsequently result in the formation of a chemical bond between bone and biomaterial. Figure 2.9 presents the proposed bonding between bone and implant. The precipitated apatite layer will serve as a substrate for subsequent protein adsorption and bone cell attachment. The proteins from the body serve as cell receptors, and adsorb onto the apatite surface (cell ligand), thus, enabling cells to attach onto the implant.

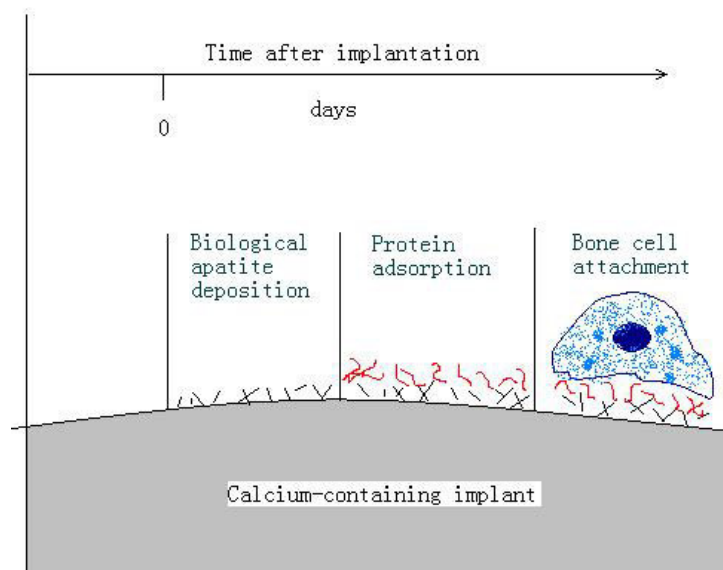


Figure 2.9 A schematic shows the proposed mechanism facilitating the bonding of bone to certain implants [119].

These biological properties of biomaterials should be tested before medical application. Many studies have been carried out for a comprehensive understanding of the factors that control the biomechanical properties *in vitro* studies. In an *in vitro* study, the material is immersed in a protein-free and acellular solution that has an ion concentration nearly equal to that of human blood plasma; i.e., simulated body fluid.

2.8.1 Simulated body fluid

Due to its close chemical composition to that of human blood plasma, the bioactivity of an artificial material can be evaluated by examining the formation of apatite on its surface following immersion in SBF. It has been suggested that the efficacy of apatite nucleation is determined not only by their composition, but also on their concentration and structural arrangements.

After soaking in SBF, an HA sample is negatively charged immediately due to OH^- and PO_4^{3-} and the positively charged Ca^{2+} ions in the fluid. As the calcium ions

accumulate, the surface imparts a positive charge, and thus combines with negatively charged phosphate ions in the fluid to form amorphous calcium phosphate. This phase is metastable, and eventually transforms into stable bone-like apatite.

The formed apatite layer incorporates carbonate ions from the solution into its lattice by substituting phosphate groups. This substitution promotes the differentiation of marrow stromal stem cells into osteoblasts (bone-producing cells) that are responsible for the formation of bone.

2.8.2 Cell culture

Cell culture tests are used not only to test material cytotoxicity (cell poisoning), but also to investigate surface-dependent responses of bone-forming cells. The quality of the bone where cell cultures are to be grown, is taken into account in *in vitro* study. This kind of approach concerning the *in vitro* research requires models that simulate the *in vivo* conditions: the study of the primary osteoblast (bone forming cell) behavior seems relevant to this purpose. Such a cell culture experiment provides evidence of enhance adhesion of osteoblasts on the nanophase HA. Moreover, cell culture work provides the information on cell proliferation, alkaline phosphatase activity, and concentration of calcium in the extracellular matrix. *In vitro* cellular models have been used to determine the efficacy of HA to serve as bone prostheses [92-93].

2.9 Summary

HA has been extensively investigated towards use as hard tissue replacements in clinical applications. Many methods have been employed to obtain HA with enhanced bio-mechanical properties. Grain size reduction has been designed as an effective

approach to achieve enhanced mechanical properties. Chemical modification such as ion substitution of HA helped to increase the biological properties of the HA implants. The biological performance of HA has been simulated through *in vitro* studies. The results have indicated that the biological performance mainly depends on the phase compositions and surface chemistries.

The relationship between processing and chemistry of nano-structured HA ceramic is not fully understood and hence a thorough study could contribute to future biomedical applications. It is expected that a RF plasma technique is one useful method to produce ultra-fine HA powders in industrial applications. Moreover, the spark plasma sintering technique helps to suppress the coarsening of grains to maintain the nano structure due to fast processing.

Chapter 3 Experimental Techniques

3.1 Spray drying system

A spray drying system was used to produce the starting HA powders. Figure 3.1 showed the schematic diagram of a LT-8 spray drier (Ohkawara Kahkoki Co.Ltd. Yokohama, Japan) used in the present study.

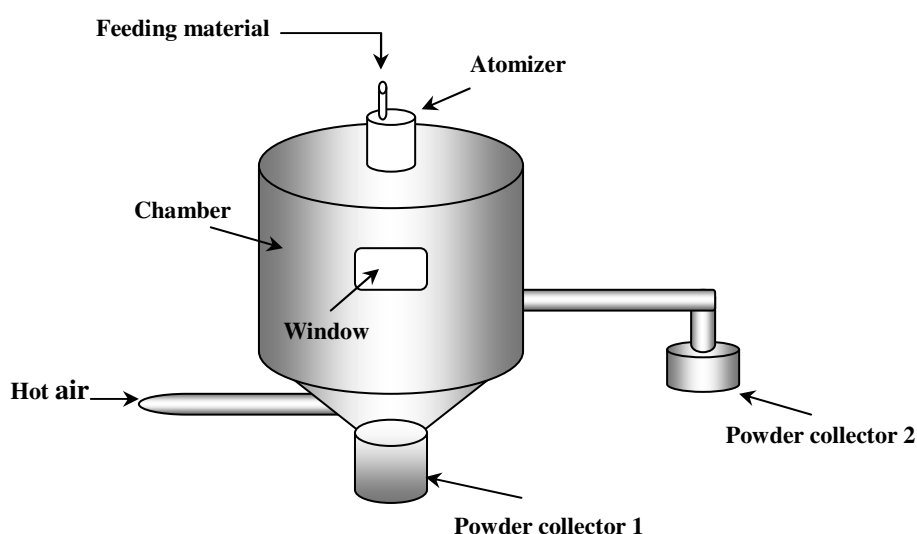


Figure 3.1 A schematic of the spray dryer LT-8.

During spray drying, a slurry containing the finely dispersed material that was to be agglomerated was fed by a pump into a centrifugal atomizer or a nozzle atomizer. The atomized slurry was dried in a stream of cleaned and heated gas (mostly air). The moisture contained in the droplets evaporated during flight in the chamber. The gas was cleaned out in the cyclone. The solid particles were collected in the powder collectors. The centrifugal atomization consisted of a rotating disc. The working parameters were chosen based on the results obtained by Kweh et al [78]. The speed of rotation was set

at 40,000 rpm. The inlet temperature was set at 200 °C. The feeding rate of the slurry was set at 15 ml/min.

3.2 RF induction Plasma System

The plasma processing system (PL-50, Tekna Plasma System Inc., Sherbrooke, Canada) employed for this study consisted of an induction torch and matching radio-frequency power supply equipment, a hermetically sealed cylindrical spray chamber, and a powder feeding system. As illustrated in Figure 3.2, the induction plasma torch used a water-cooled ceramic-plasma confinement tube incorporating a 3-turn induction coil to collect the nano powders. The coil was connected to the radio-frequency power supply (Nihon Kosuha Co., Ltd., Yokohama, Japan) through a tank circuit.

The cylindrical spray chamber (80 cm internal diameter and 100 cm height) was a water-cooled stainless steel structure. The induction plasma torch was fixed at the center of the upper port of the chamber via the bolted flange. There was a window on the front of the chamber, which allowed the visual control of the deposition procedure. The machine was also equipped with oil-filled rotary pumps to enable deposition at low pressure. The exhaust gases extracted from the chamber were first filtered to collect particles followed by wet scrubbing treatment, and finally discharged to the atmosphere.

The powder injector was a water-cooled stainless steel probe located at the torch head; allowing powder to penetrate axially into the plasma flame as shown in Figure 3.3. The position of the probe was adjusted at the center plane of the induction coil. The powders were fed to the torch from a powder feeder where the powder was agitated by

mechanical stirring. A carrier gas would transport the powder through a narrow pipeline to the torch injector probe. The mean powder feed rate was determined mainly by the rotation speed of a drive disk.

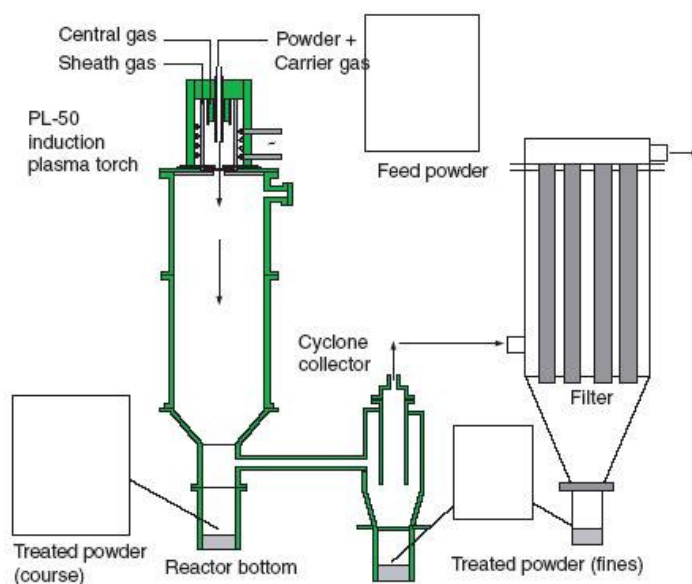


Figure 3.2 A schematic of the radio frequency induction plasma system.



Figure 3.3 A radio frequency plasma flame.

In this study, the working plate power and powder feed rate were adjusted to investigate the properties with respect to the RF plasma processed powders. Other atomization parameters (gas flow rate, angle of atomization, and chamber pressure) were kept constant. Table 3.1 listed the working conditions during the RF plasma thermal spray process.

Table 3.1 Typical Radio Frequency Plasma experimental conditions.

Parameters	Experimental
Central gas flow rate (standard liter per minute)	20
Sheath gas flow rate (standard liter per minute)	50
Carrier gas flow rate (standard liter per minute)	4.5
Plate voltage (kV)	4-6
Plate current (A)	1.8-3.5
Power (kW)	15, 20, 21
Feeder rotary speed (rotation per minute)	5, 10
Powder feed rate (g/min)	2.5, 5.4
Chamber pressure (torr)	400
Probe distance (mm)	35

3.3 Spark plasma sintering system

An SPS-1050 system (Sumitomo Coal Mining, Japan) was used to fabricate the bulk CaP ceramic. Figure 3.4 showed the main components of the SPS. The operating pressure for densification was set at 4.5 Pa. The temperature of the graphite die during sintering was monitored with a pyrometer, which was only able to measure temperatures higher than 600 °C. As such, the cooling rate of the specimen below 600 °C was monitored using a timer. The time needed for the final cooling was around 30 min. The die was then fan-cooled before the insert was removed from the assembly. The total time required for the sintering process (heating and cooling) was about 70-80 min,

while the actual sintering duration was 10 min.

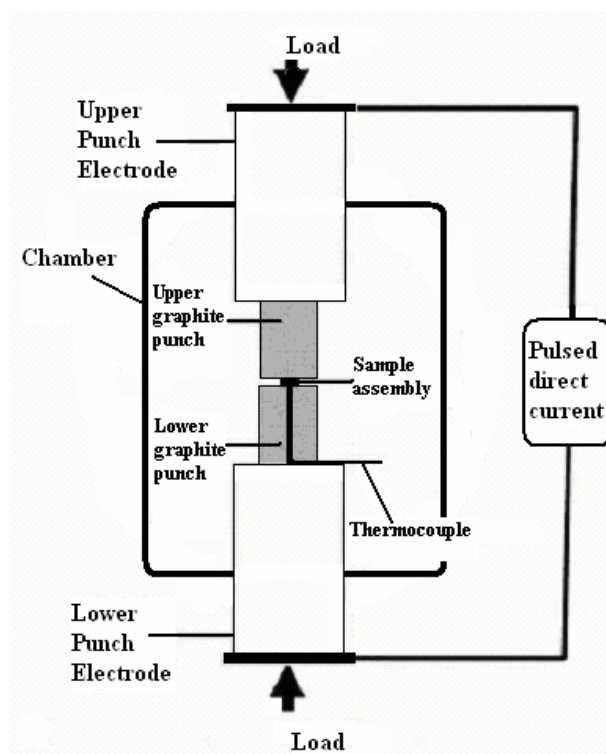


Figure 3.4 Main components of the spark plasma sintering apparatus [61].

The dimensional changes in the sample during the heating stage, under constant load, were monitored through measuring the relative movement between the top and bottom pistons using an in-built displacement gage. The displacement data were recorded from 600 °C onwards, and the data were used to determine the effective sintering stages.

3.4 Dilatometer system

To determine the effects of sintering parameters (sintering temperatures, heating rates, and duration) on the synthesized calcium phosphate powders, a NETZSCH dilatometer (DIL 402 C, Germany) was used in this study. This dilatometer was equipped with alumina sample holders and a high temperature furnace.

The measurements were carried from room temperature to the sintering temperature.

The protective gas was nitrogen with a flow rate of 50 ml/min. The shrinkage was measured in the axial direction. A sample support, Netzsch measuring unit, and displaceable furnace of the dilatometer were mounted horizontally. The length change measurements were made by a transducer, which was maintained at a constant temperature by means of water circulation from a constant temperature bath. The temperature was measured using a calibrated thermocouple, which was placed directly above the sample. A small force of 0.2 N was applied to the sample through the push rod to maintain contact with the sample. The selection of the temperature program was controlled by a computer via a data acquisition system. Correction was applied to the expansion of the system by making a run under identical conditions using a standard sample (Al_2O_3). This calibration together with the reproductibility due to the thermal treatment ran in an accuracy of $\pm 2.5\%$ for the expansivity data.

3.5 X-ray diffraction analysis

XRD was a versatile analytical technique used in research, as a quality control analysis to study crystalline materials. It was performed for a full identification of the different phases present (peak positions), phase concentration (peak heights), amorphous content (background hump) and crystal size/strain (peak width).

An XRD machine (Philips PW1830, the Netherlands) was used to determine and quantify all the phases present on the produced powders and ceramic. The XRD analysis was carried out through the 2θ range from 20° to 60° . It was operated at 30 kV and 20 mA at a scan rate of 0.02 deg s^{-1} .

3.6 Scanning electron microscopy

The surface features and morphology (such as shape and size of the particles) of the powders and the ceramic samples were observed by means of SEM. The JEOL-5600LV SEM, Japan, was used for this purpose. SEM allowed imaging of surface features from 10 to 30,000X with a resolution down to 3 to 100 nm; depending on the samples. Phases on unetched surfaces with different average atomic number can be easily differentiated with a back-scattered electron detector. In case of electron charging, a thin gold layer was deposited on the surface of the samples. This allowed examination of the samples under high vacuum, thus, providing better resolution.

3.7 Transmission electron microscopy

TEM (JEOL 2010, Japan) has also been used to analyze the detailed morphology of ultrafine powders in instances when a resolution beyond capacity of the SEM was required.

The resolution in TEM imaging goes down to 0.2-0.3 nm. The specimen must be “transparent” for the electrons; thus requiring a thickness in the order of 100-200 nm (for 100 KeV Microscope). TEM not only allows microstructural study but it also provides phase analysis of the area that was viewed. The imaging in TEM is made by observation from a transmitted beam.

TEM images and diffraction patterns were being captured via an in-built camera. This allowed the morphological and crystallographic study of the starting feedstock powders and RF plasma processed particles. Diffraction patterns corresponding to different zone axis were obtained and calculated.

For the preparation of the powder samples, the powders were mixed with ethanol followed by 15 min of ultrasonic treatment to separate the agglomerated nano powders. A buret was used to drip the solution to a carbon grid and then left to dry in air before being transferred onto the specimen holder.

3.8 Raman spectrometry

Most investigations in biomaterials were based on histomorphometric techniques and X-ray diffraction. These methods, however, could not provide structural information on a molecular level, as it was required for elucidating the biochemical processes involved in implant integration. In this respect, Raman microscopy was used to probe the distribution among different chemical compounds with a microscopic lateral resolution [120].

In Raman spectroscopy, a laser beam shone onto the surface of the object. Most of this light was reflected back and remains unchanged. However, a small proportion interacted with the molecules in the material, and was scattered. The scattered portion of light, known as the Raman effect, was collected to produce a spectrum. As each material had a unique Raman spectrum, it became a fingerprint to identify materials. However, the Raman effect was quite small. Its use as an analytical tool was limited. The advances, particularly the development of lasers, had overcome the main limitation in Raman spectroscopy. It was used widely to analyze a wide range of materials. These spectra could be used to identify a variety of materials from polymers to precious minerals.

Raman spectroscopy was a non-destructive technique, and allowed recording of spectra from very small samples. A specific design of the laser Raman microprobe,

enabled analyzing even smaller areas in the samples.

Depending on the symmetry of the samples, some vibrations were Raman active and infrared inactive, and vice versa. Hence IR and Raman spectrometry provide complementary detailed information about molecular vibrations, about the molecular environment, and about the crystallization state of the sample. Infrared spectrometry was a transmission method, so the sample had to be thin. The spatial resolution of the Raman technique was 100 times higher than the infrared resolution [18].

However, Raman micro spectrometry provided poor results with amorphous compounds. The Raman signal was about 10^{-6} - 10^{-9} times weaker than the excitation, so the detection of any compound with a concentration lower than 1-5 weight % was impossible. The polarization of the laser beam had a strong influence on the intensity of the Raman bands, so it was impossible to obtain quantitative compositions of the sample using this method.

In this study, Raman spectra of the samples were recorded on the Renishaw Raman Imaging Microscope, United Kingdom. The excitation source consists of a HeNe laser (632 nm). The laser beam was focused onto the specimen using a microscope. The microscope provided a confocal illumination of the sample via a holographic beam splitter. A CCD array detector was employed to detect the optical signals produced by the sample after analysis. Spectral and image data from the CCD was read, stored and processed by a computer, which also controlled all spectrometer functions. The CCD card and system were controlled via a CCD interface card, installed in the PC and connected via a data cable and a 37-way D-type connector to the system.

3.9 Differential scanning calorimetry

Thermal analysis were carried out with a differential scanning calorimetry (Netzsch thermal analysis, DSC 404C, Germany) to investigate the recrystallization temperature of the amorphous phase in the as synthesized CaP powders. The analyses were performed in a nitrogen atmosphere (flowing rate: 150 ml/min). The thermal cycle was set as follows: heating to 1000 °C at a rate of 10 °C/min followed by cooling down to room temperature at a rate of 20 °C/min.

3.10 Micro-indentation test

Micro-indentation (CSEM® MHT, Switzerland) was performed on the SPS samples. The SPS compacts were ground and polished before carrying out the indentation test. The maximum load was of 1 N with a loading rate of 2 N/min. The load was applied for 10 s. The unloading rate was also set at 2 N/min. In order to avoid the stress-strain influence caused by the different indentation, the analysis was taken at least 200 μm apart from each other. The Poisson's ratio (ν) was assumed to be 0.3. The elastic properties of the diamond indenter used in the calculations were $E=1141$ GPa and $\nu=0.07$ according to the CSEM manual. A total of 10 points were averaged for each compacted sample.

The principle of the indentation method was based on the elastic response of a material when load was applied with an indenter onto the specimen. Load and displacement data allowed the E and H of the material to be measured. A schematic representation of load vs indenter displacement was shown in Figure 3.5. The contact stiffness S was measured from the slope of the unloading line.

Figure 3.6 showed a schematic representation of indentation showing various parameters used in the analysis.

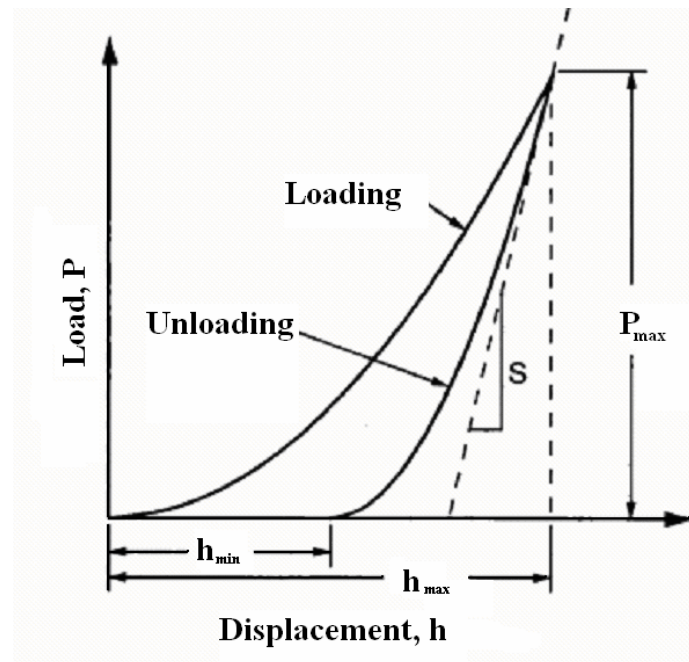


Figure 3.5 Load-displacement curves, showing the maximum indentation depth h_{\max} and minimum indentation depth h_{\min} [121].

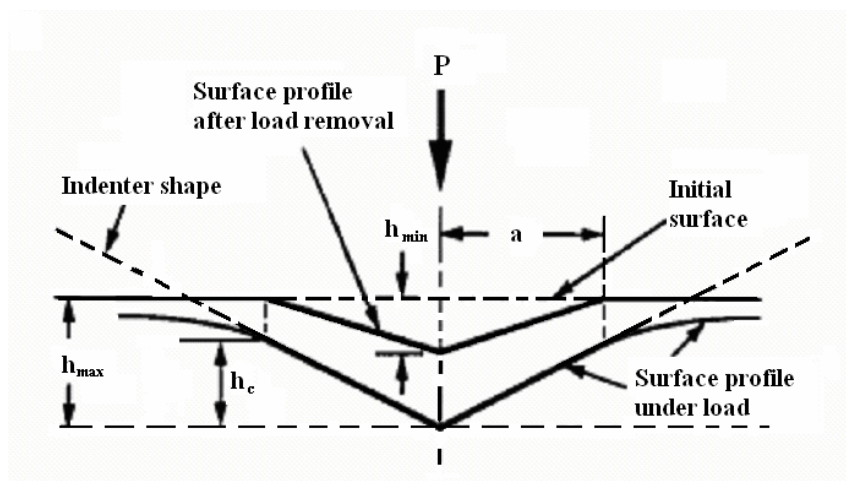


Figure 3.6 A schematic representation of indentation showing various quantities used in the analysis [121].

The contact area was calculated using the following:

$$A = 24.5h_c^2 + \sum_{i=0}^7 C_i h_c^{1/2^i} \quad [3-1]$$

The hardness, which was defined as the mean pressure that the material would support under load, was determined by the following relation:

$$H = P_{\max}/A \quad [3-2]$$

The apparent elastic modulus (reduced modulus) of the sample, E^* , was calculated from the load-displacement curve using standard Hertzian contact theory [141]:

$$E^* = (9/16)^{1/2} P h^{-3/2} R^{-1/2} \quad [3-3]$$

Where h was the depth of the elastic penetration of the indenter, P was the load, and R was the indenter radius. The true modulus of the sample, E , could be calculated from the apparent modulus by taking into account the elastic properties of the indenter:

$$E = (1-\nu^2) / \{ (1/E^*) - [(1-\nu_i^2)/E_i] \} \quad [3-4]$$

Where ν was Poisson's ratio, and the i subscript referred to the indenter.

3.11 *In vitro* tests

In vitro tests were used to study the bioactivities, cell attachment and proliferation on the SPS disks.

3.11.1 Simulated body fluid

Simulated body fluid was used to test the bioactivities of SPS disks by examining the formation of apatite on the sample surface after immersion. The SBF tests were

conducted in a continuously stirred bath containing distilled water with a stable temperature of 37 ± 1 °C. Prior to immersion, the samples were ground to Grit P 1000 and cleaned in an ultrasonic bath with distilled water to remove any loose debris. Each sample was incubated in SBF contained in a glass bottle. After immersion, samples were removed from the bottle and rinsed with distilled water and dried in air. Both solution and samples were kept for the following analysis. The ceramic surface morphology was observed by SEM to disclose the changes of the ceramic.

The SBF solution was prepared according to Kokubo's protocol [122]. Its ion concentration was nearly equal to human blood plasma at physiological conditions of temperature of 37 °C and pH of 7.4, respectively. The ion concentration of the SBF was tabulated in Table 3.2 with comparison to those of human blood plasma.

Table 3.2 Compositions of the SBF solution with the comparison to human blood plasma [122].

Ion	Ion concentration (mM) SBF	Ion concentration (mM) Blood plasma
Na ⁺	142.0	142.0
K ⁺	5.0	5.0
Mg ²⁺	1.5	1.5
Ca ²⁺	2.5	2.5
Cl ⁻	147.8	103.0
HCO ₃ ⁻	4.2	27.0
HPO ₄ ²⁻	1.0	1.0
SO ₄ ²⁻	0.5	0.5

The SBF solutions were prepared according to the following procedures:

- 1 M of HCl solution was prepared.

- All the apparatus used in preparation were cleaned and washed with 1M HCl solution, neutral detergent, and distilled water, and then dried.
- 1 liter of ion-exchanged and distilled water was placed into a beaker.
- The better was stirred constantly with a magnetic stirrer. Each reagent was added one by one, in the order shown in Table 3.3 with the next reagent only being added after the last one had fully dissolved. (Note: only 80 vol % of 1 M HCl was added first.)
- The temperature of the solution in the beaker was adjusted to 36.5 °C by heating a hot plate, and the pH of the solution was subsequently adjusted to 7.4 by stirring the solution and titrating 1 M HCl into the solution.
- The water used to wash the electrode of the pH meter was added back into the solution.
- The solution was transferred from the beaker to a glass volumetric flask. The water used for washing the beaker was also added into the flask.
- The solution volume was made up to 1 liter by adding ion-exchanged and distilled water, shaking the flask at room temperature.
- The solution in the flask was filtered using a 0.22 µm filter and then transferred into a polyethylene bottle, and stored in a fridge at 5-10 °C. If any precipitation was detected during the storage, the SBF solution cannot be used.

Table 3.3 Reagents required for preparing 1 liter of SBF [122].

Order of addition	Reagent	Amount of reagent (± 0.0001 g)
1	NaCl	7.996 g
2	NaHCO ₃	0.350 g
3	KCl	0.224 g
4	K ₂ HPO ₄ ·3H ₂ O	0.228 g

5	MgCl ₂ .6H ₂ O	0.305 g
6	1M HCl	40 ml
7	CaCl ₂	0.278 g
8	Na ₂ SO ₄	0.071 g
9	NH ₂ C(CH ₂ OH) ₃	6.057 g

3.11.2 Cell culture

The SPS samples were ground till Grit P 2400 finish and sterilized via autoclaving before proceeding to cell culture work.

The cell line used was established by transfection of human limb tissue obtained from a spontaneous miscarriage with the temperature sensitive expression vector and the neomycin resistance expression vector. Clones were selected in the presence of 0.6 mg/ml G418.

Table 3.4 tabulates the components used for the preparation of cell culture medium. For experiments, osteoblasts were seeded at 2×10^4 cells/cm² onto SPS disks in an incubator at 37 °C in the presence of 5 vol % of CO₂. Medium was changed every 2-3 days.

Table 3.4 Components in the cell culture medium for osteoblast propagation.

Components	Volume (ml)
DMEM/F12	500
FBS	50
Antibiotics	5
G418	3
L-glutamine	3

To understand and to analyze cell attachment and cell differentiation under SEM, the SPS disks with the cell attached on their surface needed to be fixed. Before fixation, the samples were removed from the culture medium, and were rinsed with PBS. The specimens were then fixed in 2.5 vol % glutaraldehyde buffered in 0.1 M sodium cacodylate (pH 7.3-7.4) for 1 hr at $\sim 4^{\circ}\text{C}$. The next step was to rinse the samples in the 0.1M sodium cacodylate buffer for 5 min followed by 30 min treatment in 1 weight % tannic acid in 0.1 M sodium cacodylate at 4°C . They were still washed in sodium cacodylate buffer before post fixation with 1 weight % OsO_4 buffered in 0.1 M sodium cacodylate for 30 min at 4°C . Following post fixation, the samples were rinsed with distilled water for 10 min, and dehydrated in a graded series of ethanol for 5 to 10 min at room temperature. Finally, samples were immersed in increasing concentrations (50 vol %, 70 vol %, 100% and 100%) of HMDS, which was a mixture of HMDS and ethanol, for critical point drying. After removing the HMDS solution and drying the sample in the dryer, they were gold sputtered for 120 s at 10 mA to allow observation under SEM.

A colorimetric assay was used to quantitatively determine cell proliferation and viability on the ceramic. It was a test based on the capacity of viable cell to metabolize “tetrazolium” to “formazan crystals”. The amount of formazan crystals was directly proportional to the total number of living cells as it turned to spread blue color. Its concentration could be easily measured at 490 nm using a microplate reader. The osteoblasts were seeded onto each ceramic surface at a density of 2×10^4 cells/cm² in a 24-well plate. On the preset days, 0.2 ml of medium was sucked out, and 0.2 ml of colorimetric solution was added to each well and the plates were incubated at 37°C for 2 hrs. After the supernatants had been discarded, the dark blue crystals of formazan were dissolved by adding 0.4 ml of dimethyl sulfoxide, and were quantified

spectrophotometrically at 490 nm using the microplate reader. As a control, osteoblasts with a density of 2×10^4 cells/cm² were also seeded in the well and chemically reacted with the colorimetric solution. Using the standard curve, the results were converted to living cell number.

AKP activity was a widely recognized biochemical marker for osteoblast activity. It was commonly studied to assess osteoblast differentiation. AKP catalyzed the hydrolysis of phosphate esters at an alkaline pH and was believed to play a role in skeletal mineralization [193]. An AKP reporter gene assay kit was employed in this study to determine the secretion of AKP of osteoblasts after cultured on the SPS disks. To perform the assay, the cells were seeded onto different disks and cultured. Since the osteoblasts secreted AKP, the medium was collected for analysis after culturing for 2 and 6 days. A serial dilution of the control enzyme was prepared as positive control group. A medium with no secreted AKP was prepared as a negative control group to indicate the background level. Those media (collected medium, positive control medium and negative control medium) were incubated at 65 °C for 30 min. The majority of the protein products of AKP genes, cloned in order to serve as reporter genes, were stable at 65 °C. After cooled to room temperature within 2 min, MgCl₂ solution and Fluorescent assay buffer solution with a volume ratio of (1:8) was added in the solution. After mixed with the substrate, a fluorometer with an excitation of 360 nm and an emission of 440 nm was used to measure the absorbance intensities. Five readings were averaged for the AKP results.

3.12 Other methods

The particle size distribution and mean particle size were measured using a Laser

Particles Analyzer (Fritsch 22, Germany). Zeta Potential was used to analyze the nano particles size distribution. The specific surface area of the synthesized powders was determined by the BET method using a Micromeritics Surface area analyzer (ASAP 2010, USA).

The atomic ratio of calcium and phosphorus in the powders and ceramic chemical analysis was determined through XPS. XPS spectra were recorded on a Kratos spectrometer using Al K $\alpha_{1,2}$ (1486.6 eV) as a excitation energy. The pressure was about 10^{-9} Pa.

The density of the SPS sample was measured with the weight scale system upon immersion in ethanol. The ADA 210/L balance (Adam Co. Ltd., UK) equipped with a density kit and software for analysis was used. To avoid ethanol from entering into the samples' pores and yield large values, transparent oil paint was used to cover the samples. After immersion in the SBF, the ion concentration in the solution was measured with the ICP atomic emission spectrometer (IRIS, Intrepid, USA). An average of three measurements was taken for each sample.

Chapter 4 Spray Dried HA and Silica doped HA (SiHA)

Introduction

Micrometer sized hydroxyapatite (HA) and silica doped HA (SiHA) powders were used as feedstock for producing RF plasma processed CaP powders and spark plasma sintering ceramic. There were numerous synthesis methods for producing conventional sized HA powders. The precipitation route appeared to be the most common techniques. Among the range of precipitation routes, the reaction of: (1) diammonium hydrogen phosphate with calcium nitrate; and (2) orthophosphoric acid with calcium hydroxide, were the two most popular. The first method required the use of aqueous ammonia to maintain the pH of the reaction at around 9. The major disadvantage of this method was that the purity of the precipitated HA powders was affected by the purity of the calcium nitrate. Furthermore, the excess ammonia and ammonium by-products must be removed by extensive washing. In contrast to the first method, the second method was a more convenient process and suitable for the industrial production of HA since the only by-product was water. In this project, the second precipitation process was selected for the production of HA powders.

Preliminary studies have noted that the reaction temperature, the reactants concentration, rate of mixing reactants and the residence time can affect the overall characteristics of the HA produced [78, 123, 124]. Appropriate working parameters were selected to produce the stoichiometric HA slurry according to the previous studies [78, 123-124].

4.1 Preparation

Calcium hydroxide (Riedel-de-Haen, AG Germany) and orthophosphoric (Merck, AG Germany) were used to synthesize hydroxyapatite.

The HA slurry was obtained from the chemical reaction of calcium hydroxide and orthophosphoric acid according to the reaction formula [4-1]:



According to the chemical formula, 592.72 g of Ca(OH)_2 and 553.41 g of H_3PO_4 were dissolved in eight liters of distilled water to form 1 M Ca(OH)_2 and 0.6 M H_3PO_4 solutions, respectively. The calcium hydroxide solution was put in a water bath. It was heated to $40 \pm 5^\circ\text{C}$ to accelerate the reaction. During the reaction, the solution was stirred mechanically to ensure uniform mixing. To obtain a gelatinous HA suspension, the acid of 0.6 M H_3PO_4 was dripped into the alkaline bath to achieve a pH of 9. The drip rate of the acid was controlled at 0.9 liter/hr by a mechanical pump.

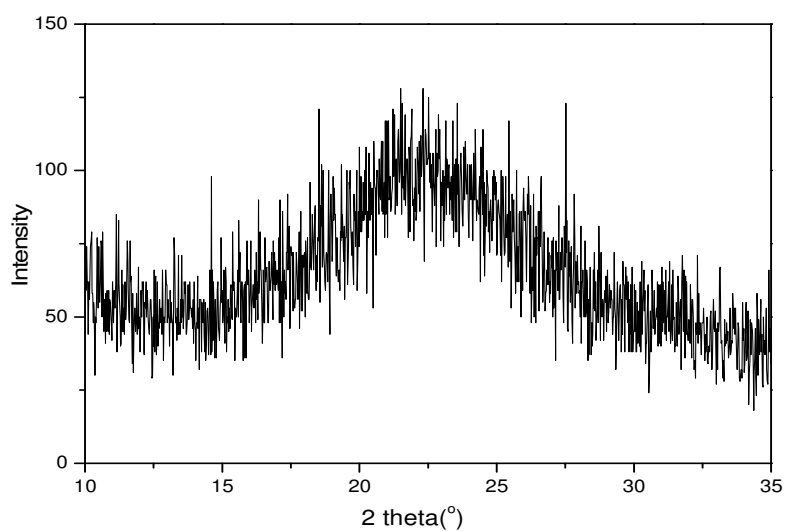
In the course of the reaction, which took approximately 8-9 hrs, the pH of the solution was monitored by a computerized pH detection system (HI 9017 microprocessor pH meter, Hanna Instruments, Portugal). After reaching a pH of 9, the acid addition was stopped. The resulting gelatinous precipitate was then stirred for two more hours and left overnight to settle. To obtain spray dried SiHA, silica as preset weight (0~5 wt%) was added into the HA slurry. The introduction of silica resembled the levels detected in natural bone mineral. The slurry was stirred for 4 more hrs before transportation into the spray dryer.

4.2 Results

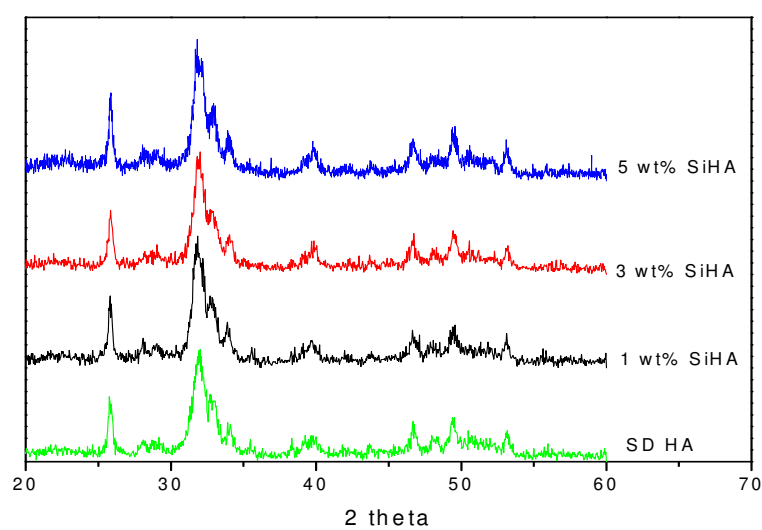
4.2.1 Phase compositions of the powders

The phase purity of the as synthesized HA and SiHA powder was analyzed after spray drying. The XRD patterns of the spray dried powders and that for the original silica used were shown in Figure 4.1. Only a broad hump centered about 22° was detected in the silica, which indicated that silica precipitated was made up of amorphous phase.

The positions of the peaks and their relative intensities of the spray dried powders corresponded to the data of the JCPDS files for HA (9-432). There was an absence of other calcium phosphate or other undesirable phases, such as TCP or CaO in the XRD patterns. The relatively broad peaks in the spray dried powders indicated that the spray dried powders consisted of relatively fine particles. The source powder exhibited a low degree of crystallinity, which was known to be a typical characteristic of calcium phosphate being synthesized by the wet method. However, after calcination, as shown in Figure 4.2, the powder exhibited a substantial increase in peak height and an associated drop in peak width, which corresponded to an increase in crystallinity. The correspondence to JCPDF 9-432 fit well for all peaks with 2θ angles ranging from 20° to 60° . It was reported [78] that the effect of calcination might actually be involved in increasing the overall crystalline size. Therefore, the sole effect of increasing crystallinity could not be isolated easily. To test the thermal stability of the spray dried HA powders, higher temperature annealing was carried out at 1000°C in air for 5 hrs with furnace cooling. As shown in Figure 4.3, no new phases were formed after the calcination, which indicated that the powders were quite stable after spray drying process.



(a)



(b)

Figure 4.1 XRD patterns: (a) silica precipitated; (b) spray dried powders doped with different dopant level of silica.

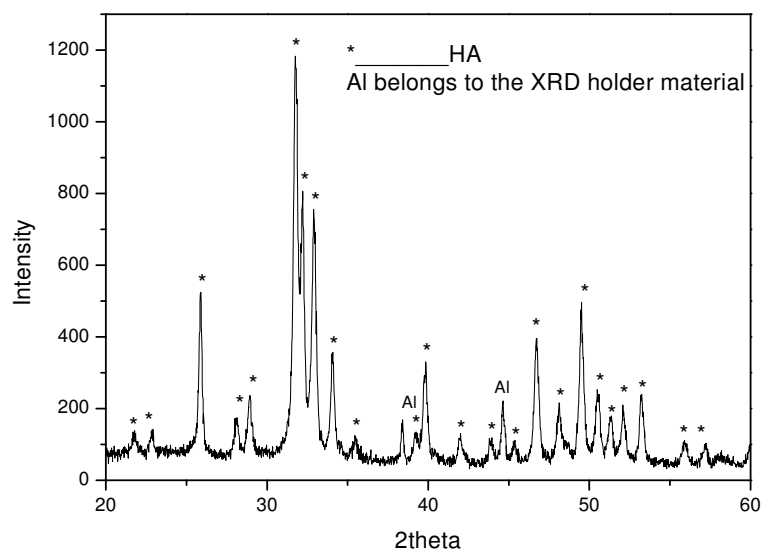


Figure 4.2 XRD pattern of spray dried HA powders after heat treatment at 850°C in air for 1.5 hr.

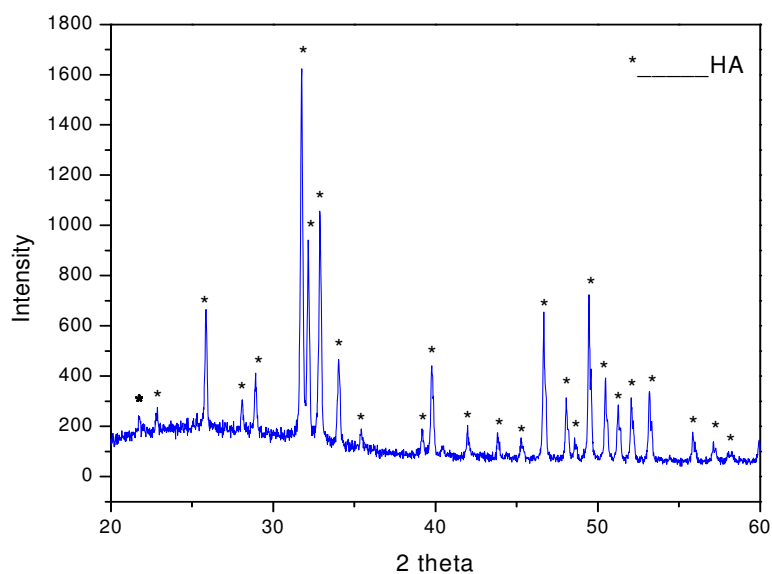


Figure 4.3 XRD pattern of spray dried HA powders after heat treatment at 1000°C in air for 5 hrs.

4.2.2 Raman spectra

The powders were subjected to Raman analysis. The results were supportive and complementary to the XRD results described in the previous section. The spectrum of

HA contained the phosphate bands and the bands due to hydroxyl ion stretching and vibrational modes. The vibrational spectra of calcium phosphates exhibited a strong molecular character associated with the internal modes of the PO_4^{3-} tetrahedra. At room temperature apart from the hydroxyl bands, calcium phosphate had ν_1 , ν_2 , ν_3 and ν_4 bands. Those bands appeared above 400 cm^{-1} [125]. The ν_1 frequency corresponded to the symmetric stretching of the P-O bonds, whereas the ν_3 frequency arose from the triple degenerate mode involving asymmetric P-O stretching and P motion. The ν_2 frequency corresponded to the double degenerate O-P-O bending modes. The ν_4 frequency was due to the triple degenerate modes of mainly O-P-O bending character [126].

The Raman spectrum of spray dried HA powders after heat treatment at $850\text{ }^\circ\text{C}$ was presented in Figure 4.4. In this spectrum, the vibrational bands of HA were observed. PO_4^{3-} peaks were present at 429, 449, 580, 594, 608, 961 and $1000\text{--}1130\text{ cm}^{-1}$. The peak at 3573 cm^{-1} corresponded to the stretching frequency of OH^- ions of HA.

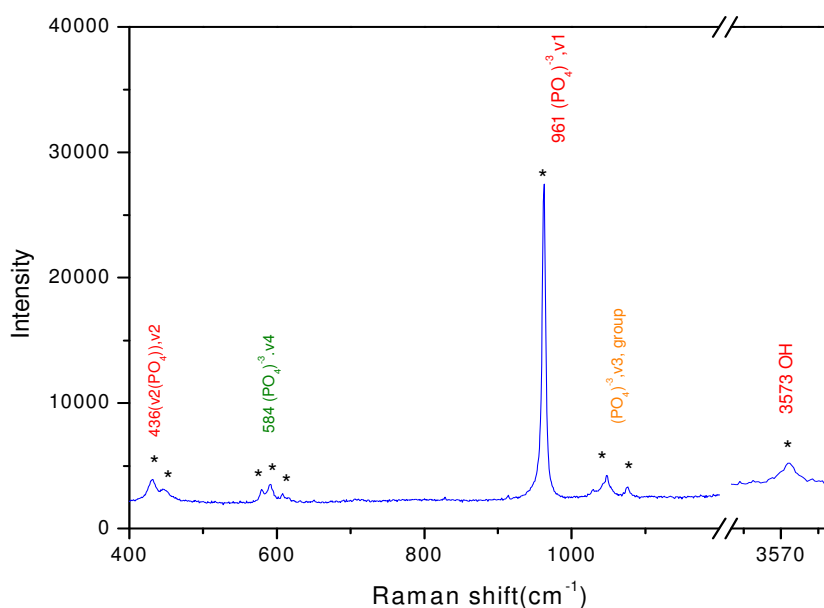


Figure 4.4 Raman spectrum of synthesized spray dried HA powders after heat treatment at $850\text{ }^\circ\text{C}$ in air for 1.5 hr.

The silica doped HA powders were also tested with the Raman spectrometer. The result was shown in Figure 4.5 (a). It was noted that no significant difference could be claimed among the spray dried powders. However, the intensity of peaks locating around 490 cm^{-1} in 5SiHA powders changed slightly when compared to other powders samples. To certify this peak, the Raman spectrum of the silica was presented in Figure 4.5 (b) as reference information. The silica sample exhibited vibrational modes due to the bending mode of Si-O-Si near 480 cm^{-1} and the Si-O-Si symmetric stretch at around 690 cm^{-1} . The peak near to 1046 cm^{-1} should be attributed to the asymmetric Si-O-Si stretch [127].

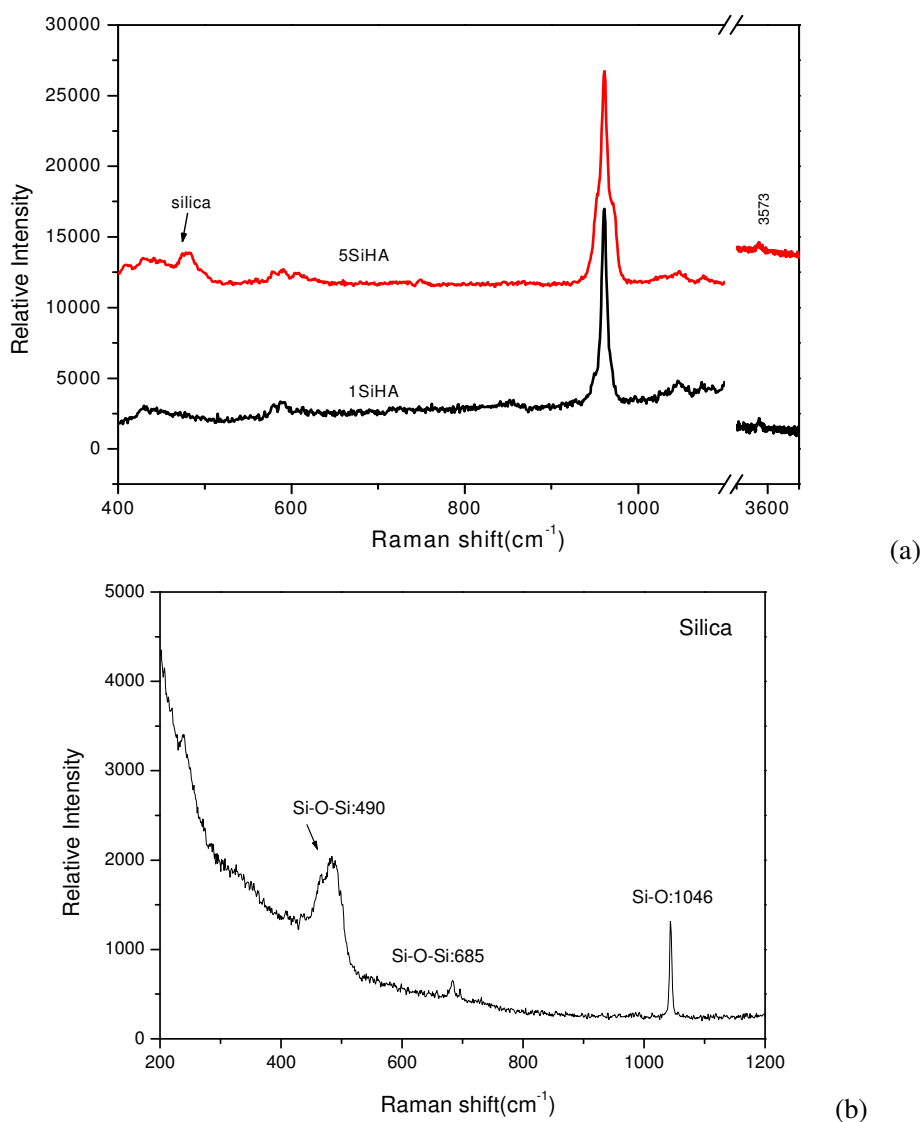


Figure 4.5 Raman spectra: (a) silica doped HA powders; (b) silica precipitated.

4.2.3 Morphology and size distribution

Particles used for the morphological investigation were directly obtained from the spray dried powders. The high vacuum operation mode of SEM was used to provide higher resolution images. The SEM sample was coated with gold using the conventional procedure for the SEM process to make the powder sample conductive.

Figure 4.6 (a) showed HA powders with rather spherical shape with micro-pores homogeneously distributed. The magnified view in Figure 4.6 (b) further ascertained the highly porous nature of the SD HA powders.

Figure 4.6 (c) showed the high magnification SEM micrograph of the SD HA powders. It revealed that the powders were made up of nano-sized particles with needle shape. After heat-treatment at 850 °C for 1.5 hr, the HA particle shape was shown in Figure 4.6 (d) with a more rounded morphology in comparison with the particles (shown in Figure 4.6 (c)) that did not experience any heat treatment.

The results from the laser particle size analyzer indicated that all the powders have median diameters of 14-17 μm . The processing steps used for all materials resulted in similar particle size distributions, regardless of the level of doped silica. This implied that the low amount (<10 wt%) of silica didn't influence the separation of HA during the spray drying steps. A typical picture of the particle size distribution was shown in Figure 4.7. It was found that the median particle size of spray-dried HA powder was about 15.86 μm . From the two main peaks of the size distribution graphs shown in Figure 4.7, it could be concluded that around 10 vol % of the powders were less than 5 μm and 90 vol% of the powders fall in the range of 5-40 μm .

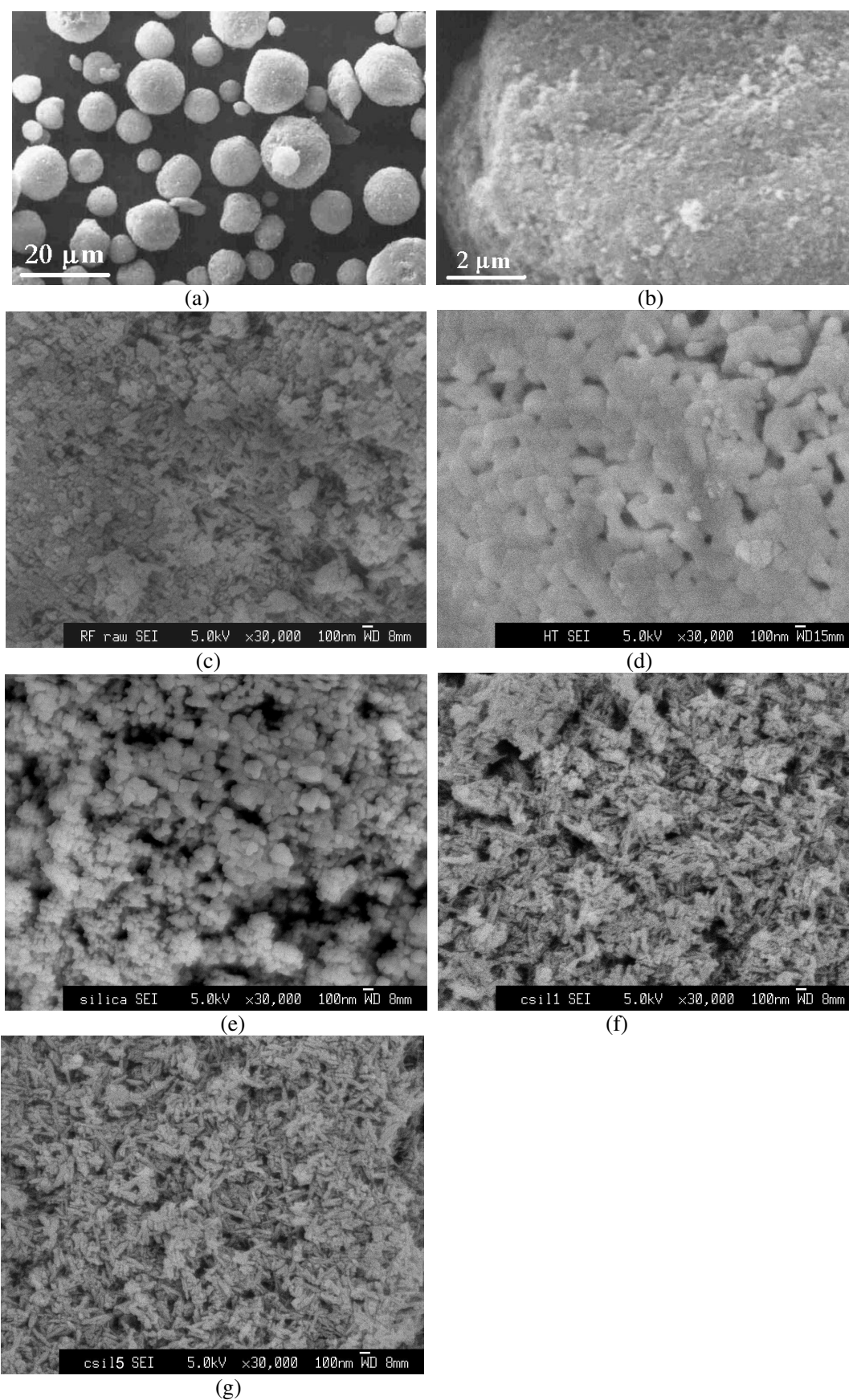


Figure 4.6 SEM morphologies of SD HA (a-c); heat treated HA (d); Silica(e); 1 wt% SiHA (f) and 5 wt% SiHA (g) powders.

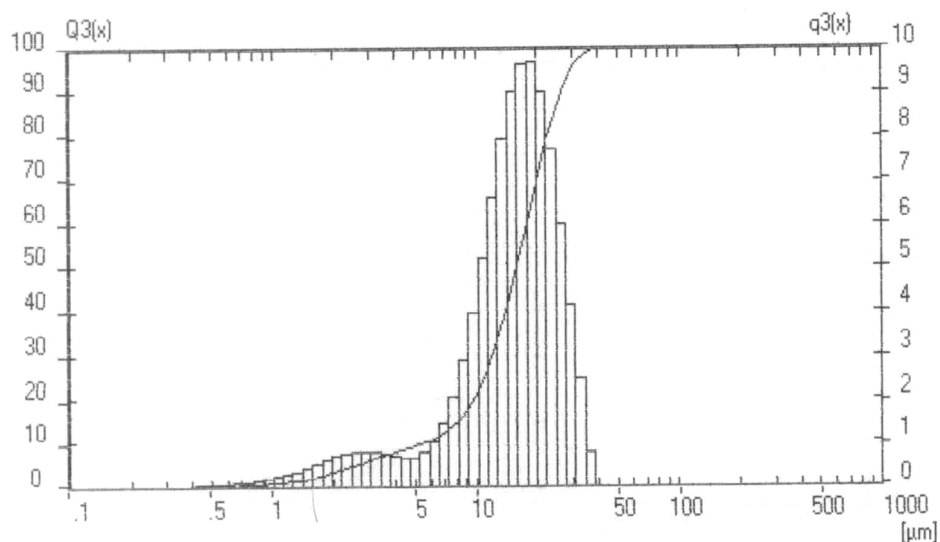


Figure 4.7 Particle size distribution of spray dried HA powders.

4.2.4 TEM analysis

TEM was used as a complementary method to identify the crystallographic phases of individual particles in spray dried HA powders. The typical TEM result in Figure 4.8 (a) showed that spray dried HA powders were mainly made from fine particles. The electron diffraction patterns of the selected area were shown in Fig 4.8(b). As was evident from the appearance of rings, the powder was polycrystalline. It should be noted, however, that the rings did not appear as completely continuous ring. This aroused because that there were several grains in the selected area.

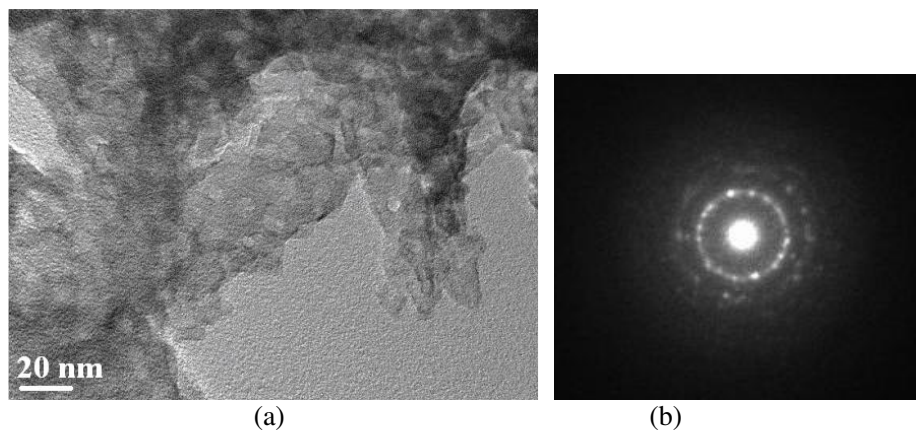


Figure 4.8 TEM images of fragment from Spray dried HA powders (a) and the SAD of the HA (b).

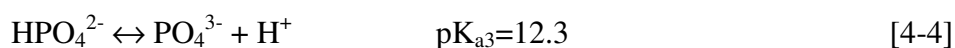
4.3 Discussion

4.3.1 Reaction conditions for stoichiometric HA

The effect of synthesis temperature on the particle shape of HA has been reported [123]. It was found that at low synthesis temperature (~35 °C) the crystals carried a needle-like shape corresponding to the c-axis of the HA structure. Increasing the reaction temperature to 85 °C changed the crystals from a needle shape to a more round shape.

The pH value was a very sensitive parameter to the stoichiometricity of hydroxyapatite. It was noted [78] that the pH at about 9 would produce correct conditions whereby only pure, single-phase HA was formed. Below a pH at 9, i.e., at pH 5 or 7, traces of TCP were detected. A high addition rate of phosphoric acid (> 2 liter/hr) or in excess could lead to the formation of calcium deficient precipitates. However, if the slurry suspension pH swung to the other extreme of pH 11, traces of CaO were identified [78]. The high Ca/P ratio (>1.7) may have resulted in the decomposition of calcium hydroxide into calcium oxide. As discussed by Bouyer [123], the morphology of the HA particles depended strongly on the addition rate of reactant during the reaction synthesis. The addition rate also had a strong influence on the composition. A higher addition rate of acid, such as higher than 2 liter/hr, systematically resulted in an increase of the Ca(OH)₂ content that was not desired. This might be explained in terms of pH of the reaction media. When the acid was introduced at a very high addition rate of >2 liter/hr, the pH of the reaction media decreased drastically (pH<7). Orthophosphoric acid was a weak triacid, the acidity potentials were as follows:





If $\text{pH} > \text{pK}_a$ then the dissociation of H_3PO_4 would occur according to the Le Chatelier principle [123]. In the other case the recombination would occur. Therefore, when the acid was introduced in the reaction media in a high addition rate, the pH decreased leading to an incomplete dissociation of orthophosphoric acid. In the absence of PO_4^{3-} , the formation of HA structure was compromised.

Therefore, the favorable synthesis condition of pure HA was a moderate acid addition rate coupled with a reaction temperature at around 40 °C. This related to a pH of 9 at the end of the reaction.

4.3.2 Structural and compositional study of the powders

As shown in Figure 4.6, pores were detected in the spray dried powders. The high degree of porosity was due to the elimination of the moisture and gases during the spray dried process at elevated temperature of 200 °C. The pores in the powder might compromise the flowability, heat transfer and consistent melting capability during the further plasma processing. These porosities appeared as small surface depression, which may be minimized and the material restored to a denser structure through calcinations or sintering [78].

The ultra fine particles under high resolution SEM indicated that the spray dried powders were made of nano-structured particles; corresponding to the results obtained from TEM analysis.

In order to compare the needle shaped particles with the nearly spherical particles after heat treatment, a shape factor was defined by the ratio length/width of the HA

nanocrystals as discussed by Bouyer et al [123]:

$$F_s = L/w \quad [4-5]$$

where F_s , the shape factor; L , particle length [nm]; and w , particle width [nm]. The shape factor, F_s , of the HA nanocrystals decreased with an increase in the synthesis temperature [123]. The as-spray dried needle shape particles had a shape factor of around 5~6 in this study. The heat treated particles were very dense and have an F_s of 1 due to the sintering of the particles. The increase of the shape factor would lead to the decrease of specific surface area of the particles [123].

After heat treatment, visible color change from white to light blue was seen after calcination. According to Berndt and Gross [128], the color changes were due to the presence of manganese ions or other transition elements located in the crystal lattice structure. Although the color change may not have any significant effect on the biocompatibility of HA, the consumer acceptance would not be positive.

XRD results confirmed the apatite structure of all the spray dried powders. After heat treatment at 850 °C and 1000 °C, no secondary phases were detected in the spray dried powders. These results indicated that the obtained HA was of high purity. This HA was stable without decomposition when it was heat-treated at 1000 °C for 10 hrs (Data not shown).

As observed under SEM, the spray dried powders were agglomerated from randomly distributed ultrafine particles. The structure of these ultrafine particles, such as grain size, had important effects on the properties of the material. The XRD peak was strongly affected by the structure of aggregates of the powders and yielded information about the grain size. By analysis on the changes of shape or intensity in diffraction peaks, it was possible to recognize the internal structure change of the

material. According to the Scherrer equation [90], the relationship between crystalline grain size (D) and the full width at half-maximum (FWHM) of the diffraction peak was expressed by:

$$D = 0.9\lambda / \Delta(2\theta) \cos\theta \quad [4-6]$$

Where λ was the wavelength of X-ray, and θ was the diffraction angle. $\Delta(2\theta)$ was the true peak broadening. The narrower the peak width, the larger the grain sizes. Thus, the sharper peaks intensities in XRD patterns of heat treated powders revealed that the heat-treated powders had a relatively larger grain sizes than those without heat treatment.

During the growth stage of the HA structure in the suspension, the nonuniform micro-strain in the powders caused by the formation of defects would also result in the peak broadening. Annealing could remove this residual stress and as a result, the diffraction peaks became sharper, as shown in Figure 4.4. The SEM results in Figure 4.6 indicated that heat treatment had led to the transforming of needle shaped particles to regular and relatively large particles.

It was difficult to distinguish the HA and SiHA phases by XRD. Also, some low level impurities may not be detected by XRD, especially if their patterns were overlapped by stronger patterns. Therefore, Raman analysis was carried out to identify individual constituent crystalline phases in the synthesized powders, including possible impurities. As shown in Figure 4.4, it was observed that the Raman spectrum of the ν_1 band had only one peak at 961 cm^{-1} , and it was very intense. According to Cusco et al [126], the different number of ν_1 peaks could be used to differentiate the presence of HA phase from other calcium phosphates. In this study, the presence of only one peak at ν_1 of phosphate ions at 961 cm^{-1} showed that the pure phase of HA

existed in the HT spray dried powders. No other peaks, such as the peak at 875 cm^{-1} assigned to HPO_4^{2-} , were observed, which also indicated the purity of the obtained spray dried HA powders. Both the XRD and Raman results indicated that the used parameters for the formation of HA slurry were suitable for the production of stoichiometric HA.

The Raman patterns from the spray dried powders showed that the patterns were consistent only with the calcium phosphates. However, combining with the Raman patterns shown in Figure 4.5, the marked peaks at around 490 cm^{-1} in 5SiHA powders belong to the bending mode of Si-O-Si, which were due to the relatively high content of silica. The presence of silica did not change the peaks positions of the phosphate group. This indicated that the structure of HA was not influenced by the doped silica, and no chemical reaction occurred between the dopant and HA.

4.3 Chapter summary

Hydroxyapatite and silica doped hydroxyapatite slurries were prepared through wet chemical reaction methods. The slurries were spray-dried into nearly spherical powders using a spray drier. The obtained spray dried powders were characterized through different methods. The results indicated that only an apatite structure was obtained in the spray dried powders. The thermal stabilities of the spray-dried HA powders were investigated through heat treatment. The shape factor of the obtained spray dried powders was influenced by heat treatment due to the sintering of the particles. These powders will be used as feedstock for the production of RF plasma synthesized powders and SPS ceramics.

Chapter 5 Production and Characterization of Radio Frequency Plasma Synthesized Calcium Phosphate powders

Introduction

During the radio frequency (RF) plasma process, the feedstock was axially injected into the plasma region. It experienced melting, evaporation, sintering and fusion, rapid solidification and condensation. The whole process took about 100 milliseconds depending on the size of the plume and the particle velocity in the plasma [129]. Particle thermal history in the plasma would greatly influence the characters of the powders obtained. Two situations could develop, depending on the processing history of the particles. One situation was that micrometer sized feedstock underwent surface melting, and some of them melted completely. Their final diameters would be obtained upon reaching the tail end of the plasma. The other situation was that the vaporized materials condensed into the nano-sized particles.

The rate of heat transfer to each particle by conduction, convection and radiation as a function of logarithmic time for particles under various working conditions had been reported [129]. It was claimed that the heat transfer rate depended on the plasma temperature, the particle characteristics and residence time in the plasma. Normally, for a given material, the higher the plasma temperatures and the larger the particle size, then the higher the heat transfer rate. It should be mentioned that the heat transfer mechanism with the particle interaction was a very complex phenomenon [84], which has been studied extensively but not fully understood.

The morphology, structure, and composition of formed RF plasma processed powders may be well understood when they were related to the process of RF plasma

spray techniques. Variations in working parameters of RF plasma processing could affect the decomposition of nano and micrometer sized particles. Kumar et al [130] had concentrated on investigating the influence of various RF plasma parameters (plate power, chamber pressure, plasma gas flow rates and probe position) on the characteristics of the as-synthesized powders. It was reported that the plate power would influence the decomposition of HA during the RF plasma flame. Two of the most important working parameters, working plate power and powder feed rate, were investigated in the present study. Those two parameters influenced significantly the properties of the formed powders. In the following sections, details of the working conditions, characterization of these formed powders were discussed.

5.1 Production of Radio Frequency plasma CaP powders

The characterization of spray-dried feedstock that was used for the synthesis of finely spherical CaP powders had been elaborated in Chapter 4. In order to make the spray-dried powders easy to transport into the RF plasma flame, they were dried in an oven at 80 °C for 12 hrs to remove any absorbed moisture and improve their flow ability.

The spray dried powders were fed axially into the RF plasma by a special powder feed system. They were agitated by mechanical stirring, and then conveyed by the drive disk to the metering orifice. The process-carrier gas transported the powders through a narrow pipeline to the torch injector probe. The mean powder feed rate was determined predominantly by the rotation speed of the drive disk [85]. Based on the weight of synthesized RF plasma powders at a fixed period, the mean powder feed rate was calculated for various rotation speeds of the driver disk.

For the purpose of revealing the influence of working parameters on the formed

powders, working plate power and powder feed rate were adjusted to obtain the best results. Other atomization parameters were kept constant.

In a previous investigation on the RF plasma spray process, it was reported that powders with different size ranges were produced [94, 96]. The RF plasma synthesized powders collected, separated into two kinds of particles: one was micrometer sized but nano-structured particle, and the other was nano-sized powder. In this research, both of these powders were investigated.

The results were discussed primarily based on the ‘thermal history’ and/or physico-chemical of the powders sprayed at the various RF plasma spraying parameters. The chapter aimed, in a broad sense, to address the basic relationships between plasma parameters and the physico-chemical and thermal characteristics of the obtained powders. The characterization of the powders included the morphology analysis, structure and composition analysis, particle size analysis, and thermal analysis.

5.2 Characterization of RF plasma processed spherical powders

5.2.1 Results

5.2.1.1 Morphology analysis and particle size analysis

Figure 5.1 (a) presented a typical SEM image of RF plasma synthesized powders that were obtained at a working power level of 21 kW, and powder feed rate of 5.4 g/min. The surface of the powder was covered with very fine particles that were condensed from the evaporated feedstock. The powders have roughly two size-ranges: ~1-10 μm and 10-100 nm particles. The larger particles were within the micrometer size and predominantly spherical in morphology. Due to the size effect and van der

Waal's forces, the nanometer-size particles adhered to the surface of the larger ones.

As presented in Figure 5.1(b), some hollow-structured particles were detected within these RF plasma processed powders. Since thermal plasma ensured the adequately high temperature for the ceramic particles to melt, water vapor or other gases liberated from the agglomerates were supposed to cause the thermal cavity as shown in Figure 5.1 (b).

The finer particles in the powders were characterized under high magnification SEM and presented in Figure 5.1 (c). It was found that the fine particles were about 100 nm. Finer particles were analyzed using a TEM system. Samples were prepared through the following procedure. The HA slurry, prepared with spheroidized powders, was prepared by ethanol. The slurry was then filtered through a fine perforated disc. A grid with carbon film for TEM was dipped in the ethanol solution to analyze the filtered fine particles. After the evaporation of the ethanol, the finer particles were left on the grid and analyzed by TEM. The result, Figure 5.1 (d) indicated that the size of the fine particle was within the nanometer region, which corresponded to that of high magnification SEM analysis.

The cross-section of spheroidized HA powders were presented in Figure 5.1 (e). It was found that the spheroidized particles were either a fully dense or hollow structure with a shell. The fully dense particles were contributed to the fully melted particles in the plasma flame. Some unmelted particles were also detected, which were mainly from the feedstock entered the outer layer of the plasma flame where the temperature was not high enough to melt the feedstock.

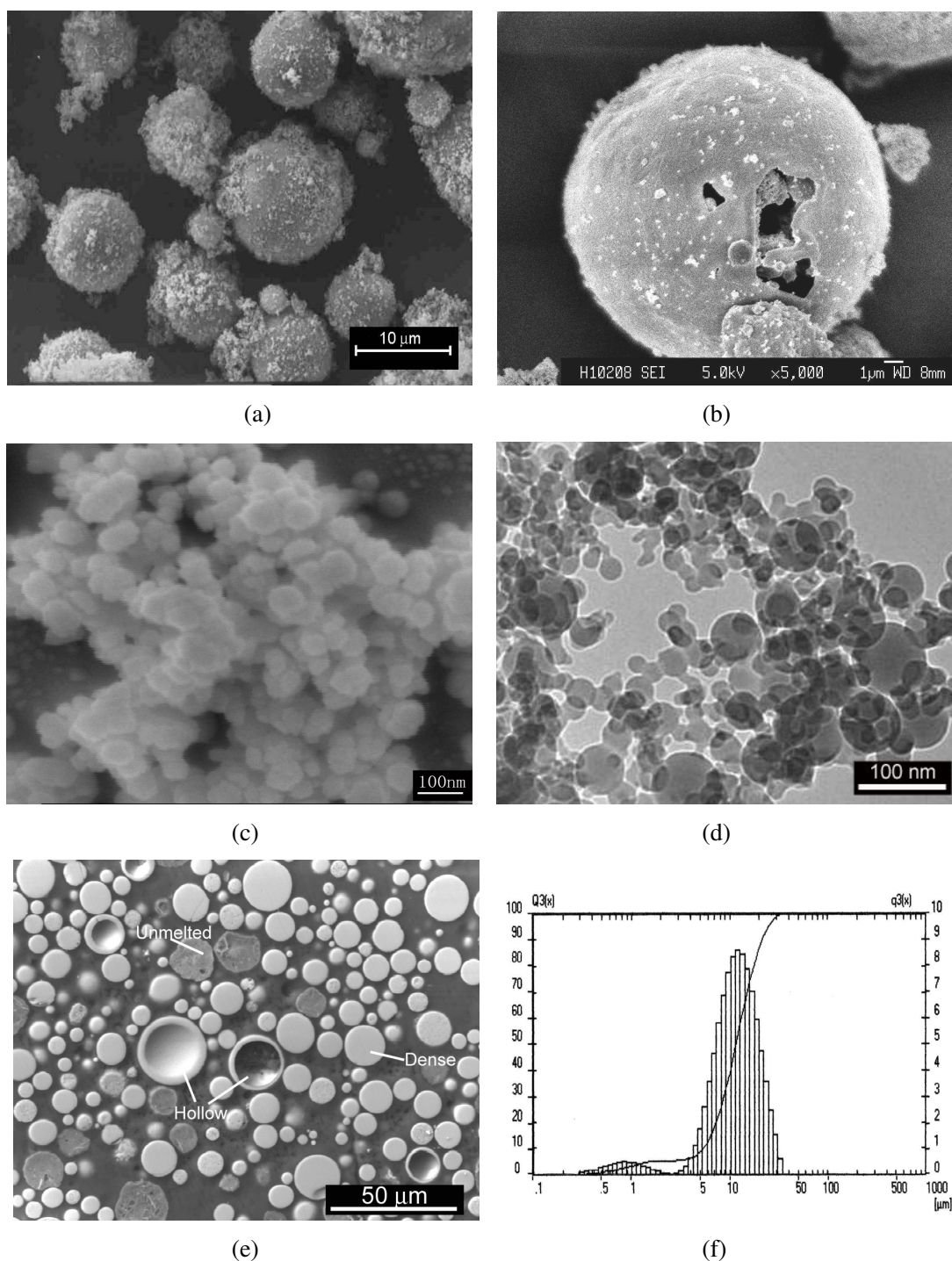


Figure 5.1 Morphologies of: (a) Spheroidized HA powders under SEM; (b) Hollow-structured powders under SEM; (c) Fine particles filtered from spheroidized powders under high magnification SEM; (d) Fine particles filtered from the spheroidized powders under TEM; (e) Cross-section of spheroidized powders under SEM; and (f) Particle size distribution of spheroidized powders.

5.2.1.2 Phase composition studies

The XRD patterns of the spheroidized powders were shown in Figure 5.2. The peak positions matched closely to the diffraction peaks of stoichiometric HA, α -TCP, TTCP and CaO.

Raman spectrometry was used on the synthesized powders to study the change in PO_4^{3-} groups, and in other functional groups such as OH^- , HPO_4^{2-} and CO_3^{2-} . The characterization was carried out at room temperature. The typical Raman spectra of synthesized powders were shown in Figure 5.3. The vibrational spectra of the synthesized HA powders exhibited a strong molecular character associated with the internal modes of PO_4^{3-} tetrahedra.

For phosphate group in apatite, there were four different frequencies: the peaks that appeared around $430\text{-}450\text{ cm}^{-1}$ were attributed to the symmetric O-P-O bending mode (ν_1); The peaks at about $580\text{-}630\text{ cm}^{-1}$ were components of the asymmetric O-P-O bending mode (ν_4); The very strong peak at around 960 cm^{-1} was assigned to the non-degenerate symmetric P-O stretching mode (ν_1); and the forth component of the ν_3 band was observed at around 1050 cm^{-1} . The hydroxyl stretch was observed at 3573 cm^{-1} in the spectrum of HA feedstock, whereas no obvious hydroxyl stretches were detected in the plasma spheroidized powders. This finding indicated the dehydroxylation of the HA structure during the high temperature processing.

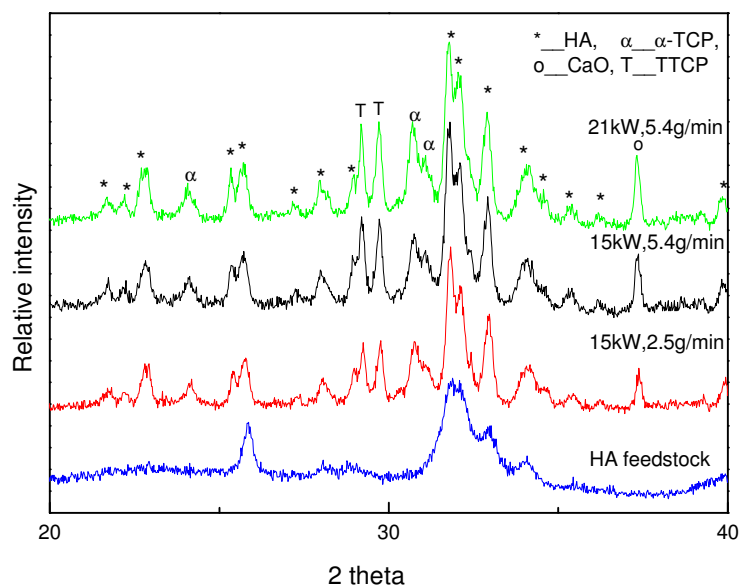


Figure 5.2 XRD results of spray dried HA powders and spheroidized HA powders

As shown in Figure 5.3, HA feedstock had a single peak attributed to the symmetric stretching mode for phosphate at 962 cm^{-1} . Vibration changes of ν_1 were observed after plasma processing. New shoulders appeared at 940 , 947 , 953 and 969 cm^{-1} . The loss of the symmetric stretching mode at ν_1 position indicated that the environment around phosphate ions had changed after plasma processing. The Raman spectra confirmed the presence of TTCP (doublet at 940 and 947 cm^{-1}) and TCP (947 and 969 cm^{-1}) according to Cleries et al [6]. The peak centered at 953 cm^{-1} might be attributed to the amorphous calcium phosphate phase in the synthesized powders. The peaks around 1350 cm^{-1} were attributed to the ν_3 vibrational mode of carbonate ion. The occupancy of ν_3 carbonate vibration modes might come from the competition between the phosphate and carbonate ions. The presence of carbonate vibration would contribute to the decrease of hydroxyl mode in Raman spectra of spheroidized powders. No peak belong to HPO_4^{2-} (locating near to 875 cm^{-1}) was traced in the

powder samples. The detection of amorphous phase and carbonate ions group indicated that Raman spectrometry could be used as a complementary tool to analyze the minute phases in samples.

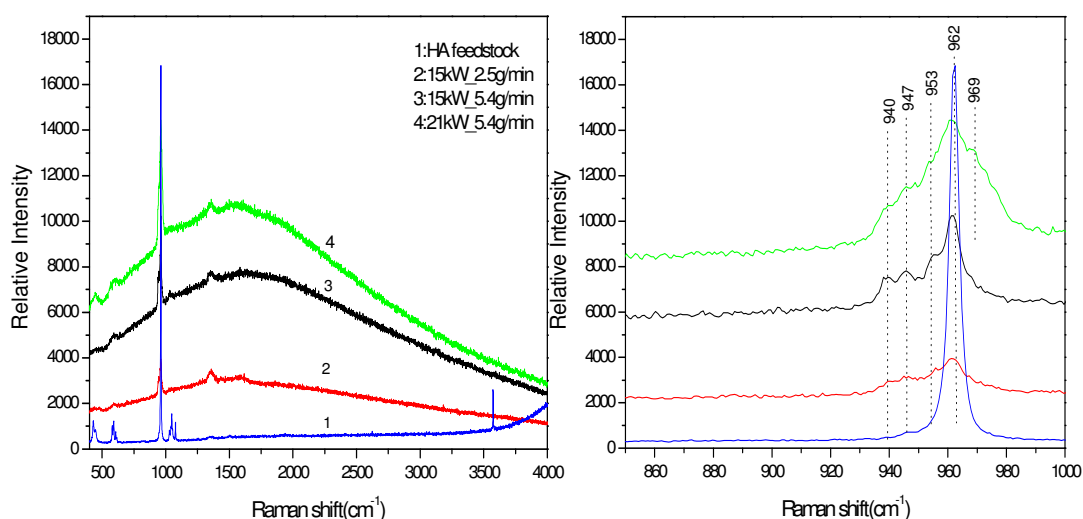


Figure 5.3 Raman spectra of spheroidized HA powders obtained at various working conditions.

5.2.1.3 Heat-treatment effect

For calcium phosphates, the excellent biocompatibility could only be retained when pure and highly crystalline HA was obtained. A heat treatment at around 800~900 °C could help to recover the high crystalline HA without causing any consequent decomposition. Thus, these synthesized powders were heat-treated at 850 °C for 1.5 hr in the air with furnace cooling. The heating rate was set at 5 °C/min and the cooling rate was set at 10 °C/min, respectively. After the calcinations, the powders were analyzed by different characterization methods.

A typical XRD pattern of heat treated powders was shown in Figure 5.4. It was found that the main peaks of HA in the heat treated powders became sharper and more prominent. The peak of CaO was almost unchanged. There was an absence of TTCP

and α -TCP, with β -TCP instead, which indicated that TTCP had transformed back into crystalline HA structure due to the similar chemical structure, and α -TCP turned into β -TCP after heat treatment.

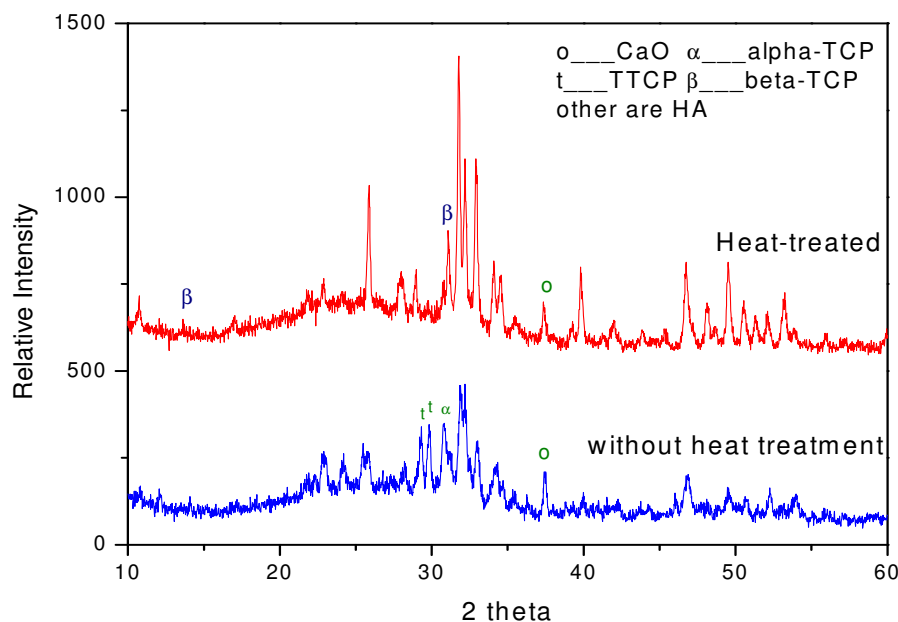


Figure 5.4 XRD results of RF plasma processed powders (20kW, 10rpm) with and without heat treatment at 850 °C for 1.5hr.

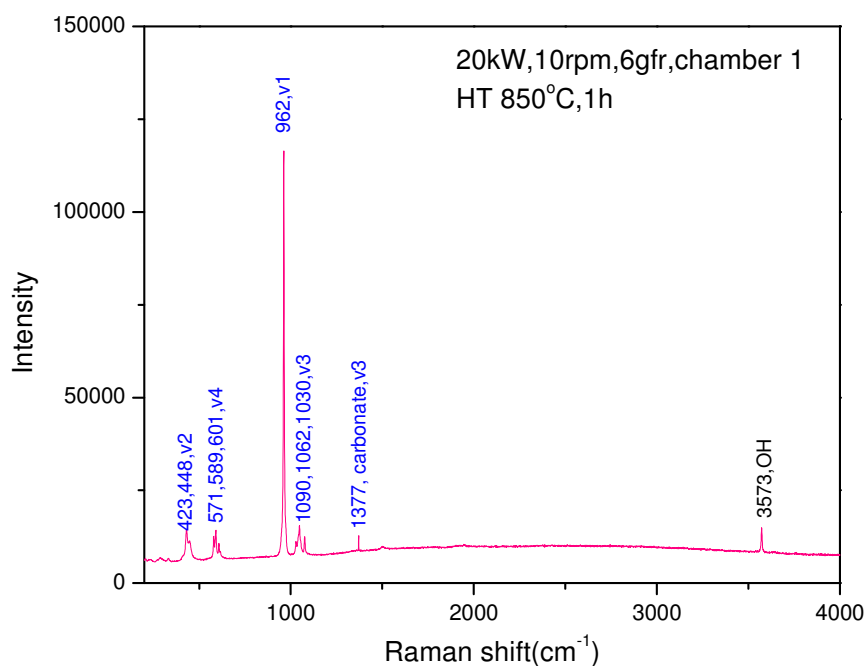
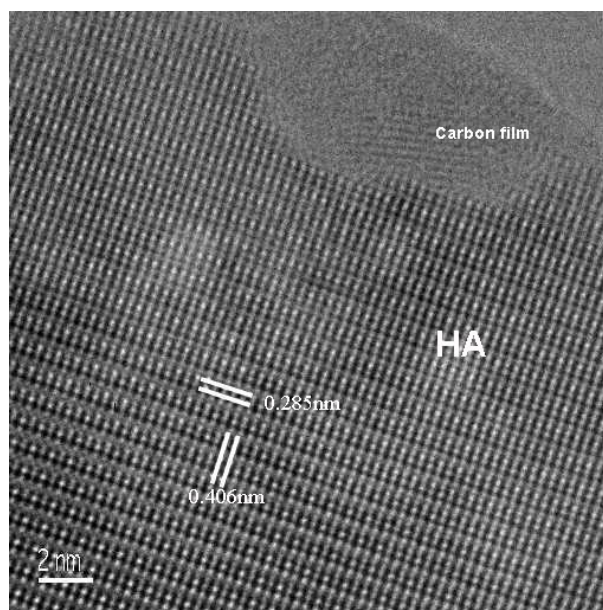


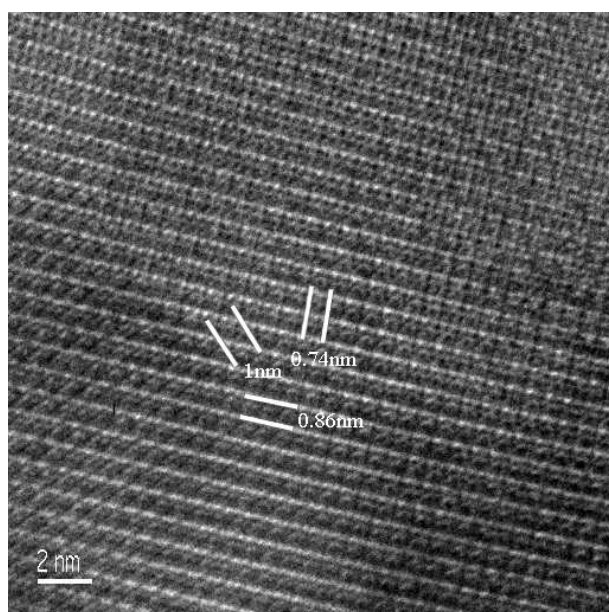
Figure 5.5 Raman spectrum of the heat treated RF plasma synthesized CaP powder which obtained at 20kW, 10 rpm.

The Raman spectrum of the heat treated powder was shown in Figure 5.5, the vibration modes for PO_4^{3-} exhibited much stronger than those observed in the powders without heat treatment. The peaks located at ν_2 , ν_4 , and ν_3 positions had splitted into several small peaks. The predominant intensities of phosphate vibrations and peaks splits indicated the increase of the powders crystallinity after the heat-treatment. The competence from the hydroxyl vibration indicated the recovery of water into the dehydrated apatite structure.

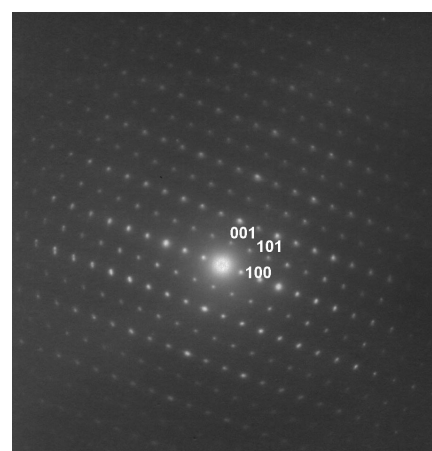
In addition to XRD and Raman spectrometer analysis, HR TEM was also used as a complementary method to view the detailed structure information of the heat treated powders. As shown in Figure 5.6 (a-b), well distributed lattice information was detected in heat treated RF plasma processed powders. From diffraction pattern shown in Figure 5.6 (c), the atoms in the HT powders highly arranged together. The inter-reticular distances of the nearest atoms and angles ϕ between (hkl) planes were measured from these HR TEM views. In the case of Figure 5.6 (a), the distances between the adjacent atoms were $d_1=4.06 \text{ \AA}$, $d_2=2.85 \text{ \AA}$, $\phi=90^\circ$. These two d values corresponded to the d -values of (200) and (211) planes of HA, respectively. These two planes were viewed along $[0\bar{2}2]$. In the case of Figure 5.6 (b), the lattice spacing measured was $d_1=7.4 \text{ \AA}$, $d_2=8.6 \text{ \AA}$, and $d_3=10 \text{ \AA}$. Since this technique usually contained an error of about 3%, the d_1 and d_2 could be corresponding to the d value of (001) and (100) planes of HA, respectively. The d_3 corresponded to the 'a' value of HA. Then it could be ascertained that HA dominated in the heat treated RF plasma processed powders.



(a)



(b)



(c)

Figure 5.6 HRTEM views of RF plasma synthesized powders after heat treatment at 850 °C for 1.5 hrs.

5.2.2 Discussion

5.2.2.1 RF plasma processing

As discussed by Boulos et al [84], the material transformations involved in plasma spheroidizing technique were mostly limited to physical changes involving melting and rapid solidification, vaporization and condensation. When the feedstock centrally entered the RF plasma flame, the injected particles were heated rapidly. The surface began to melt and partially evaporated due to the high plasma temperature. Thus, the HA feedstock experienced melting and evaporation within the plasma plume. After passing through the high temperature region, the melting part would rapidly solidify into spheroidized particles due to the surface-tension effect. The vaporized parts later condensed, upon reaching the end of the plasma, into fine particles as shown in Figure 5.1. The occurrence of such a phenomenon was actually confirmed by the appearance of bimodal size distribution in the HA powders produced by RF plasma in the previous work [94]. As shown in Figure 5.1(c), the ultrafine particles joined to other fine particles by one or two necks, which indicated that the fine particles had time for only one or two collisions at or above the fusion temperature before quenching was effective.

Hollow-structured particles were also detected in the RF plasma processed powders. One possibility of the formation of hollow structure could be explained as follows. During the RF plasma process, the surface temperature of the feedstock quickly reached the melting temperature, and the surface began to melt to form a shell. Then some of the remained absorbed moisture in the feedstock began to evaporate for the heat transfer, the internal pressure would be built up in the feedstock by the moisture. At the beginning of heating, the gas could escape through the developing molten shell.

After having reached a certain thickness, the melting front pushed the small bubbles toward the center due to the high surface tension of the molten material. If the bubbles got engulfed, their motion in the molten shell became sluggish in the strongly viscous liquid phase. If the internal pressure was high enough, the gas could be released or break through the surface before freezing of the molten shell.

Figure 5.7 presented the strongly porous structure of the product particles. If the melted surface formed a non-porous shell and the internal pressure was insufficient to release the gas out of the shell, particle with closed porosity would be formed. In the case of solid spheres, few moisture or gas apparently existed in the feedstock. The heat transferred into the interior of the feedstock rapidly, and it became the controlling process. This process would lead to the formation of solid spheres.

Klima and Kotalik [131] proposed another possibility. It was said that a melted spherical particle would begin to solidify on cooling and a solid layer grew at the entire particle surface. Since the density of the solid phase was higher than that of the liquid, porosity would form inside the sphere during further solidification.

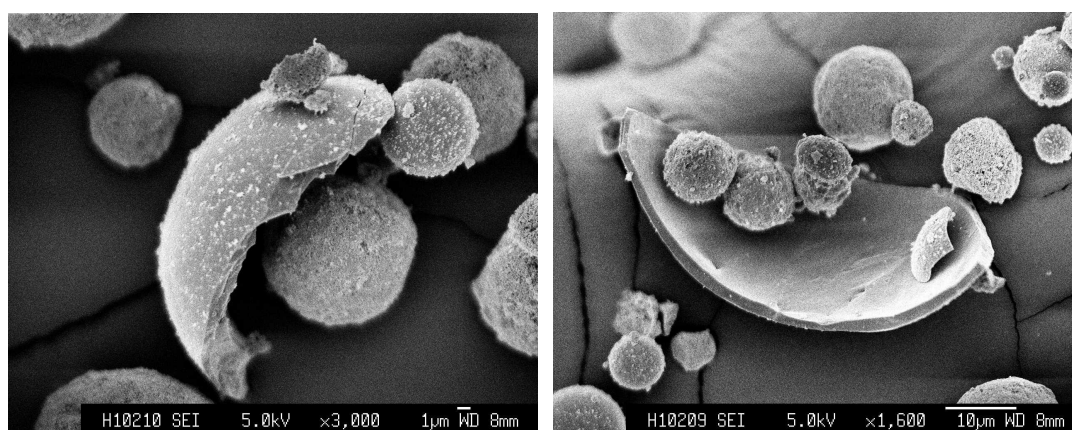


Figure 5.7 SEM images of broken particles after RF plasma processing.

As proposed by by Pradvic and Gani [132], the gases entrapped in the porous HA feedstock might contribute to the formation of hollow structured particles. The gases grouped together so as to reduce its surface tension. Their investigations have been carried out to determine the conditions that led to the production of spherical hollow ceramic oxide particles during melting in a DC plasma jet. They reported that the relative size of the pore was dependent on particle diameter. The major controlling factor that influenced this dependence was the escape of gas trapped in the spray dried agglomerate during melting. Surface tension or under cooling were shown to produce only minor effects. In addition, their results also showed that the nature of porosity within the hollow particles as well as the surface morphology was dependent on the material being sprayed.

As shown in Figure 5.1 (c), once the particle was melted in the jet all the gases would tend to group themselves to minimize surface area. The pores located near to the particle surface would most probably escape as shown in Figure 5.1 (b) whereas those situated into the core of the particles would be trapped in the particle contributing to the formation of the void as shown in Figure 5.1.(e).

The particle size distribution of the obtained powders was clearly exhibited in curve by a laser diffraction method as shown in Figure 5.1 (f). Because of the lower detection limit of the laser diffraction method was about 0.3 μm , it was then impossible to determine precisely the percent of finer particles in the spheroidized HA powders. From the two peaks of size distribution graph, it could be concluded that about 90.5 vol % of the powders in the range of 3-30 μm , which were the primary particles, and about 9.5 vol % of the powders fell in the range of 0.3-3 μm . It was found that the finer were below 5 μm , and the bigger particles had a mean diameter

about 11.7 μm . Particle size analysis results of the synthesized powders was presented in Table 5.1. The synthesized powder obtained at the working plate power level of 15 kW had larger values of $d_{0.1}$, $d_{0.5}$, and $d_{0.9}$ than those of the powders prepared at 21 kW.

Table 5.1 Particle size distribution of RF plasma synthesized CaP powders ($d_{0.1}$, $d_{0.5}$, $d_{0.9}$ refer to the measured particle size of 10 vol %, 50 vol % and 90 vol% of the powder particles)

Working conditions	$d_{0.1}(\mu\text{m})$	$d_{0.5}(\mu\text{m})$	$d_{0.9}(\mu\text{m})$
15kW_2.5g/min	5.1	13.4	24.2
15kW_5.4g/min	4.3	12.1	23.3
21kW_5.4g/min	4.1	11.5	22.0

Table 5.2 presented the mean particle sizes and BET results of the specific surface areas of the spheroidized powders obtained at various working conditions. It was found that the level of RF plasma power level had a significant influence on the specific particle sizes and surface areas of the obtained powders. As explained above, the injected particle surfaces would partially evaporate due to the high RF plasma temperature. When the working plate power level was increased from 15 kW to 21 kW, the RF plasma volume would become large, and the temperature increased continuously. These resulted in more evaporation of particles. Therefore, the synthesized particle diameters successfully decreased. In this study, the mean particle size of the spheroidized HA powders was decreased from 13.02 μm obtained at 15 kW to 11.68 μm obtained at 21 kW, and the specific surface area at 15 kW was approximately 3.195~4.71 m^2/g , and was increased for 21 kW to 6.83 m^2/g .

It was expected that an increase in powder feed rate would reduce the dwell time of the HA feedstock in the plasma flame, and thus would result in the relatively large

particle size. Yet, it was found that the particle size decreased with an increase powder feed rate. This because: the relatively low powder feed rate not only led to relatively long resident time, but also promoted some of the particles sinter together to form large particles.

Table 5.2 Specific surface areas of the RF Plasma spheroidized CaP powders.

Samples	Surface areas(m^2/g)	Mean Particle size (μm)
15kW_2.5g/min	3.1948	13.02
15kW_5.4g/min	4.7066	12.38
21kW_5.4g/min	6.8311	11.68

5.2.2.2 Phases and structure analysis

After RF plasma spraying, chemical transformation involved due to the high plasma temperature in the process. Vaporization of powders injected into the plasma could produce preferential removal. When HA feedstock in the plasma flame where the temperature was high enough to melt the surface or even the whole particles, low melting point component or group, such as OH^- or H^+ was removed preferentially, which in return resulted in the formation of TCP and/or TTCP (shown in Figure 5.2). At even higher temperatures, in addition to being hydroxyl deficient, the outer shell of the molten particles may become phosphate deficient (P_2O_5), and then calcium oxide (CaO) would be observed due to loss of P_2O_5 . Amorphous phase was also formed due to the rapid cooling rate.

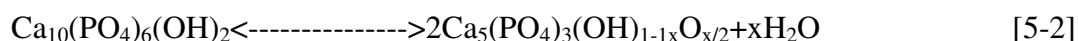
Thermal behavior of HA should be considered during the plasma spraying. Two ranges of temperature could be distinguished: the first, 0-1000 $^\circ\text{C}$, was the domain of intra-crystalline reactions and of irreversible decomposition of non-stoichiometric apatites. The second, over 1000 $^\circ\text{C}$, corresponded to reversible decomposition of

stoichiometric HA. However, at above 850 °C, in an atmosphere free of water, it was quite impossible to obtain stoichiometric HA because of the decomposition of the hydroxide ions:



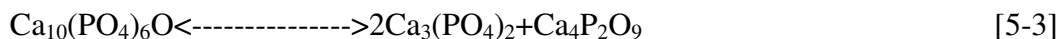
which led to the formation of an oxyhydroxyapatite ($\text{Ca}_{10}(\text{PO}_4)_6(\text{OH})_{2-2x}\text{O}_x$).

The amount of O^{2-} ions formed, of course, depended largely on the temperature and water pressure. This reaction was reversible like all the reactions that occurred at high temperature if there was sufficient moisture:



The substitution of two OH^- ions by one O^{2-} ion would form oxyapatite ($\text{Ca}_{10}(\text{PO}_4)_6\text{O}$), whose structure was the same to that of HA but had a slight decrease of the unit cell “a” dimension and a slight increase of “c” dimension.

At temperature higher than 1200 °C, oxyapatite decomposed in two compounds: α -TCP and TTCP according to the reaction:



On heating at temperatures above 1570 °C, a liquid phase began to form and above 1700 °C, the only solid phase to subsist was CaO. These decomposition reactions explained why CaO and other high temperature calcium phosphate phases were found in the RF plasma processed powders.

TCP had three polymorphs, such as: β -TCP was stable below 1180 °C, α -TCP between 1180 and 1400 °C, and α' -TCP was above 1470 °C. Among the three

allotropic forms, β -TCP was preferred as a bioceramic on account of its chemical stability, mechanical strength, and proper bioresorption rate. The heat treatment accelerated the α -to- β transformation as shown in Figure 5.4.

The Rietveld method was used to treat the XRD patterns in order to determine quantitatively the amounts of crystalline phases in the spheroidized powders. Calculation based on the Rietveld method did not need calibration experiments since it approached the XRD patterns directly. Instead of standards, this method required the knowledge of different crystal structures of the phases present in XRD patterns. However, when amorphous content had to be determined, it was necessary to employ an internal standard material for reference purpose [133].

Without treating the amorphous phase, the XRD spectra of the spheroidized powders were refined by the Rietveld method to calculate the relative phase contents within the crystalline region. The pattern fitting was performed and satisfactory results were obtained. The results of weight percents were shown in Figure 5.8. Referring to the weight percent of HA, it could be seen that the powders experienced higher decomposition at working plate power level of 21 kW than that of 15 kW (with other working parameters kept constant). The enthalpy of plasma flame was the primary driving force for the decomposition of HA. As discussed in the former part, an increase in the working plate power added to the energy of the plasma, and in return generated a higher flame temperature, leading to an increase in the extent of decomposition of HA powders in the plasma flame. Thus, an increase in working plate power would result in the significant decomposition. Particle velocity could also have a substantial influence on the particle temperature history and its ability to reach its melting and vaporization temperatures [84]. With the increase of the powder feed rate

into the plasma, the energy transferred from the plasma to the particles would result in a corresponding drop in the particle temperature and consequently in the decomposition of particles. As discussed in [134], amorphous phase was dominantly presented in the nano particles, which would contribute to the decrease of decomposition with an increase in feed rate.

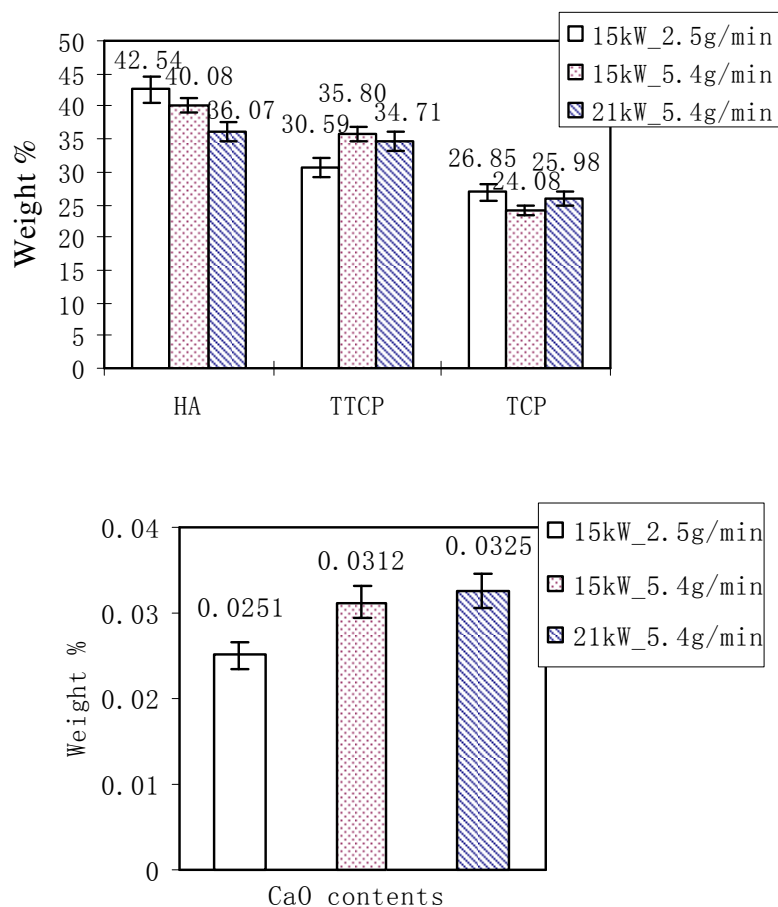


Figure 5.8 Phase contents in spheroidized HA powders obtained from various working conditions.

5.3 Characterization of RF plasma synthesized nano powders

Nano particles were partially separated to another collector that was designed to collect the RF plasma processed powders with very fine sizes. Their phases and microstructures were characterized by SEM, TEM, and XRD. Intensities from XRD traces were also used to calculate relative decomposition trends. Due to the presence of high amount of amorphous phase, an internal standard was employed to calculate the phase contents in the nano-sized powders. High purity (99.99 wt%) of Al_2O_3 was used as the internal standard reference sample. Thermal analysis was carried through DSC to determine the recrystallization phenomena of amorphous phases.

5.3.1 Results

5.3.1.1 Morphological analysis

The morphology of the nano-sized HA powders were observed using the JEOL JSM-5600 LV SEM and JEOL 2010 TEM. SEM samples were prepared by sprinkling the HA powders onto a small copper plate with a layer of double-sided carbon adhesive tape. The samples were then gold coated for 400 seconds using a Polaron SC7640 Coater. TEM samples were prepared through the procedures as described in Chapter 3. The magnification under the TEM had to be kept low as the nano-particles underwent excessive denaturing, which were probably due to excessive charge build up on the particle surface coupled with the high heat induced by the high energy density beam. Methods were currently being investigated to reduce beam damage in the TEM, such as, introducing a cold stage with liquid nitrogen, and leaving the sample overnight in the evacuated state in the TEM before resuming the next morning. Furthermore, it was noticed that the samples denatured faster when acetone was used in the sample preparation stage when compared with ethanol.

Figure 5.9 (a-c) showed the typical SEM morphologies of nano powders. The general trait for the nano powders was that they had agglomerated because of the size effect. The self-agglomerated powders were not very dense. There was an apparent lack of cohesion within the inter-agglomerates and intra-agglomerates. This result from SEM had shown that the RF plasma process could be used to produce nano-sized powders.

Figure 5.9 (d-e) showed the spherical morphology of these nano powders under TEM. The particle size of the nano powders was within the range of several nanometers to around 60 nm, which were corresponding to the results obtained from high magnification SEM analysis. The smallest particles in the agglomerated particles were smaller than 10 nm. The images obviously showed the network of agglomerated nano-sized spherical particles. Some of the nano particles had aggregated or bonded into one larger cluster during the condensation process.

On the basis of the morphology of the nano powders, it could be inferred that the formation of these particles were condensed from the evaporated part of the feedstock during the RF plasma processing.

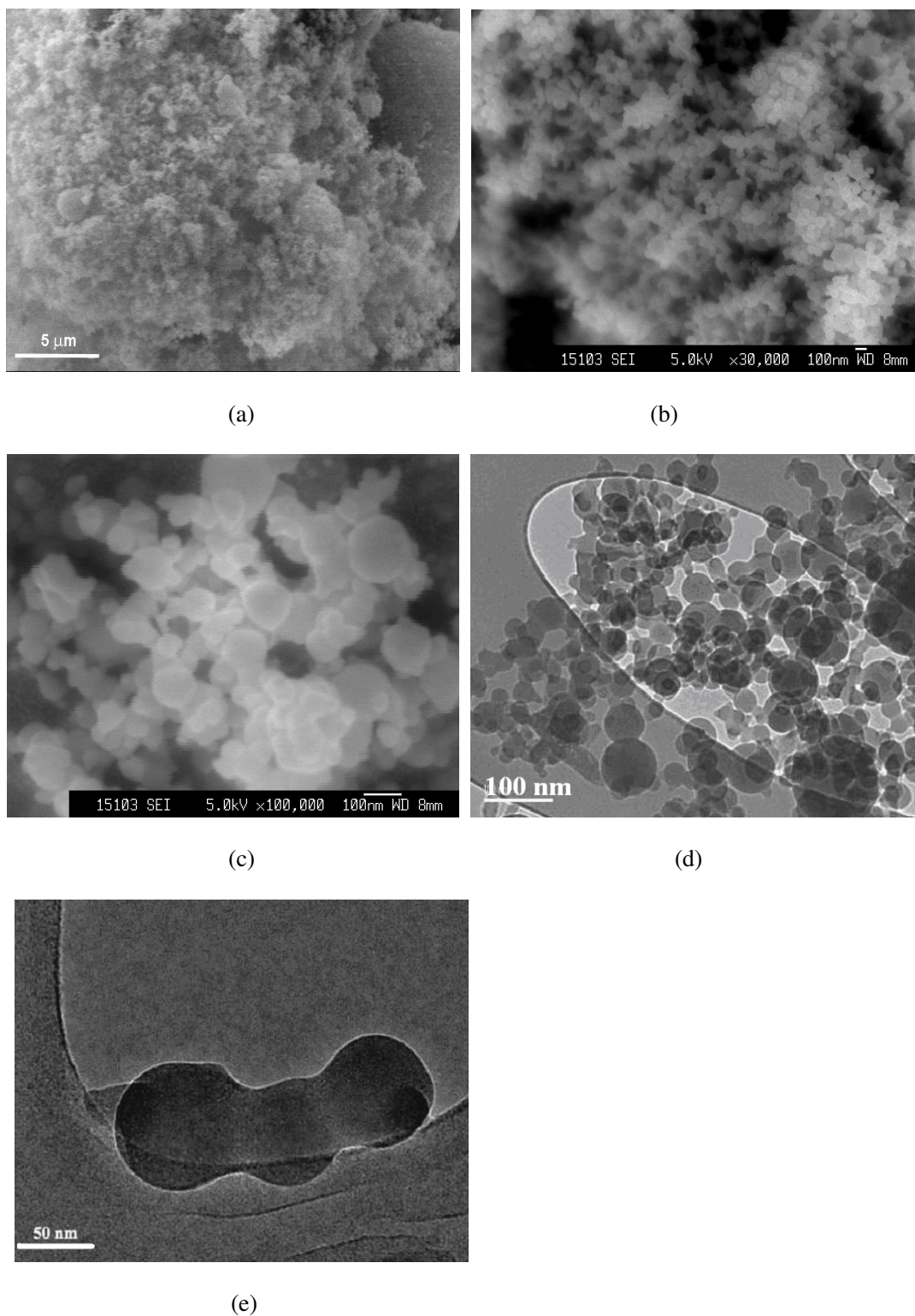


Figure 5.9 SEM images (a-c) and TEM images (d-e) of nano HA powders obtained from RF plasma thermal spraying.

5.3.1.2 XRD analysis

Phase composition of the nano HA powders were investigated using XRD analysis. Due to the low peak intensities caused by nano-crystalline nature of the materials, the powders were scanned at a low scan rate of $0.01\text{ }^{\circ}\text{s}^{-1}$ and per step for 2 s, under the operating conditions of 30 kV and 20 mA. The Joint Committee of Powder Diffraction files (JCPDS 9-432, 9-348 and 37-1497) were used to compare with XRD results for the identification of the different phases in the samples.

As observed from the XRD pattern (Figure 5.10), the peaks were relatively broad, and intensities were relatively low. The peak widening could be interpreted as a combined effect from the nanometer-sized precipitates and internal strains formed during crystallization. Normally, the peak broadening occurred when an individual crystallite became so small that the complete diffractive interference of an X-ray did not occur at angles close to the Bragg angle, which was because of the limited number of crystal planes. This peak broadening increased as the crystallite size decreased. In Figure 5.11, HA was preferentially dominated in the nano-sized powders. Apart from the HA phase, α -TCP and CaO were also found in the powders, which confirmed the decomposition of starting HA due to the high temperature of RF plasma flame. A broad hump centered at about $2\theta=29^{\circ}$ in the XRD pattern was attributed to an amorphous phase in the nano-sized powders.

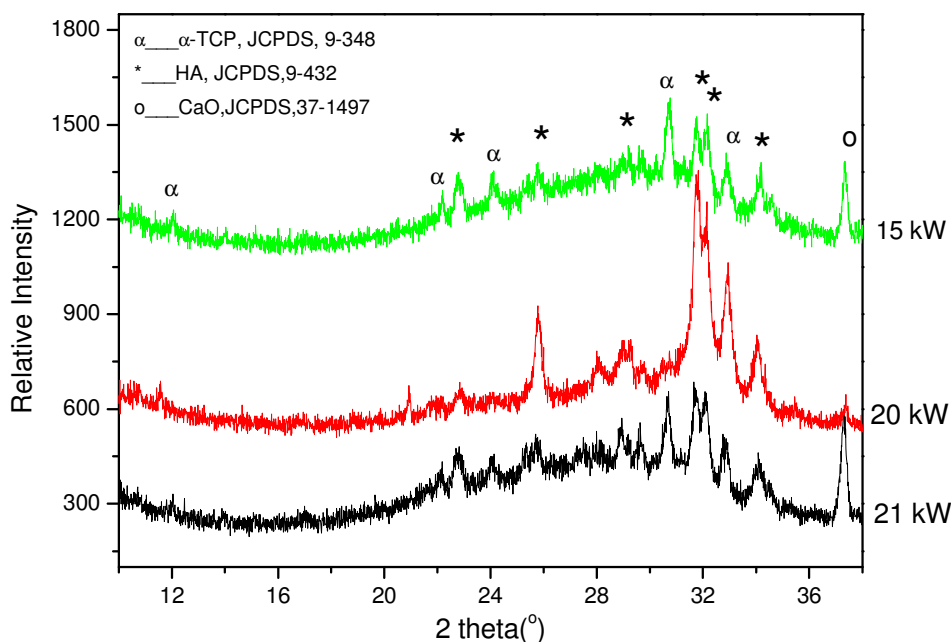


Figure 5.10 XRD patterns of nano-sized powders after RF plasma processing at various working plate power level.

Due to the lower melting point of amorphous phase than that of crystalline phase, the nano sized powders were heat-treated at 800 °C for 1.5 hr in air. Compared with the powders without heat treatment, relatively sharper peaks with higher intensity were observed in the XRD patterns, which showed the highly crystallized nature of the heat-treated powders. β -calcium pyrophosphate (β -DCP, or β -Ca₂P₂O₇) corresponding to JCPDS 9-346 was found in the nano powders (Figure 5.11). The peak belong to CaO was slightly traced at $2\theta=37.4^\circ$, while α -TCP phase was almost undetectable in the heat treated nano powders, probably owing to the overlapped peaks with those of HA or β -DCP. They might also have been converted into HA or β -DCP by the driving force of temperature.

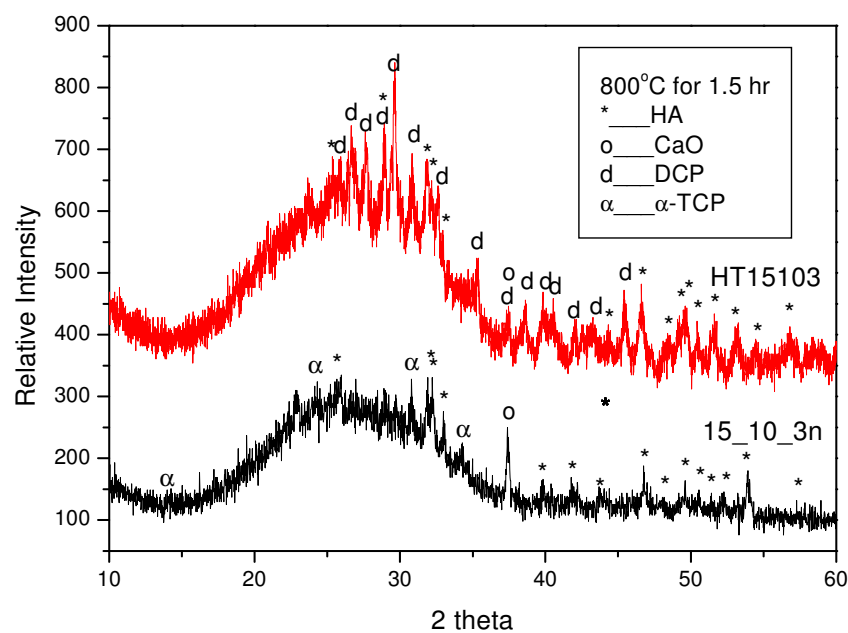
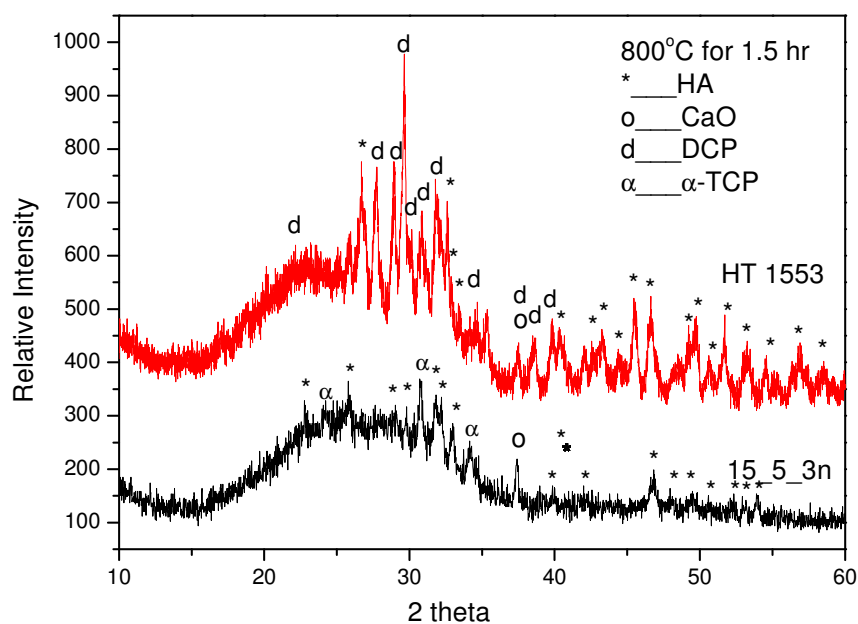


Figure 5.11 XRD results of nano powders after heat treatment at 800 °C for 1.5 hr in air.

5.3.1.3 HR TEM results

It was possible to identify the crystal structure at the molecular level using the HR TEM measurement. Direct observation under the HR TEM gave clear images of the morphologies and boundaries between the nanometer-sized crystallites, from which crystallite dimension in different crystallographic orientations may be accurately measured. HR TEM studies had been performed to gain information about the grain-boundary structure along apatite/amorphous junctions. During HR TEM nanometer-sized particle image simulation, it had been proven that the image formation process could be influenced by: (i) particle thickness inducing contrast variations and difference between images and real particles size; and (ii) contrast fringes running parallel to nanometer-sized particle surfaces [135, 136].

Figure 5.12 showed the typical structure after the nano powders, revealing the nucleated nano-crystalline domains within the powders. These domains were thought to have nucleated immediately after condensation during plasma spraying. As shown in Figure 5.13, it was found that the nano-sized particles contained amorphous and crystalline phases. The lattice spacing in the crystalline HA, shown in Figure 5.13, was about 3.85 Å along [111] direction.

Figure 5.14 (a) was another HRTEM image showing the morphology and boundary between the nano crystallites and the amorphous phase. The crystallites constituted a transition step between the amorphous matrix and the well-ordered crystals. The unit cells showed that the crystalline HA was formed from the amorphous region along c axis at high temperatures. The formation of a large amount of interfaces or transition region during the nano crystallization from amorphous solids had a significant influence on the transformation thermodynamics.

The lattice image shown in Figure 5.15 (a) revealed that several lattice layers were distorted to finger mark shape near the amorphous region. This phenomenon may correspond to the existence of strains in the amorphous phase region. These strains resulted from the rapid cooling from the high temperature plasma.

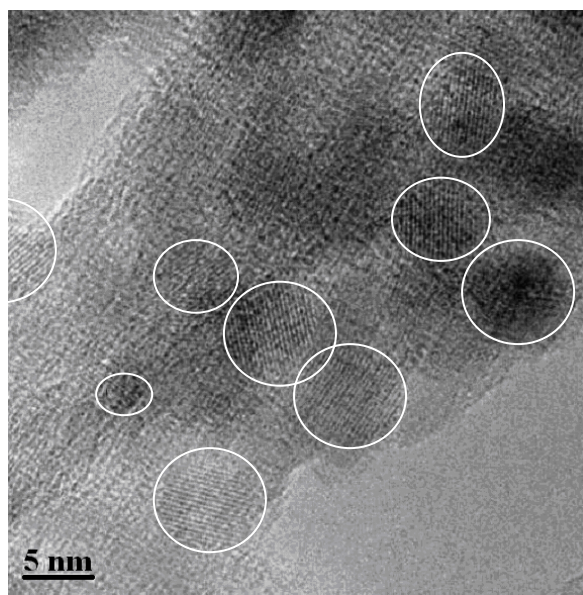


Figure 5.12 Nano domains within the nano sized powders after RF plasma processing.

Scale bar was 5 nm

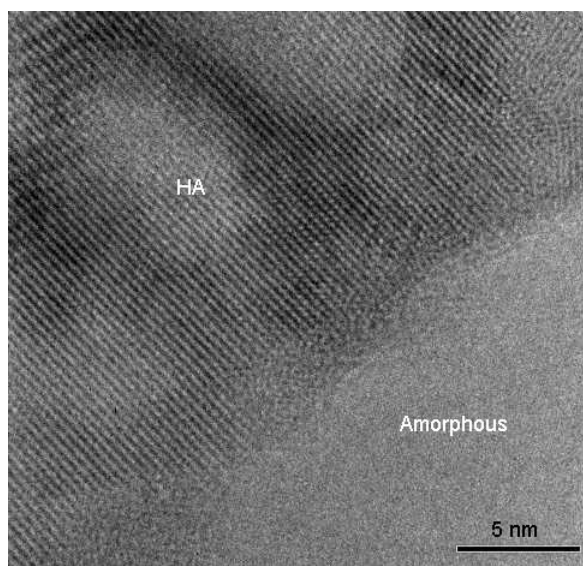


Figure 5.13 An HRTEM image showing amorphous/HA phases interfaces in nano HA powders along [111] direction.

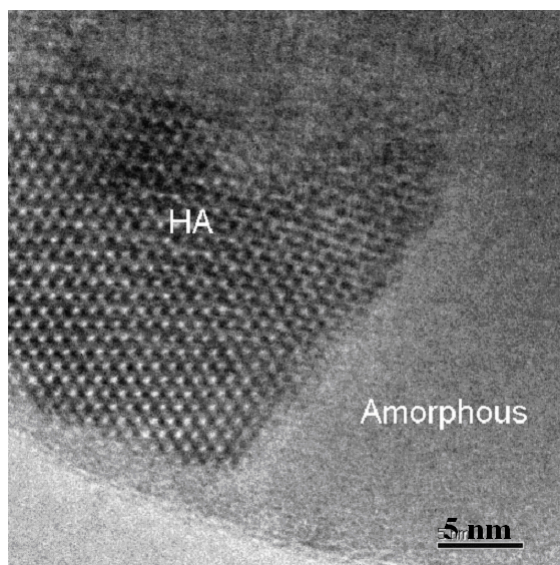
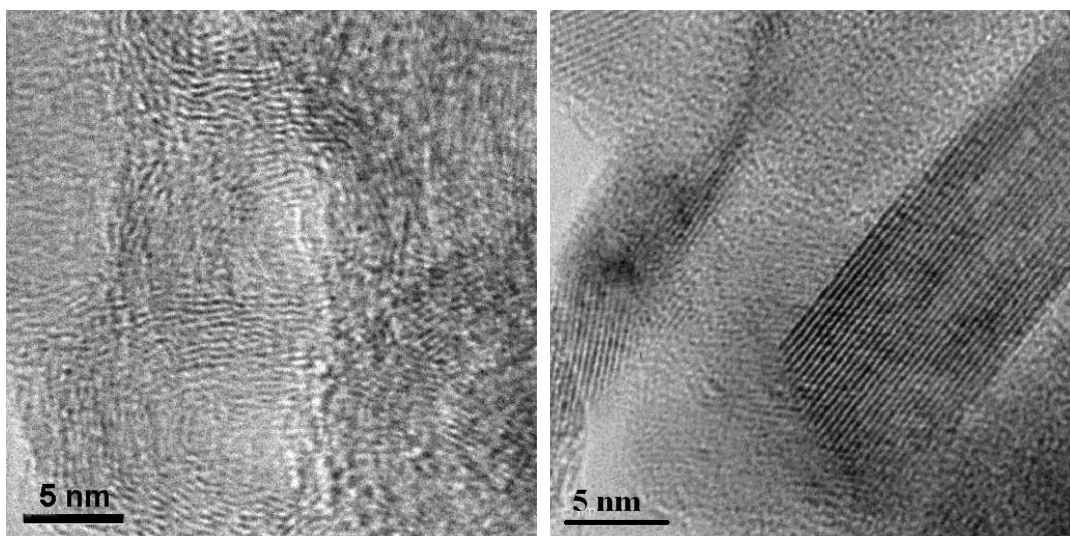


Figure 5.14 HA/amorphous interfaces in nano powders showing the unit cells of HA along c.



(a)

(b)

Figure 5.15 HRTEM images: (a) Distorted lattices;
(b) Orientated lattices taken in the nano sized powders. The scale bar was 5 nm.

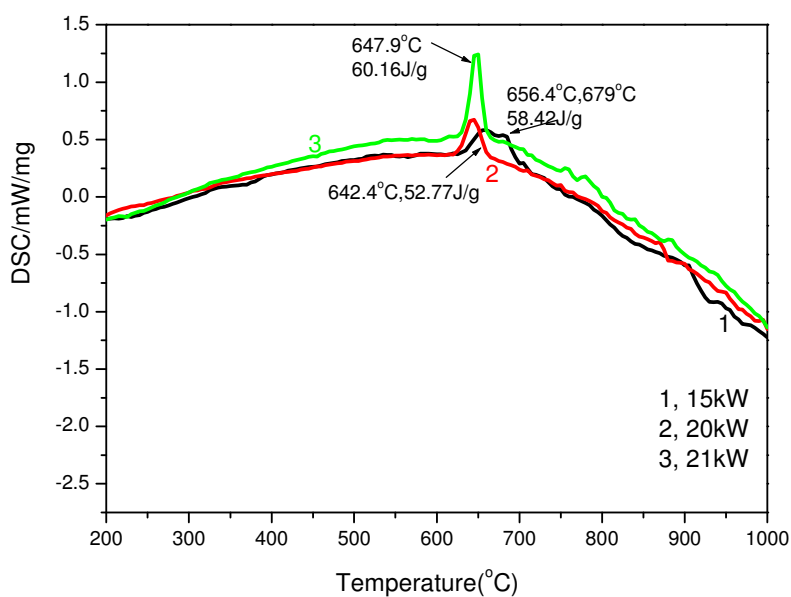
5.3.1.4 Thermal analysis

As the presence of amorphous phase in the synthesized nano powders, calorimetric measurements were performed using DSC to study the transition temperature between amorphous and crystalline phases. Figure 5.16 (a) showed the DSC results of nano-sized powders obtained at various working plate power levels. The result of spray dried HA feedstock was presented in Figure 5.16 (b) as reference information.

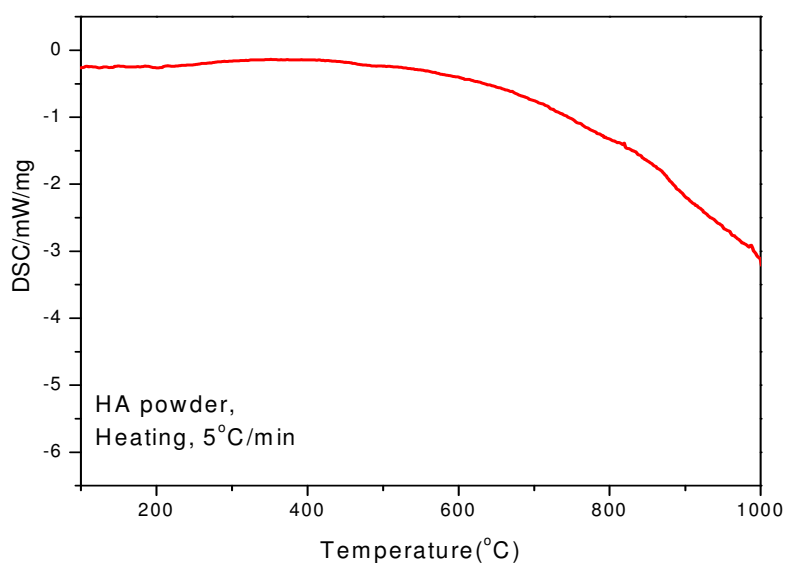
A slow exothermic tendency prevails from 200 °C to 640 °C in the powders, and this was partially attributed to the difference in heat capacity between the amorphous phases when compared with Al₂O₃ pan [137].

As observed, all apparent peaks of the nano sized powders lied on an exothermic rise. These peaks represented the crystallization of the amorphous calcium phosphate into crystalline calcium phosphates. For the powders obtained from the working power level of 15 kW, two exothermic peaks were positioned at about 656.4 °C and 679 °C, respectively. For the powders obtained at working power of 20 kW and 21 kW, the peaks were positioned at 642.4 °C and 647.9 °C, respectively. No obvious exothermic peak or endothermic peak was observed from the curve of spray dried HA.

As shown in Figure 5.16 (a), the magnitudes of the peaks were different under various powders formation parameters, which might have a linear relationship with the contents of amorphous phase. Through the determination of the area under the exothermic peak, the enthalpies of the phase changes could be ascertained. The calculated recrystallization energies of the nano-sized HA powders prepared at 15, 20 and 21 kW were 58.42 J/g, 52.77 J/g and 60.16 J/g, respectively.



(a)



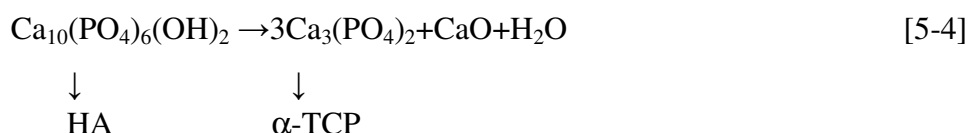
(b)

Figure 5.16 DSC results: (a) nano-sized powders obtained at various working plate power levels, and the curve at 15kw shows two overlapped exothermic peaks; (b) spray dried HA feedstock.

5.3.2 Discussion

5.3.2.1 XRD analysis

The formation of various phases in nano-sized powders was the main result of extremely high temperature and highly reactive atmospheres, which favored non-equilibrium or metastable structures [138]. The decomposition of the evaporated feedstock during the RF plasma processing could be described as follows:



Where α -TCP and CaO were the high temperature meta-stable phases. This was not uncommon particularly with non-equilibrium processes like thermal spraying.

The amorphous phase was formed due to the rapid solidification on high cooling rate, at about 10^4 K/s during RF plasma processing. Amorphous calcium phosphate played an important role in the formation of biominerals and was used in several bioactive biomaterials. Such amorphous phase that existed in the as-synthesized powders could be effectively transformed into the crystalline phase through a post-spray heat treatment [139]. There has been considerable attention on amorphous calcium phosphate, which has the highest resorbability among Ca/P compounds. The availability of large quantities in the powder form could be beneficial as it could be used as viable carrier for genes and drugs. However, the consequences were also more severe and less tolerable in biomedical application, where such additional phases could induce unfavorable tissue response.

Referring to the XRD results (the main peak intensity of CaO) in Figure 5.11, it

could be seen that the nano powders experienced significant decomposition at working plate power of 15 kW and 21 kW, respectively (with other working parameters kept constant), whereas there was no significant decomposition at 20 kW.

As discussed previously, the plasma temperature and dwell time of particles greatly influenced the decomposition of starting HA. An increase in the working plate power added to the energy of the plasma, and in return generated a higher flame temperature, leading to an increase in the extent of decomposition of HA powders. While, it was important to emphasize that the plasma power level was related to the particle velocity. An increase in working plate power would also increase the plasma velocity, which in return would increase particle velocity [129]. An increase in the particle velocity would decrease the dwell time of HA feedstock in the flame, and as a result, the decomposition of the HA powders would decrease.

As the above analysis demonstrated, at a higher working plate power of 21 kW, significant decomposition of HA was obtained predominantly due to the relatively high energy of RF plasma flame. However, a lower working plate power of 15 kW also caused significant decomposition, which was mainly attributed to the increased resident time of powders due to the low plasma velocity. Slight decomposition was achieved at a power level of 20 kW due to a combined influence of flame temperature and plasma velocity.

In addition, the increase in working plate power level from 15 kW to 20 kW just needed the adjustment of working plate current levels proportionally. However, the increase from 20 kW to the maximum working plate power level of 21 kW needed not only an electrical enhancement but also the adjustment of the grid gauge to make sure the pointers of the voltage gauge relatively parallel to the pointer of the grid gauge.

This meant that the increase in current and voltage could not increase proportionally. This kind of difference in the adjustment of working plate power level might also result in the difference in the state of the feeding powder in the plasma flame with an increase in the working plate power level from 20 kW to 21 kW.

5.3.2.2 Phases contents

The crystallinity of the nano HA powders and crystalline phase compositions depended on the thermal spray processing parameters. They were believed to be a key factor affecting the biological response to the surrounding tissues [140]. To determine the phase composition and the amorphous fraction generally presenting in the various nano HA powders, several methods have been described. In the present study, Rietveld analysis was used to calculate the phase composition in the nano powders.

Rietveld method required the knowledge of the various crystal structures of the phases present in the XRD patterns. However, when amorphous content had to be determined, it was necessary to employ an internal or external standard material for reference purpose. In this study, the amorphous content was indirectly calculated using crystalline alumina (99.99% pure) as an internal standard. A mixture of 50 wt% alumina and 50 wt% of the plasma-synthesized nano powders were mixed together and used for the quantitative analysis. Rietveld analysis of the XRD of the crystalline alumina standard mixed with the nano powders containing amorphous phase would yield a higher quantity of alumina than used in the mixture. This was because the XRD patterns were generated for the crystalline portion of the powders. The amorphous phase was transparent to the analytical treatment. Since the quantification was normalized to 100% the program reports alumina values higher than the amount added, the difference could then be used to calculate the amorphous content.

The formula was as follows:

$$\text{Amorphous (wt \%)} = 1 - (x/y) \cdot 2 \cdot 100\%, \quad [5-5]$$

Where, x was the amount of alumina added to the mixture (i.e. 50 wt %) and y was the value calculated by software.

Rietveld analysis was carried out with the “Rietquan 2.3” Quantitative Phase Analysis (QPA) software to determine the quantity of phases presenting after spraying. The raw data from the XRD scans were input into the analysis software for refinement purposes. Crystal models of HA, α and β -TCP, TTCP, CaO and Al_2O_3 were prepared for a starting model for the refinement from relevant crystallographic data. Peak shapes were modeled using the pseudo-Voigt function. Two asymmetry parameters were refined. In each case, four background parameters, a scale factor, five peak shape parameters, 2θ offset (zero point correction), sample displacement and cell parameters were refined. The occupancy of the hydroxyl (OH^-) ion was refined as one group (i.e. OH^- occupancy) using the same reasoning as Knowles et al [141]. The background "hump" of amorphous CaP at around $2\theta=29^\circ$ was modeled and refined using a separate Gaussian peak shape function and refinements were carried out till convergence.

After Rietveld analysis, pattern fitting was performed. The results were obtained as shown in Figure 5.18. The fitting statistics (Figure 5.17 (a)) gave R_{wp} and R_{exp} average values of 6.87 % and 5.54 % with a GOF of 1.26. The numerator of R_{wp} was the residual being minimized. R_{exp} gave the value of the weighted square of the difference between the observed and the estimated model. These values not only reflected a good fit of the experimental and refined data, but also confirmed the accuracy of the method. The other two pictures also showed the data at $2\theta = 20-70^\circ$ fit well, and

deviation from the calculated pattern was negligible.

Table 5.3 summarized the results obtained from Rietveld analysis of the nano powders. Figure 5.18 illustrated the relative contents of various phases in the nano powders. The results indicated that, as the plate power was increased, more amorphous material was produced with a concomitant decreased in the amount of other crystalline phases. It was found that there was more than 70 wt % of amorphous phase in the nano-sized powders. The starting feed material was made up of HA which underwent decomposition and vaporization to various extents during the plasma treatment depending on the thermal input. In general, as plate power was increased, the decomposition should increase. However, at high enough powers the heat input to the feed was so high that the levels of vaporization exceeded decomposition, and gave rise to more amorphous material. In this instance, the amount of decomposed phases did not increase, and in some cases were seen to decrease.

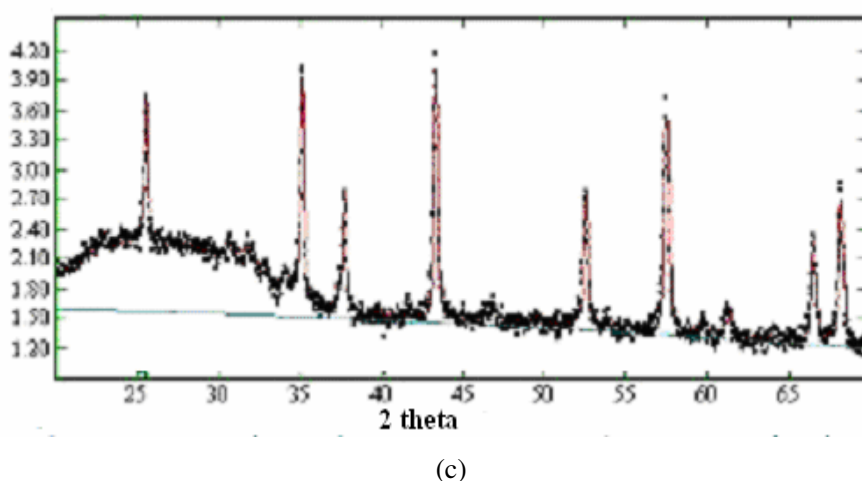


Figure 5.17 Fitting deviation of XRD pattern of 50 wt % nano powders mixture with 50 wt % alumina powders with Rietveld analysis.

Table 5.3 Quantification (wt %) of the phases and crystallinity for the nano powders.

Plate power /flow rate	Amorphous	HA	α -TCP	CaO	TTCP
15_5	66	13.1	14	2.7	4
21_5	76	7.5	15.3	1.4	0
21_10	75.4	7.6	15	2	0

The remaining phase was from the XRD samples' holder material.

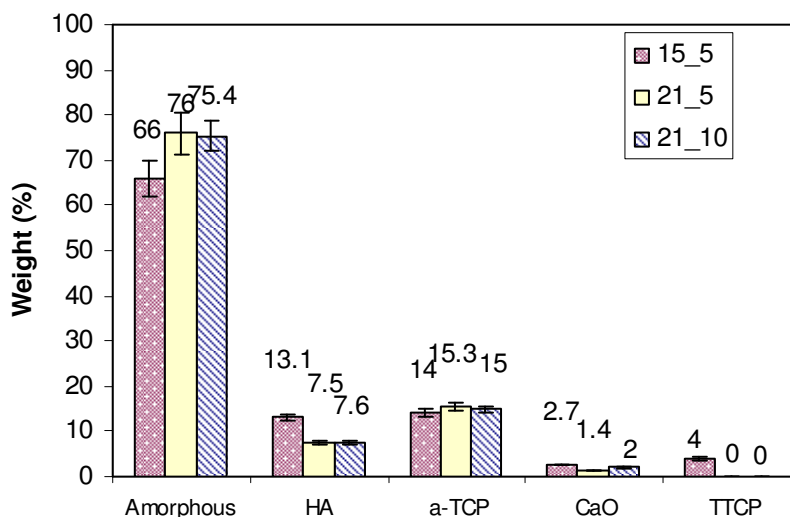


Figure 5.18 Phases contents in the nano sized powders. The results were averaged from three measurements.

5.3.2.3 HR TEM analysis

HR TEM examination revealed that the specimen consisted of well-crystallized HA crystals and amorphous phase, as shown in Figure 5.12. The presence of amorphous phase should be attributed to the rapid solidification rate during plasma processing. There were two hypothesis on the formation of crystalline HA phase. First, due to the fluctuation of RF plasma temperature, the liquid or evaporated particle undercooled to the nucleation temperature before solidification initiated [142]. Then during rapid solidification, the nucleation of the undercooled liquid grew to well-oriented nano crystals with grain boundaries. These grains could not nucleate near the melting point because there was insufficient driving force to overcome the solid-liquid surface

energy barrier. It also could not grow at low temperatures because there was insufficient thermal energy to drive atomic diffusion.

Another possibility was that some of the crystalline HA retained in the nano-sized powders due to the short duration of the feedstock in the plasma flame. From exactly the same orientation (Figure 5.14 (b)), which indicated epitaxial crystallization, it seemed more probable that the former was the main reason for the crystalline HA formation.

The crystalline domains were surrounded by the continuous amorphous regions. The amorphous calcium phosphate phase had high dissolution rate in the body fluids environment when compared with crystalline HA, which might influence the biomedical behavior for the implants. Relatively high dissolution of calcium phosphate might lead to high ions concentration of the environment and accelerate the deposition of new formed apatite layers. While, too fast dissolution of the implant would cause the inflammatory effect.

This amorphous phase could be mostly transformed into the crystalline phase through post-spray heat treatment [139]. After the heat treatment at 800 °C for 1 hr, some of the amorphous transformed into crystalline phase. As shown in Figure 5.19 (a-b), the general structure of the heat-treated nano particles was dominated by crystalline phase. Some amorphous phase was also detected in some local position as shown in Figure 5.19 (c-d).

Crystallization was a phase transformation process, in which an amorphous phase crystallized into one or more meta-stable crystalline phases. The driving force for the crystallization was the difference in Gibbs free energy between the amorphous and the crystalline states. The amorphous phase was in thermo-dynamical meta-stable state. It

would transform into more stable state under appropriate circumstances [143].

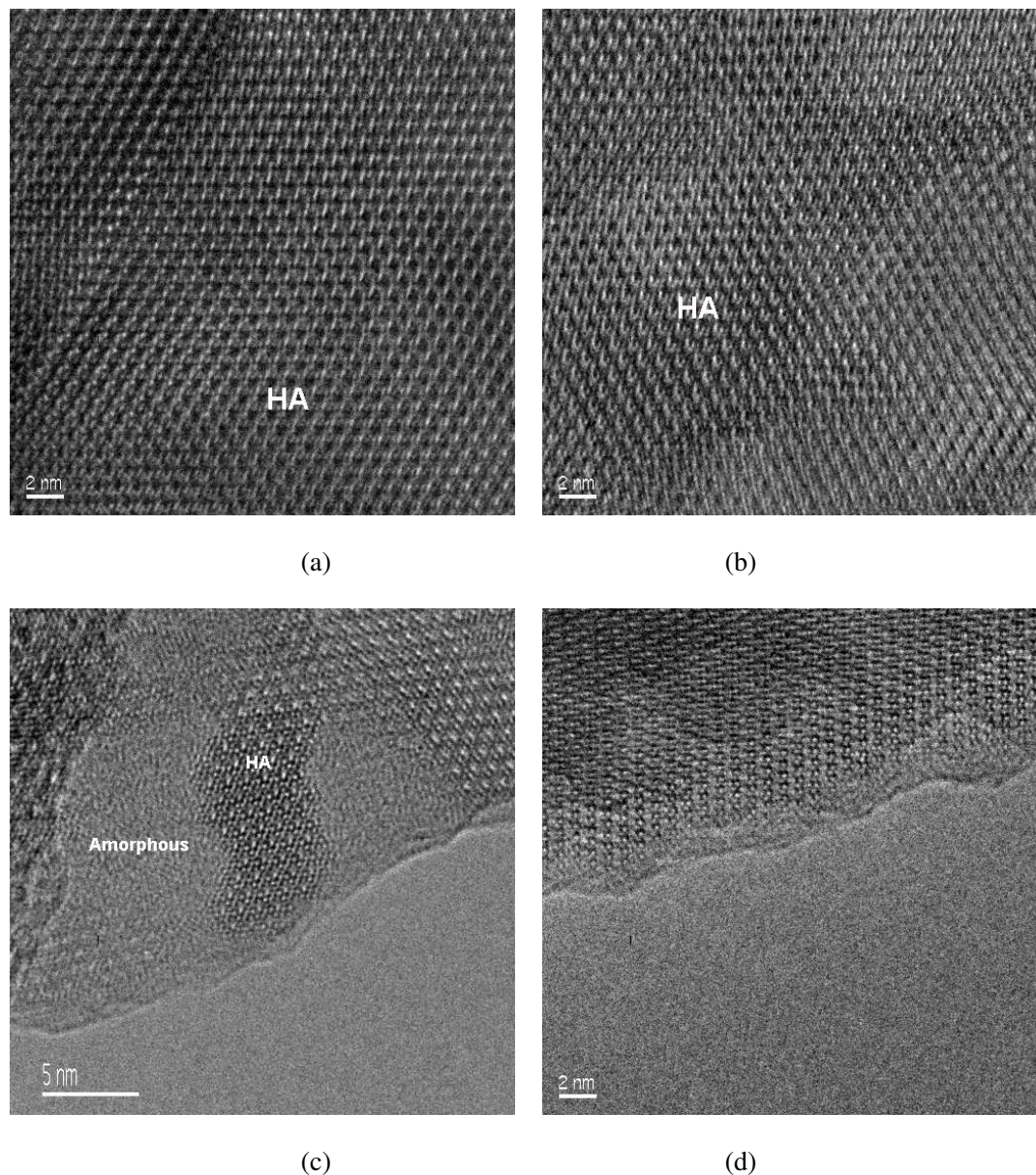
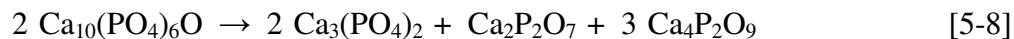
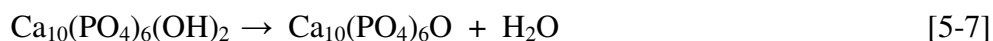


Figure 5.19 HRTEM images of nano powders (c-d), after heat treatment.

However, as shown in the XRD patterns in Figure 5.11, not only HA but also a new calcium phosphate phase (β -DCP) was observed in the heat-treated nano powders. This finding indicated that the amorphous phase did not only convert into HA phase but also β -DCP phase. It was reported that β -DCP had the ability to form a chemical bond directly with natural bone [144]. Also, it was reported that HA could be

decomposed into $\text{Ca}_2\text{P}_2\text{O}_7$ according to the following chemical reactions [82]:



From the presence of β -DCP after heat treatment, it was presumed that the decomposition of HA into DCP would occur through $\text{Ca}_{10}(\text{PO}_4)_6\text{O}$ or HA decomposed directly into DCP in the plasma flame [145]. For $\text{Ca}_4\text{P}_2\text{O}_9$ was not observed in the present result, hence it was logically concluded that HA has directly decomposed into DCP during the evaporation process in the plasma flame. Some amorphous phase may be expected to form from the $\text{Ca}_2\text{P}_2\text{O}_7$ region due to the rapid solidification. After heat treatment, this region would mainly crystallize into β -DCP in the nano powders. The amorphous region with efficient hydroxyl would crystallize into HA. Based on the previous literature, HA and β -DCP could be considered as stable in distilled water and thought to be stable and inert in solution. It was reported that the mechanical properties of sintered β -DCP was superior to sintered HA [146]. The most important fact of all was that the β -DCP has high bioactivity. In addition, β -DCP of bulk type did not produce the rapid sequence of membrane lysis or cell death, and was very stable *in vivo* [146].

5.3.2.4 Thermal analysis

As discussed previously, it was quite common to have amorphous phase due to the rapid cooling rate in the plasma processed powders or coating. The amorphous phase was sensitive to weak external and/or internal disturbing factors. There was no doubt that amorphous part of the structure played an important role for the future medical applications. The transition temperature from amorphous to crystalline phases was an

important parameter, which were the characteristics of a nucleation-and-growth process reflecting the properties of amorphous phase. Therefore, it was important to perform detailed study of this part of the plasma processed materials.

As shown in Figure 5.16, exothermic peaks were observed from DSC curves. The two exothermic peaks were partially overlapped in the nano powders obtained at 15 kW. The first peak at a lower temperature of 656.4 °C contributed to a crystallization of hydroxyl-rich amorphous regions. As subsequent crystallization occurs, the second peak at a higher temperature of 679 °C presented the diffusion of hydroxyl ions into hydroxyl-depleted regions. Gross et al [137] explained this phenomenon in transformation of amorphous phases in HA coatings. In plasma processing, the fast heating and high temperature attained in this process would cause hydroxyl removal. In return, it would induce different regions: one was a hydroxyl-rich region, and the other was hydroxyl-depleted or even oxy-rich region.

The shift of crystallization temperature might imply that the chemical state including structure would be strongly influenced by the working plate power. At working power level of 20 kW and 21 kW, the crystallization temperature began to rise. This suggested that the crystallization constraint by the increase in working power. That would result in the reduction of driving force for crystallization of the amorphous phase. In addition, it has been generally known that the crystallization was the kinetic process related to the diffusion of components. Thus, the increase in the melting energy of the amorphous phase would require an enhancement of the atomic mobility to compensate for this reduction of driving force component.

Different values of the enthalpy of phase transition for all powders were pointed out based on DSC measurements. It was expected that the enthalpy was positively related

to the magnitude of the amorphous phase. The higher the melting enthalpy, the more the amorphous phase. The amount of amorphous phase formed depended on the cooling rate, which may be modified by the temperature of the plasma flame. In other words, the amorphous phase in nano sized powders increased with an increase in working power. This correspondingly increased the enthalpy of the phase change.

5.4 Chapter summary

The spray dried HA powders were employed as feedstock for the radio frequency plasma processing. Both micron-sized and nano-sized spheroidized CaP powders were obtained with different chemical composition after RF plasma processing. The characterization results indicated that the plate power levels of RF plasma system influenced significantly the decomposition of HA into α -TCP, TTCP and CaO in the high temperature plasma flame. Amorphous phases were found to be dominant in the nano-sized CaP powders. The detrimental effects in the future medical application of these RF plasma synthesized powders should be taken into consideration. While, the bioactivities would also be enhanced by the decomposition of HA into secondary phases due to high solubilities of TCP, TTCP and amorphous calcium phosphate phase.

Chapter 6 Spark Plasma Sintering of RF Plasma Synthesized and Spray Dried Calcium Phosphate powders

Introduction

The poor mechanical properties (such as insufficient strength and durability in load-bearing conditions) of HA resembled the main limitation for performance in biological applications. High strength and toughness were necessary for successful applications of HA disks in load-bearing bone grafts. These properties depended on the characteristics of the HA powder such as particle size, morphology and crystallinity. These properties would affect its operational effectiveness. Due to the good flowability, bioactivity and good contacts between particles of spheroidized HA, it has been used as the feedstock for coatings and sintering processing [25, 40]. In this study, spheroidized calcium phosphate (CaP) powders processed in a RF plasma system were used as feedstock for the bulk materials.

Many advanced sintering techniques such as microwave sintering [147], spark plasma sintering (SPS) [148], have been widely adopted to get fully sintered HA bulk with enhanced mechanical properties. SPS was one of the newest developed technologies for fine powder consolidation, which enabled a powder compact to be sintered within minutes through rapid Joule heating and spark plasma or spark discharge generated by the high pulsed current. The SPS process was an *in-situ* cleaning method creating pure materials. The materials were rapidly densified to high densities from the powder form.

During the SPS process, neck formation among the powders was attributed to the effect of spark plasma caused by the pulse electric current. The particle surfaces were

activated electrically by the application of an ON-OFF pulse voltage and current. In return, a momentary plasma generated between the powder particles.

Several advantages arose from using SPS as a consolidation method. Firstly, the resistance heating of particles shortened significantly the high temperature exposure of powders. The sintering duration was essential to preserve the initial microstructure. Also, the electrical energy that was supplied in combination with mechanical pressure contributed to very short actual consolidation times, thereby preventing the formation of coarse microstructures. Secondly, the discharge plasma that was generated between powder particles conferred a significant surface cleaning ability that led to enhanced particle sinterability. SPS led to consolidation of powders with the removal of previously formed surfaces, combined with pressure and electrical field application. There was the possibility of preserving the initial grain size during the densification process, thus leading to extremely pure consolidated materials with improved mechanical properties. This concept has attracted special interest from both industry and research institutes.

In this chapter, an SPS system was used to sinter rCaP and spray dried powders. Sample dimensional changes of these powders were characterized to monitor the spark plasma sinterability. The obtained disks were characterized using XRD, SEM, and Raman spectroscopy. The possibilities of silicate substitution in the apatite were evaluated using Raman spectrometer and XPS analysis. In addition, mechanical properties were investigated using the micro-hardness tester.

6.1 Preparation of SPS samples

An SPS-1050 system was used to obtain bulky disks. One gram of loose powder was loaded in a graphite die (13 mm in diameter) and punch unit. A low pressure was

initially applied. The maximum pressure level ranged from 15 MPa to 34 MPa. The temperature was first raised from room temperature to 600 °C with a heating rate of 200 °C/min, and then heated to the preset sintering temperature at a heating rate of 100 °C/min. After keeping the samples at a desired temperature and pressure for the pre-set duration, the applied electric current was stopped; pressure was released, and the sample was cooled to room temperature at cooling rate 100 °C/min. The samples were brought out of the SPS machine for the following characterization.

6.2 Characterization of SPS RF plasma processed HA powders

6.2.1 Results

6.2.1.1 XRD and Raman analysis

The starting powder for SPS was prepared in RF plasma at 21 kW. The XRD patterns of the sintered samples using SPS were shown in Figure 6.1. It was found that HA was the predominant phase in all these disks. β -TCP was detected in the SPS disks sintered below 1150 °C. While, α -TCP instead of β -TCP (JCPDS 9-169) were detected in the samples sintered at above 1150 °C. Small amounts of CaO were traced. But no TTCP was found in all samples. The peaks of aluminum were attributed to the XRD holder material.

The chemical composition of the SPS samples were obtained through XPS and tabulated in Table 6.1. It revealed that the atomic ratios of Ca/P for SPS disks were not exactly corresponding to that of stoichiometric HA (1.667). The Ca/P ratio of the SPS samples was smaller than that of stoichiometric HA. TCP had a Ca/P ratio of 1.5 that was lower than that of stoichiometric HA. The relatively large amount of TCP and small amount of CaO in the SPS compacts (as shown in Figure 6.1) resulted in a lower Ca/P ratio after spark plasma sintering.

To study the changes in PO_4^{3-} groups, and the functional groups such as OH^- , HPO_4^- and CO_3^{2-} in the SPS samples at different sintering temperatures, the SPS samples were studied using Raman spectroscopy. Figure 6.2 showed typical Raman spectra of synthesized SPS compacts.

In the ν_1 phosphate mode region that located around 960 cm^{-1} , except the peak at 962 cm^{-1} should be attributed to the symmetric phosphate stretch from HA. Additional bands at 947 cm^{-1} and 954 cm^{-1} would be due to the existence of secondary phases influence, such as TCP. α -TCP and β -TCP exhibited the same region in Raman spectra. Doublet at 940 cm^{-1} and 947 cm^{-1} would confirm the presence of TTCP, which was not detected in the disks but in the feedstock as discussed in Chapter 5. Additional observed bands in SPS samples were the bands in 2000 cm^{-1} region. Based on the observation made by Park et al [149], those bands were assigned to $2\nu_3$ of phosphate ions overtones and/or a combination band of ν_1 and ν_3 of phosphate ions. The carbonate vibration bands locating within $1300\text{--}1500\text{ cm}^{-1}$ were also detected, which were due to the influence of graphite die during sintering.

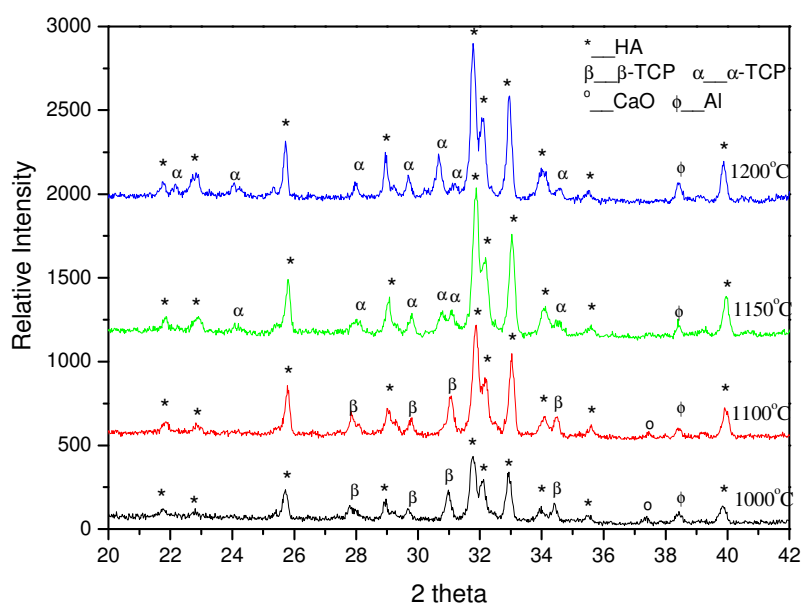


Figure 6.1 XRD results of SPS disks sintered at different temperature.

Table 6.1 Chemical analysis results of the powders and disks.

Sintering temperature	Ca/P ratio
1000 °C	1.559
1100 °C	1.623
1150 °C	1.621
1200 °C	1.667

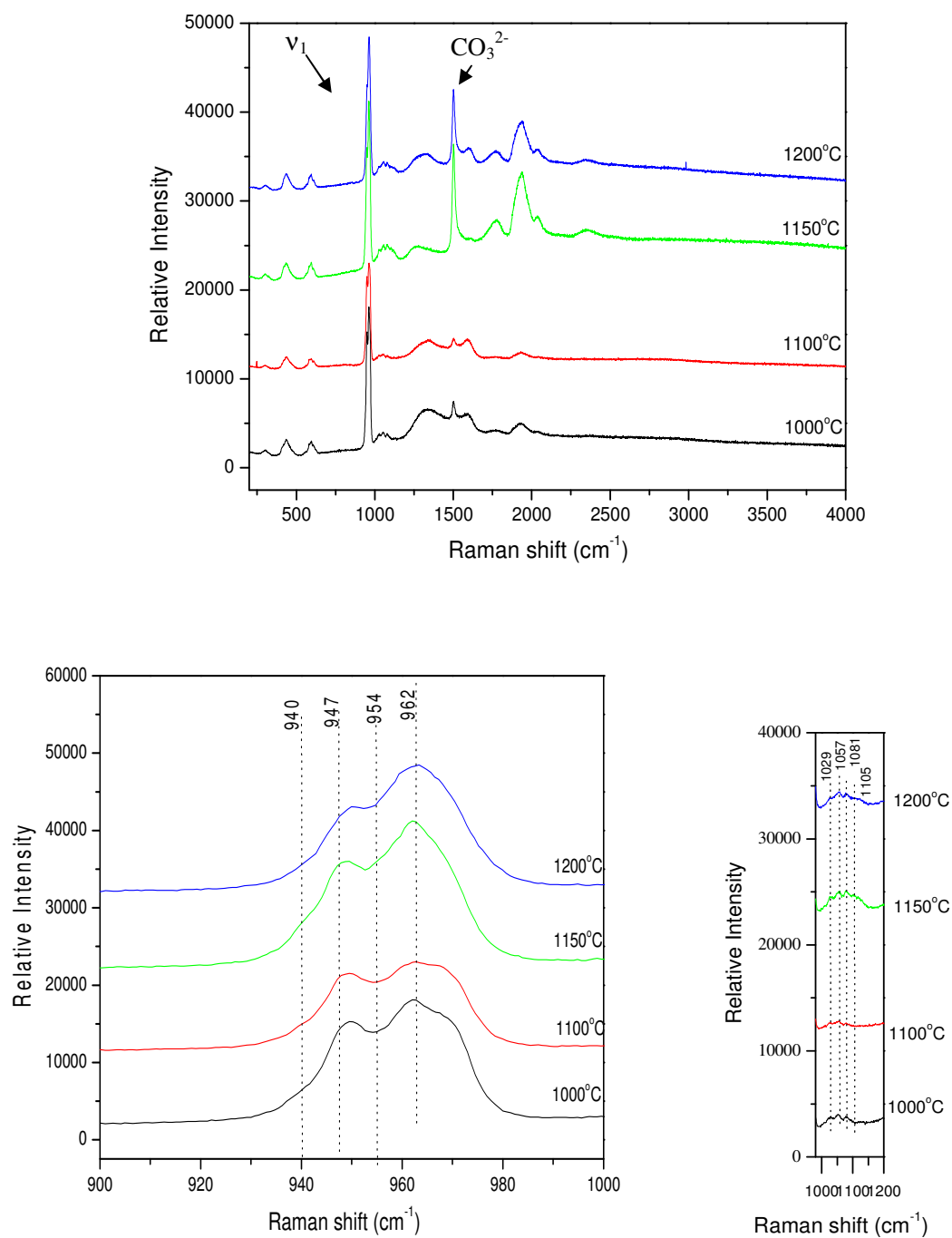


Figure 6.2 Raman patterns of SPS compacts.

6.2.1.2 Fracture surfaces analysis

Two processes occurred during sintering that included densification and grain growth. Figure 6.3 showed the SEM images of the fracture surfaces of compacts prepared at various sintering temperatures. It was well known that the main driving force in sintering was the surface free energy of the particles. The surface free energy increased quickly with the decrease of particle size. Correspondingly, sintering temperature of ultrafine particles was lower than that of larger particles. Thus, as shown in Figure 6.3 (a-b), the fine particles in the spheroidized CaP powders first sintered due to high surface energy at 900 °C, while the large primary particles presented obviously weak bonding. The large particles began to agglomerate together at ~1000 °C. Many pores were connected together. No obvious grain boundary networks were formed. With the increase of the sintering temperature to 1100 °C and 1150 °C, as shown in Figure 6.3 (e-h), pores became isolated and located at grain interfaces or entrapped in grains. Grain boundaries formed a continuous network. For a high SPS temperature of 1200 °C, the spheroidized powders exhibited significant grain growth, with some grains reaching approximately 5 μm in size (Figure 6.3 (i-j)).

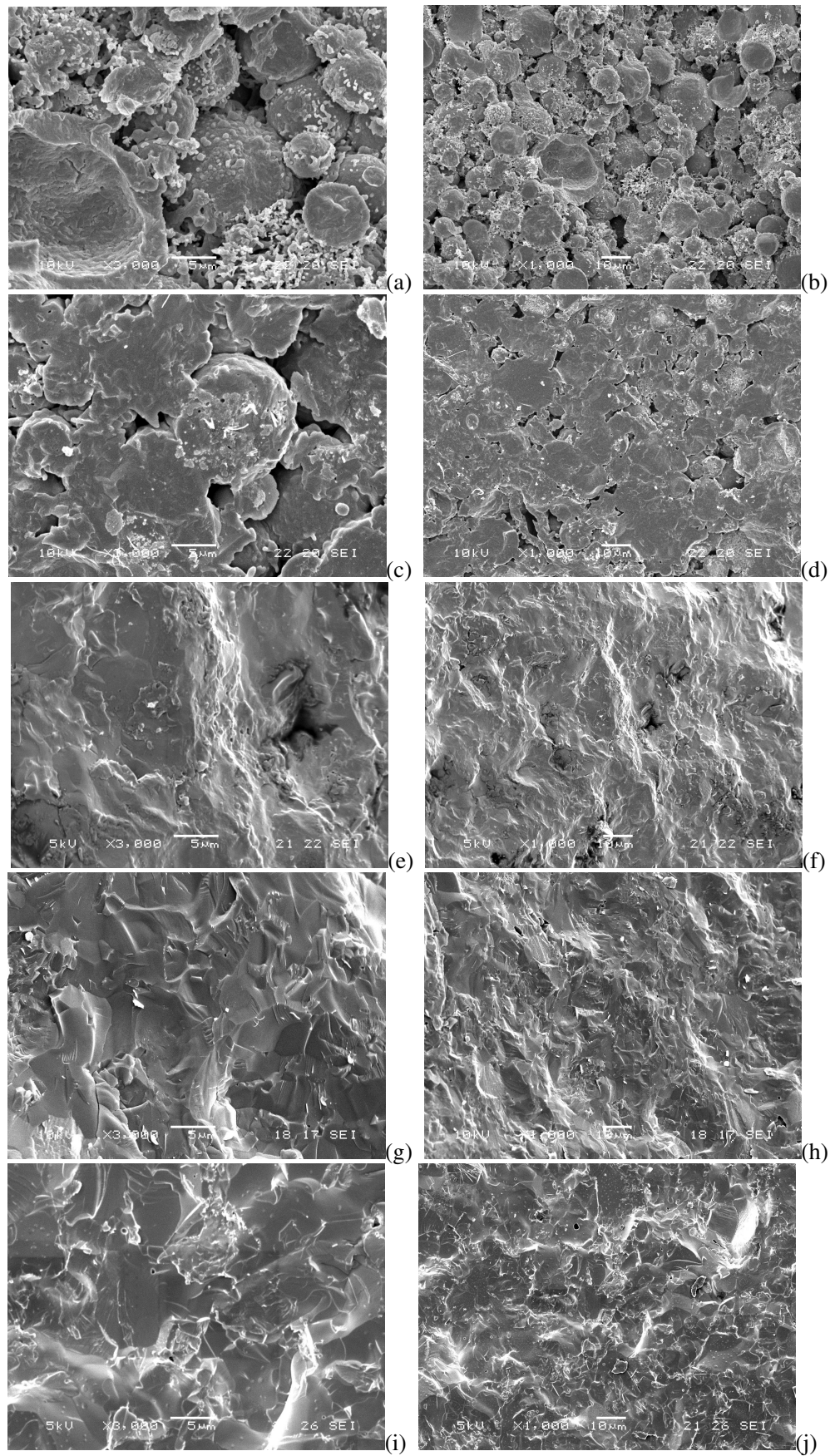


Figure 6.3 Fracture images of SPS compacts sintered at different temperature for 3 min:
(a)-(b)900 °C; (c)-(d)1000 °C;(e)-(f)1100 °C;(g)-(h)1150 °C; (i)-(j)1200 °C.

6.2.1.3 SEM images after polishing

The SPS compacts were polished and etched in nitric acid (2 vol %). Under SEM, the micro-structural features of these disks revealed the sintering trends with respect to sintering temperature. As observed in Figure 6.4, three different contrast domains were observed, which were marked as M, N, and D, respectively.

N region shown in Figure 6.4 (b) was due to high dissolution rate in the nitric acid. Because of size effect, the nano-scale particles had very great interfacial volume as well as point defects from the rapid thermal spraying. Those defects could lead to higher dissolution compared with micron size particles [150]. Therefore, the N region was attributed to the sintering area obtained from the nano-scale particles that presented in the feedstock. The M domains presented nearly spherical shape corresponding to the micron particles from the powder feedstock. They were surrounded by the N regions. When compared with Figure 6.4 (a), similar structures (shown in Figure 6.4 (c)) were observed in the sample sintered at 1100 °C.

Figure 6.4 (e-h) presented the morphology of disks sintered at higher temperatures of 1150 °C to 1200 °C. It was found that the increase in the sintering temperature resulted in the coarse microstructure. N domains became apparently smaller. M domains became characteristically elongated and irregular. The decrease in N domains was due to the coalescence of between M and N domains and/or the nano particles consumed into the micron particles during the sintering process. Under the optical microscope (Figure 6.4), many dark areas (D region) were detected in SPS disks. These D regions were relatively spherical in shape. However, it was difficult to exactly determine these dark regions using optical microscope. Further SEM analysis was needed to reveal these regions.

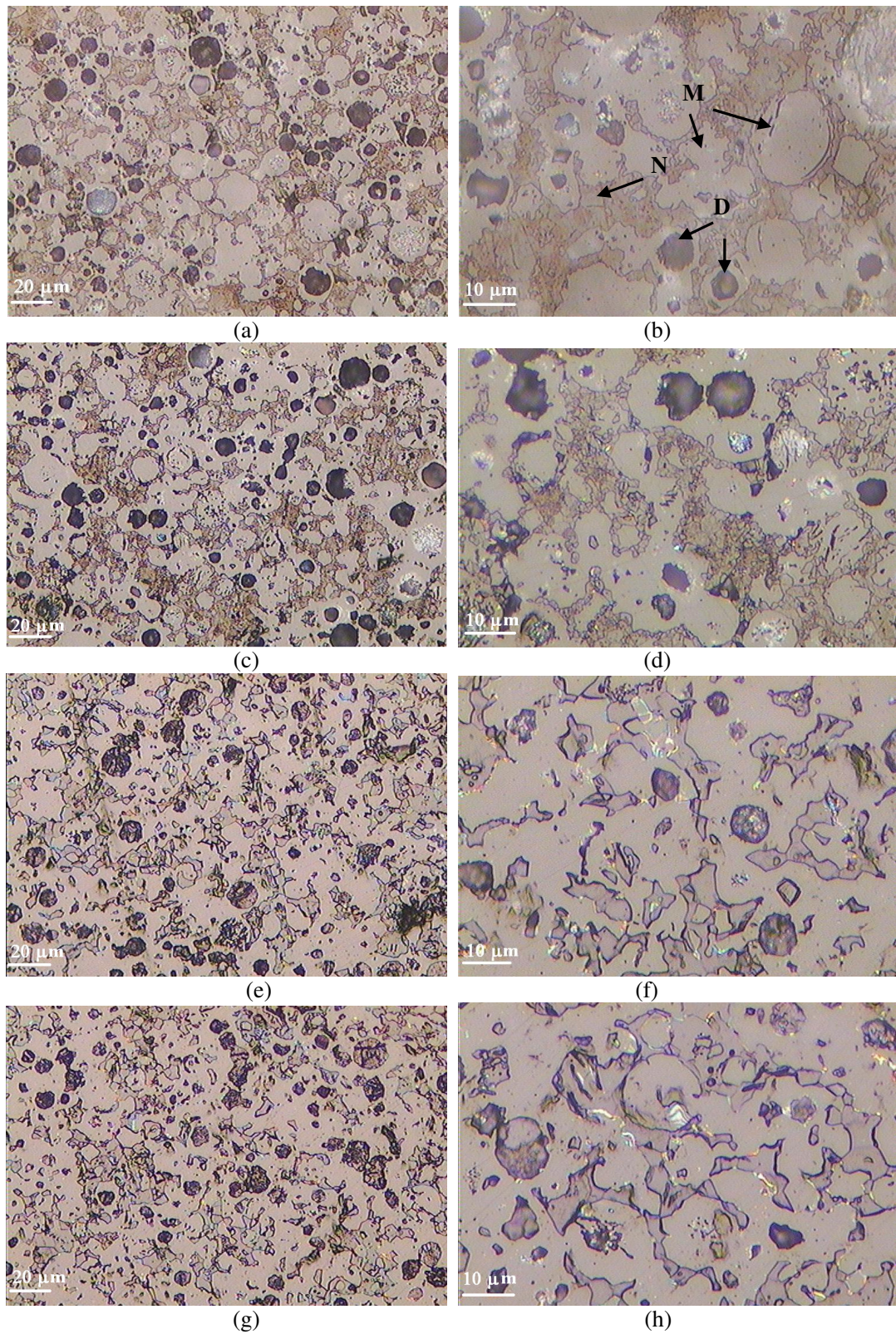


Figure 6.4 Etched optical morphology images of SPS disks sintered at:

(a, b) 1000 °C, (c, d) 1100 °C, (e, f) 1150 °C, (g, h) 1200 °C.

As presented in Figure 6.5, SEM images provided complementary information on the formation of different regions. It was found that the D regions under optical microscope were hollow-structured parts (pointed by white arrows in Figure 6.5 (b)) within these disks. SEM mapping results continually proved the presence of hollow structure in the SPS samples (Figure 6.6). Formation of a hollow into the particle had been elaborated in Chapter 5. The presence of hollow spheres would result in the porous structure after SPS processing, which were detrimental to the mechanical properties of the disks. Nearly spherical hollow structure in the disks indicated that the densification did not finish below 1100 °C. As presented in Figure 6.5 (e-f), few spherical hollow parts or pores were observed in the sample prepared at 1150 °C, which revealed that the densification had almost finished. Finally, after sintered at 1200 °C, nearly fully densified structure was obtained as shown in Figure 6.5 (g-h). Considering the XRD results, the decomposition of HA into α -TCP was taking an effect for the further sintering. Also, the grain growth would contribute mainly to the stage of sintering.

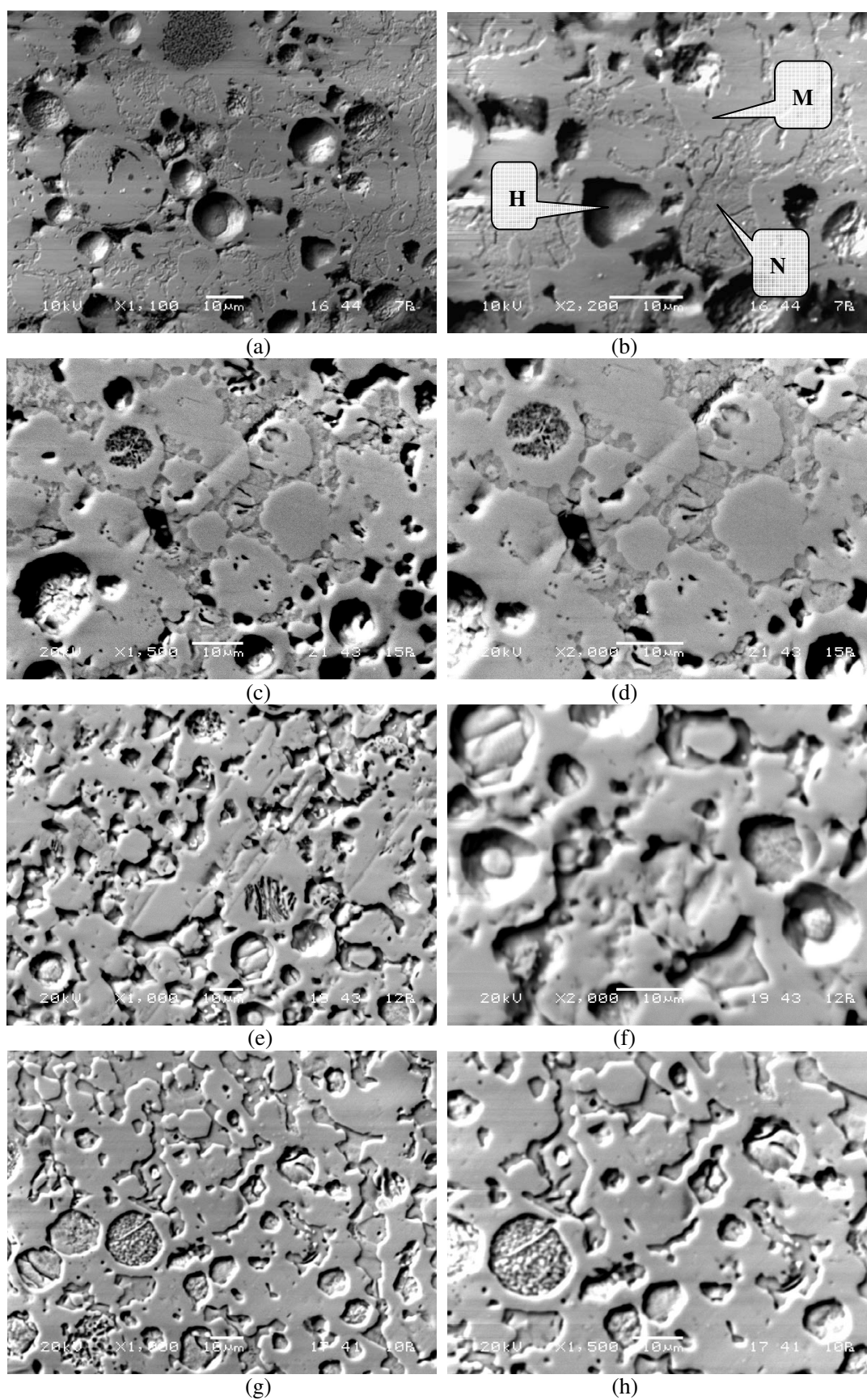


Figure 6.5 Low vacuum SEM morphologies of SPS samples after etching in nitric acid for 10 s:

(a, b) 1000 °C, (c, d) 1100 °C, (e, f) 1150 °C, (g, h) 1200 °C at 34 MPa for 5 min.

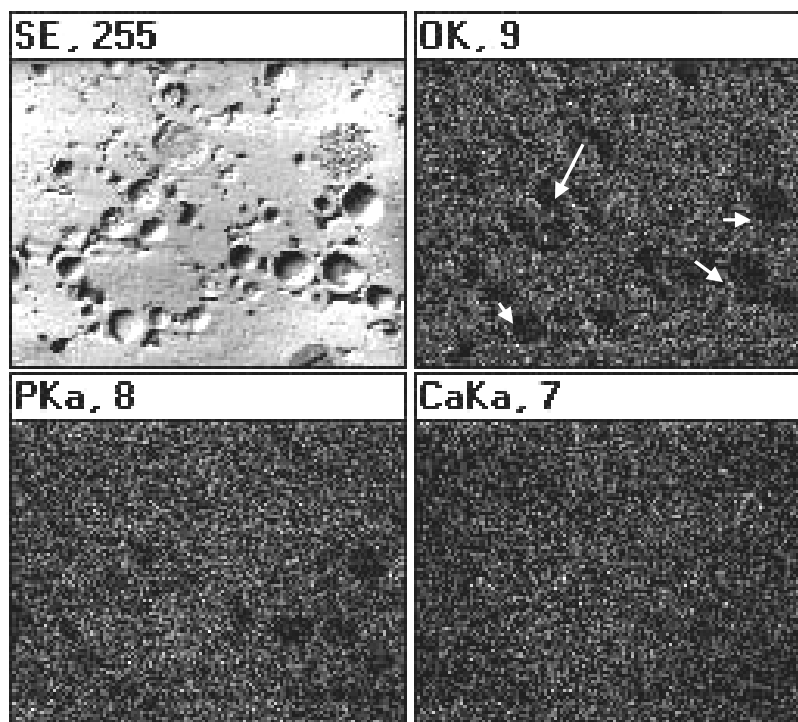


Figure 6.6 Elements mapping results of SPS ceramic sintered at 1000 °C.

6.2.1.4 Shrinkage behavior of SPS samples

To fully understand the sintering process of the RF plasma synthesized powders in the SPS system, the densification behavior was investigated through the sample displacement and displacement ratio. The starting powders were heated to 600 °C at the heating rate of 200 °C/min, and then heated to 1200 °C at heating rate of 20 °C/min. The sample was kept for 10 min at the sintering temperature of 1200 °C. Then it was cooled to 600 °C (the lowest controllable temperature of SPS) at the heating rate of 50 °C/min.

The experimental displacement and displacement ratio versus temperature curves were shown in Figure 6.7. The general trend was that the powders showed three-stage shrinkage behavior. First, the slight shrinkage occurred between 550 °C to 650 °C. During this period, the powders were pressed uniaxially in carbon die. An on-off of

direct current voltage was applied simultaneously. Then the current passed through the die and sample. The sample was heated from both outside and inside. A discharge between the particles occurred initially. The plasma formed through the sample. Thus, the heat and plasma promoted rapid densification at lower temperatures and short holding times. Desorption of absorbed moisture in the wide size distributed powders also contributed to the shrinkage within this region [151].

At about 720 °C, the displacement increased a little and the displacement ratio was larger than zero. This stage was due to that the temperature has caused the dilation of the sample. Shrinkage occurred high to 900 °C and continued high to 1150 °C. This shrinkage indicated that densification of the powders occurred by sintering. The broad temperature range of this transition might be also due to the wide particle size distribution of the powders. From 920 °C to 1060 °C, the shrinkage increased much rapidly. This was attributed mainly to the densification at the early stage (<90% of relative density). After sintered at 1000 °C, XRD analysis revealed that only α -TCP transformed to β -TCP, but the density was more than 90% of relative density and about 3.00 g/cm³. From 1060 °C to 1150 °C, the shrinkage increased moderately. This was attribute mainly to the final stage of sintering (>90% of relative density). As shown in Figure 6.8, the densities of the disks during this temperature range exhibited some increase as the increase in sintering temperature. The densities of samples after sintered at 1100 °C and 1150 °C were 3.04 g/cm³ and 3.05 g/cm³, respectively.

At above 1150 °C, no additional shrinkage was found in Figure 6.7 after the sample was kept at 1200 °C for 10 min. This finding indicated that the sintering has been finished. The grains in the samples began to increase with an increasing in sintering temperature and time. With the decrease in the temperature, the sample began to

shrink, and no abnormal phenomenon was found.

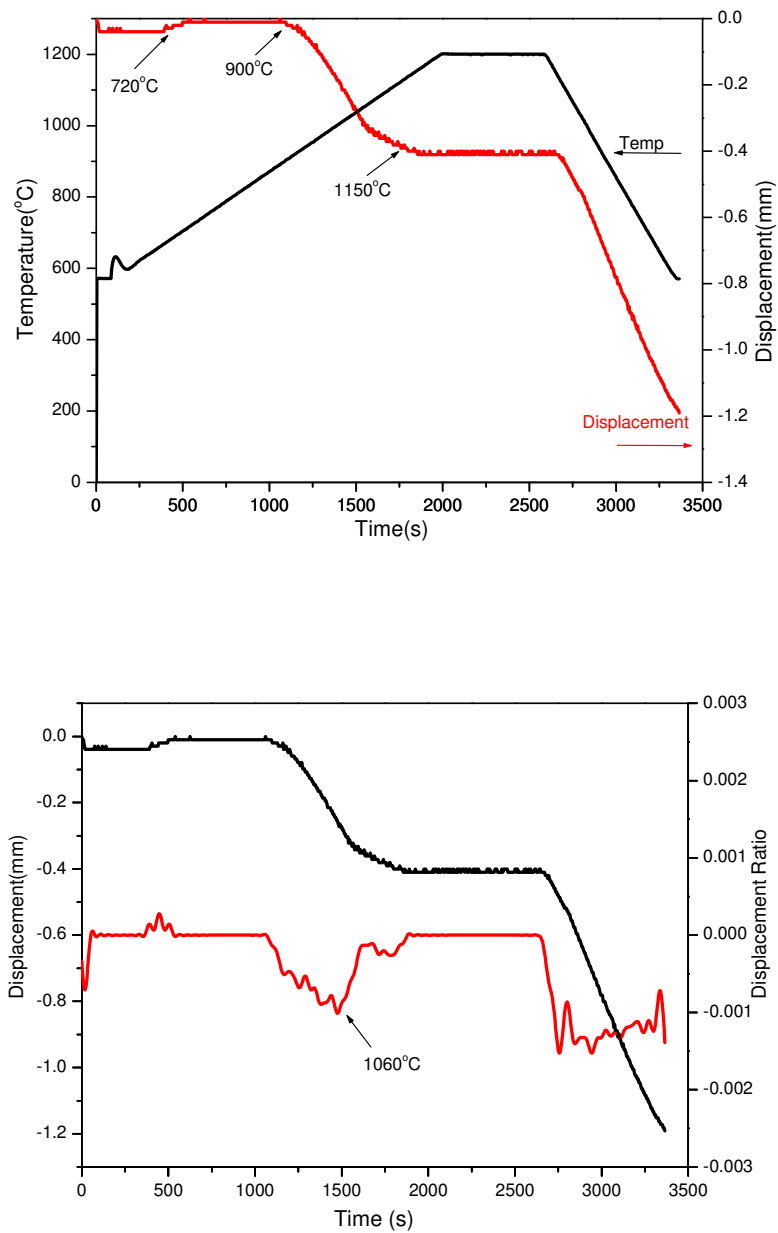


Figure 6.7 Kinetic curves of rCaP ceramic in the SPS system at the heating rate of 20 °C/min to 1200 °C, duration at 1200 °C for 10 min and then followed cooling to 600 °C at 50 °C/min.

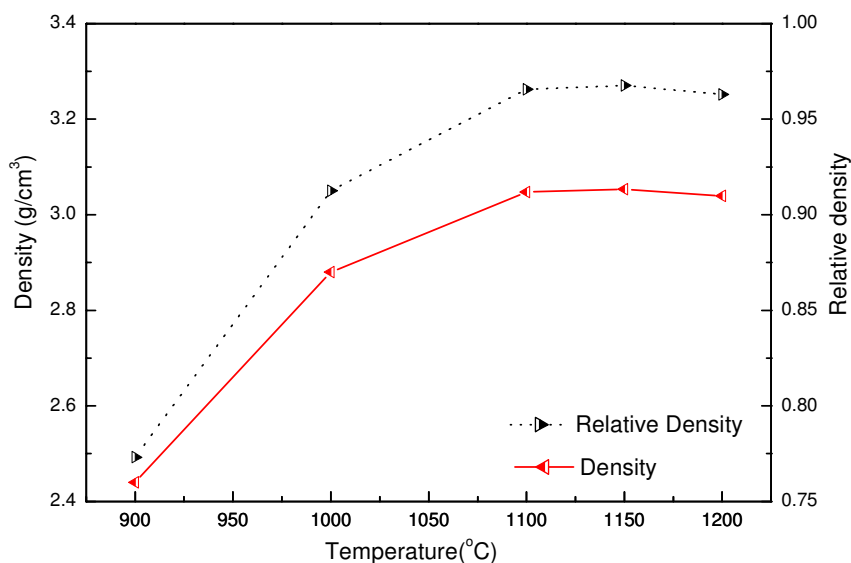


Figure 6.8 Effect of sintering temperature on the densities of SPS disks. Five measurements were averaged for each sample.

6.2.1.5 Mechanical properties

The effect of sintering temperature on the hardness (H) and Young's Modulus (E) of the solidified sample were presented in Figure 6.9. A total of 10 points were averaged for each compacted samples. The results of the sample sintered at 900 °C were not available due to its relative poor structure as shown in Figure 6.3(a)-(b). An increase in hardness occurred at a higher sintering temperature of 1100 °C. Further sintering resulted in a decrease in hardness. The trend in Young's modulus was very similar to the pattern encountered with hardness.

The highest E (about 105 GPa) and H (around 6.2 GPa) were obtained after sintered at 1100 °C. The E and H values increased about 15% when the sintering temperature increased from 1000 °C to 1100 °C. The presence of porosity played a large role in affecting the Young's modulus. Obviously, the decrease of porosity contributed to the increased modulus, as shown in Figure 6.3. In contrast, the further decrease in E and

H from 1150 to 1200 °C could not be ascribed to densification but to the increase in grain sizes from less than 1 μm to 5 μm . As discussed by Gross et al [152], the mechanical properties of disks were sensitive to the grain sizes. Normally, a clear decrease in hardness was expected with larger grain size. The volume expansion caused by the phase transformation of β -TCP to α -TCP also contributed to the decreased E and H. These achieved values were higher than other reports [153, 154], which could be attributed to the good packing ability of RF plasma spheroidized powders and the fast SPS process.

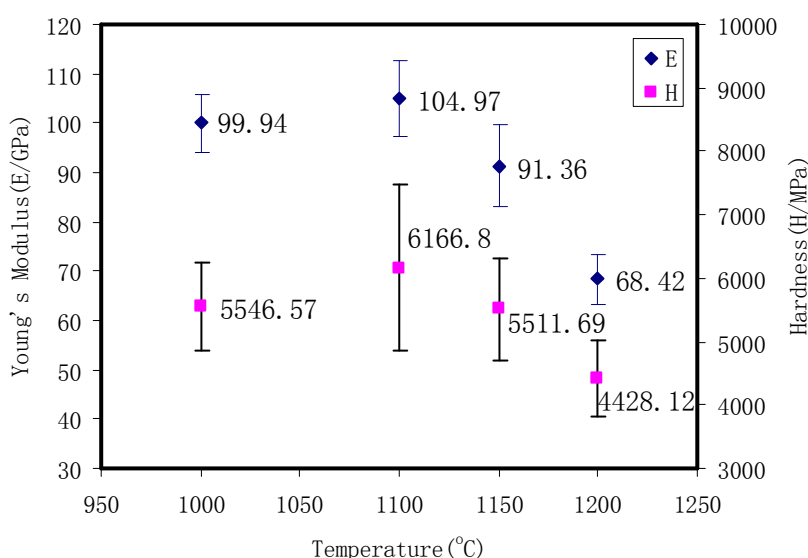


Figure 6.9 Effect of sintering temperature on Young's modulus and hardness of the sintered samples.

Ten points were averaged for each sample.

6.2.2 Discussion

6.2.2.1 Spark plasma sintering behaviors

The microstructure evolution presented in Figure 6.3 showed clearly the sintering steps at different sintering temperatures. Since the densification lowered the surface free energy by the elimination of the interfaces between different particles [155], compared with the micron sized particles, the nano particles had a higher driving

force for densification due to the enormous surface area. Preferential sintering of agglomerates inadvertently happened as discussed in reference [156]. The microstructure shown in Figure 6.4 (a-d) proved that the fine particles sintered to minimize the surface area of the agglomerates. The adjacent micron particles coalesced together.

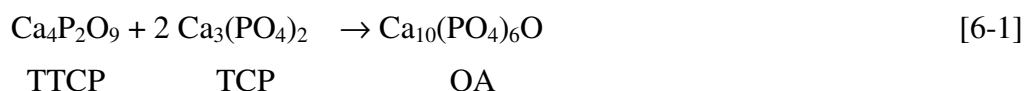
In the present study, the influence of the green compacts should be negligible, since the loose powders were directly loaded in the graphite die. The shrinkage rate during sintering was governed mainly by the driving forces from different sized particles. The influence of particle size distribution on the main two densification mechanisms, particles rearrangement and grain shape accommodation, should be addressed.

RF plasma processed powders had different size-distributed particles. During the sintering process, the smaller spheres might fill the interstices between the larger spheres, and in return, increase the final density. As presented in Figure 6.3 (a-b), the feedstock initially exhibited a faster shrinkage dictated by the fine particles. While, a small fraction of the fine particles was less prone to influence the sintering of the major fraction coarse particles, rather soon the rate decreased to a level according to the coarse fraction. The microstructure development shown in Figure 6.3 indicated that the solutions of these fine particles to the micron particles led to contacted large spheres sintering. These densifying mechanisms between the different particles dominated the sintering procedure up to the temperature (1060 °C), where the maximum shrinkage rate reached. Above this temperature, the sintering was controlled by non-densifying mechanisms, such as grain growth and pore growth [157], and solution of smaller grains led to an increasing mean grain size. Therefore, as shown in Figure 6.8, the highest sintering density was obtained at around the

sintering temperature of 1100 °C. The densification process at the sintering temperature above 1100 °C was independent of the particle sizes, and the grains growth mainly dominated in the sintering.

6.2.2.2 Phases analysis

As presented in the XRD patterns, HA and TCP were presented in the SPS disks. During spark plasma sintering process, some TTCP and TCP in the powder feedstock would react together to form oxyapatite (OA) according to the following chemical formula [6-1]:



Though the lattice parameters of oxyapatite were different from those of hydroxyapatite, it still could not be differentiated directly by XRD.

As discussed by Lin et al [106] and Chen et al [112], TTCP was less stable than TCP because the crystal structure of TTCP was similar to HA that promoted the crystal growth of HA during heating. Thus, part of TTCP would also react with the OH⁻ group to convert to HA and Ca(OH)₂ by the following hydrolytic reaction:

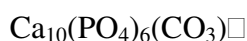


It was difficult to trace the characteristic peaks of Ca(OH)₂ in XRD patterns because too small amount of this phase might occur, and most of the peaks were overlapped with those of HA.

It was also suggested by Lin [106] that α-TCP would transform to β-TCP at the temperature ranged from 500 °C to 900 °C. β-TCP was low temperature polymorph of tricalcium phosphate. It would transform at approximately 1120 °C to the high

temperature polymorph α -TCP [158]. The transformation of α -TCP (from spheroidized powders) to β -TCP at low temperature, and from β -TCP to α -TCP at high temperature during SPS process, would cause deleterious volume variation [50]. This variation led to the decrease of mechanical properties. The presence of α -TCP and β -TCP would also contribute to that the relative low densities of the sintered samples, which did not reach densities higher than 96% because their densities (α -TCP 2.88 g/cm³, β -TCP 3.07 g/cm³) were lower than that of HA (3.156 g/cm³). Though TCP would decrease the mechanical strength of the sintered samples, its biocompatibility should be considered due to its fast dissolved behavior, which could improve the relatively fast new bone growth after implantation. The CaO had no biocompatibility. It was considered to be the most detrimental phase following implantation [159].

As shown in the Raman spectra (Figure 6.2), except the peaks belonged to phosphate groups, vibration of carbonate ions ν_3 was observed in SPS samples. During SPS processing, carbon from the graphite die would react with the feedstock due to the high enough driving force caused by the plasma. Therefore, carbonate would partially substitute into the disks, and detected by Raman spectrometer. Two types of carbonate substitution have been described: type A (OH^- substituted by CO_3^{2-}) and type B (PO_4^{3-} substituted by CO_3^{2-}). The substitution of carbonate ions for OH^- or PO_4^{3-} ions induced the creation of vacancies and distortions in the atomic arrangement. For type A carbonate apatite, the substitution of a mono-valent ion by a divalent one was compensated for by the creation of a vacancy. The chemical composition could be represented by:



where □ represented the vacancy. This substitution resulted in that the six phosphate groups of the apatite unit cell were no longer equivalent in the lattice but might be split into two groups. One organized around a vacancy and one around a carbonate ion. The shoulder and main band observed in the ν_1 mode region of phosphate could thus be assigned to two different environments (vacant sites or divalent ions). Such a modification of the environment should affect the ν_3 and ν_4 domains phosphate. However, it was more difficult to assess. It was actually impossible to distinguish these two groups like ν_1 . While, shown in Figure 6.2, in the region around 1000-1100 cm^{-1} , the peaks of 1029, 1057 and 1081 cm^{-1} bands belonged to the ν_3 phosphate vibration. A small peak locating at 1105 cm^{-1} should be attributed to the type A carbonate substitution [160]. The band at 1105 cm^{-1} was very specific of carbonate groups substituting OH^- ions. It could be considered as a signature. The type A substitution would contribute to the decrease of hydroxyl ions in the spectrum, as the hydroxyl band presented in the spectrum of carbonated apatite was weaker in intensity than that in pure HA.

No obvious vibration of hydroxyl (Figure 6.2) was detected in the region of 3570 cm^{-1} region, which supported the formation of dehydrated apatite in the final SPS disks. During the feedstock production through the RF plasma processing, in an atmosphere free of water vapor, it was quite impossible to obtain stoichiometric HA because of the decomposition of the hydroxide ions:



which led to the formation of an oxyhydroxyapatite and oxyapatite in the feedstock for SPS. The amount of O^{2-} ions formed depended largely on the temperature and water pressure. Continued high temperature in SPS would accelerate the dehydration process. Thus the reduction on the relative intensity of hydroxyl stretches should not

only be attributed to the type A carbonate substitution but also be attributed to the partially dehydration caused by the high temperature steps.

6.3 SPS of silica doped HA (SiHA)

The low mechanical properties, relatively long time for remodeling and slow rate of osseointegration had limited the medical application of synthetic HA [133]. Due to slightly chemical difference found in the structure of natural bone mineral, the natural HA appeared to have a higher bioactivity compared with the synthetic HA. A significant number of different ions might be substituted on a number of different sites, e.g. CO_3^{2-} for OH^- or PO_4^{3-} , and Mg^{2+} , Na^+ for Ca^{2+} . It was important to incorporate these trace elements into the synthetic HA because the biocompatibility of apatites depended highly on their composition.

Therefore, synthesis of chemically modified or ion-substituted HA [185] has drawn great interest since the ions played an important role in developing artificial bone with enhanced mechanical properties and bioactivities. It was reported [134] that the silicate ions into HA structure improved its *in vivo* bioactivity. Si-substituted HA became an attractive alternative to conventional HA materials for use as bone substitute disks. Silicate ion substitution was also reported [186] to enhance the formation of a poorly crystalline surface apatite layer on HA after immersing in SBF. This study tried to get a new silicon-substituted HA using spark plasma sintering and RF plasma processing steps. For this purpose, a small level of silica (1 wt-5 wt %) assembling to those found in natural bone was introduced in HA slurry before spray drying process, as introduced in chapter 4. The spray dried HA powders doped with 1wt % of silica was also processed through RF plasma before sintering. The obtained powders were sintered through the SPS system. XRD and XPS were used to analyze

the substitution possibilities of phosphate by silicate. For convenience, Table 6.2 illustrated the feedstock and type IDs of SPS ceramic samples analyzed in the present study.

Table 6.2 SPS disks feedstock and classification.

SPS disks feedstock(ID)	SPS ceramic type IDs
Spray dried HA(pHA)	HA
Spray dried 1wt% silica doped HA (p1SiHA)	1SiHA
Spray dried 3wt% silica doped HA(p3SiHA)	3SiHA
Spray dried 5wt% silica doped HA(p5SiHA)	5SiHA
RF plasma processed 1wt% Silica doped HA(prSi)	rSi

6.3.1 Results

6.3.1.1 Phase analysis of SPS SiHA

Figure 6.10 (a) showed the XRD patterns of SPS disks doped with different amount of silica. The XRD pattern of sintered spray dried HA did not reveal any other peak than HA. When the silica-doped HA (SiHA) powders were sintered in the same temperature range with HA, however, the apatite structure was less stable. β -TCP was detected in the SiHA samples. This result indicated that the presence of silica enhanced the decomposition process of HA. Referring to the relative peak intensities of β -TCP, the contents of β -TCP in the SPS disks were found to increase with an increased dopant level of silica. The amount of β -TCP was critical as these phase change would bring about transformation toughening through the residual stress, which might limit the probability of failure.

Table 6.3 presented the lattice parameters (a and c) of the SPS disks that were determined through the (*hkl*) peaks positions of HA from XRD patterns according to

the following formula:

$$1/d^2 = 4/3 \cdot (h^2 + hk + k^2) / a^2 + l^2/c^2 \quad [6-4]$$

d was the lattice distance obtained from XRD results. Compared with the lattice parameters of HA, those of the compacts were relatively large. Concerning the silicate and phosphate groups, the average lengths of the Si-O and P-O bonds were 1.62 Å and 1.51 Å, respectively. The substitution of P-O by Si-O would contribute to the increase in the lattice parameters of SiHA compacts. If the incorporation of CO_3^{2-} ions into the apatite lattice by occupying the OH^- sites in the apatite structure, the lattice parameters would also be relatively large.

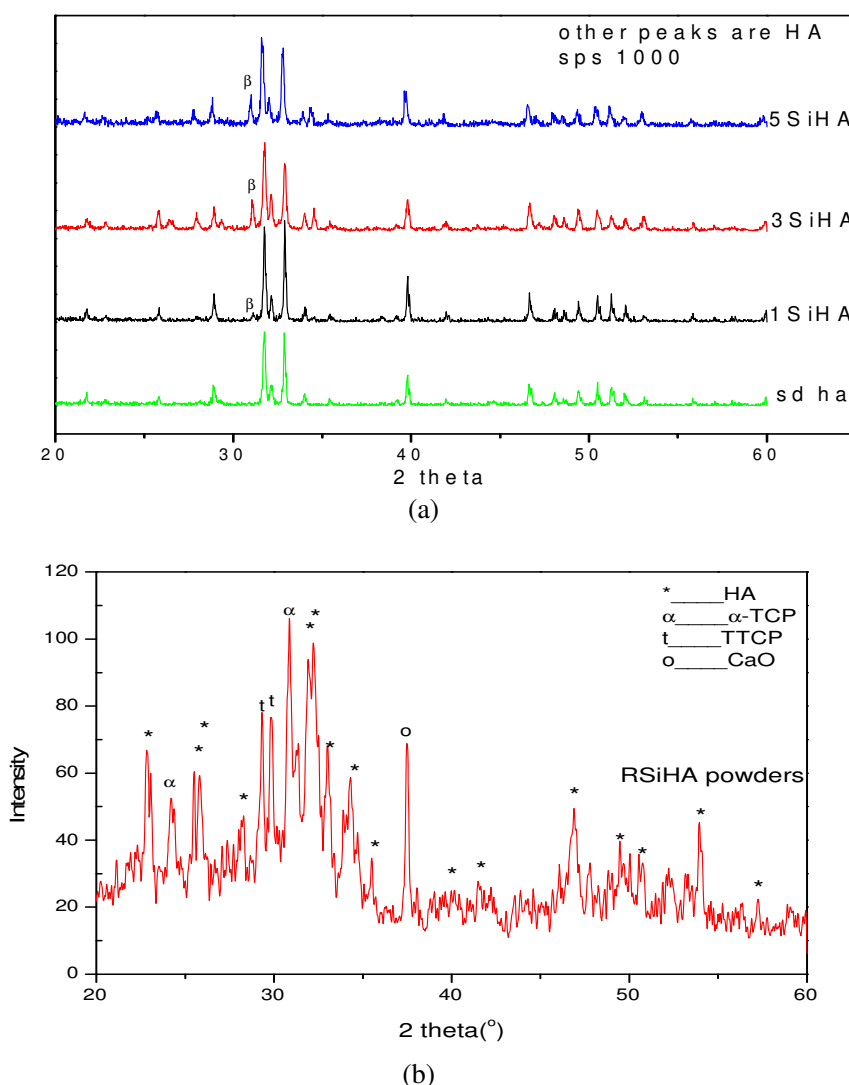


Figure 6.10 XRD patterns: (a) SPS disks doped with different amount of silica; (b) RF plasma processed HA powders doped with 1wt % of silica.

Table 6.3 Lattice parameters of SPS compacts.
Three measurements were averaged for each sample.

Samples	a-axis (Å)	c-axis (Å)	Unit cell volume (Å ³)
SD	9.4182	6.8810	528.5889
1SiHA	9.4235	6.8900	529.8761
3SiHA	9.4227	6.8970	530.3244
5SiHA	9.4352	6.8984	531.8403

The XRD pattern of the RF plasma sprayed silica doped HA powder (prSi) was presented in Fig 6.10 (b). HA, TTCP, α -TCP, and CaO were detected. Due to the low amount level of silica, no phases related to silicate were traced. From the phase fractions in the collected powders shown in Table 6.4, it was found the presence of silica accelerated the decomposition of HA into other phases after RF plasma processing. Only around 28.8 wt % of HA was detected within the crystalline domain of the obtained powders. This result was much lower than that 35 wt% of HA in powders without silica which was processed at the same working conditions.

Table 6.4 Phases fraction in the RF plasma processed silica powders.

Three measurements were averaged for each sample.

Phases	Weight (%)	Volumetric (%)
HA	28.76	28.24
α -TCP	33.98	35.51
TTCP	32.26	31.76
CaO	5.00	4.49

Typical phosphate vibration modes of SPS disks doped with various amount of silica were shown Figure 6.11 (a). No obvious peak belong to silicates could be differentiated from the vibrations of phosphate due to their similar molecular structure. The strongest line situated at 962 cm⁻¹ was attributed to the symmetric stretching ν_1 mode of PO₄³⁻. The peaks situated at 1040 and 1090 cm⁻¹, 571 and 603 cm⁻¹ and 430 and 450 cm⁻¹ were assigned, respectively, to the antisymmetric stretching ν_3 , the

antisymmetric bending ν_4 modes and the bending ν_2 of the PO_4^{3-} ions. The peak around 1350 cm^{-1} was attributed to carbonate ν_3 modes.

The intensities of hydroxyl absorption band at 3571 cm^{-1} decreased slightly with an increase in doping silica. It indicated that the presence of silica might accelerate the breakdown process of the hydroxyl group in HA. Some vacancies or oxygen ion might substitute the hydroxyl sites leading to a distortion of the hexagonal symmetry. The distortion of the hexagonal symmetry would lead to the decomposition of apatite into β -TCP. The formation of OH vacancies has been proven to be able to accelerate cation transport in the HA lattice, which would accelerate the whole sintering process.

The slight loss of OH^- resulted in the formation of positively charged defects in the HA lattice. These defects might charge-compensate by the substitution of SiO_4^{4-} substitution in PO_4^{3-} position in the sintered specimen. As proposed by Sayer et al [161], there should be full charge compensation for substitution. Two possibilities were assumed to compensate the charged defects. The first was the oxygen-deficient or O^{2-} vacancies. The second was the presence of excess calcium Ca^{2+} , charged compensation with the loss of water.

Figure 6.11 (b) presented the Raman spectrum of RF plasma processed 1SiHA powders. Phosphate vibrations were detected. A peak locating at 485 cm^{-1} could be attributed to the presence of silicate in the powders. The other bands originating from the stretching vibrations of the Si-O bond overlapped with the bands of the PO_4 . This was due to the similar types of vibrations between the connected SiO_4 and PO_4 tetrahedron. Additional analysis method should be employed to characterize the chemical presence of silica in the powders.

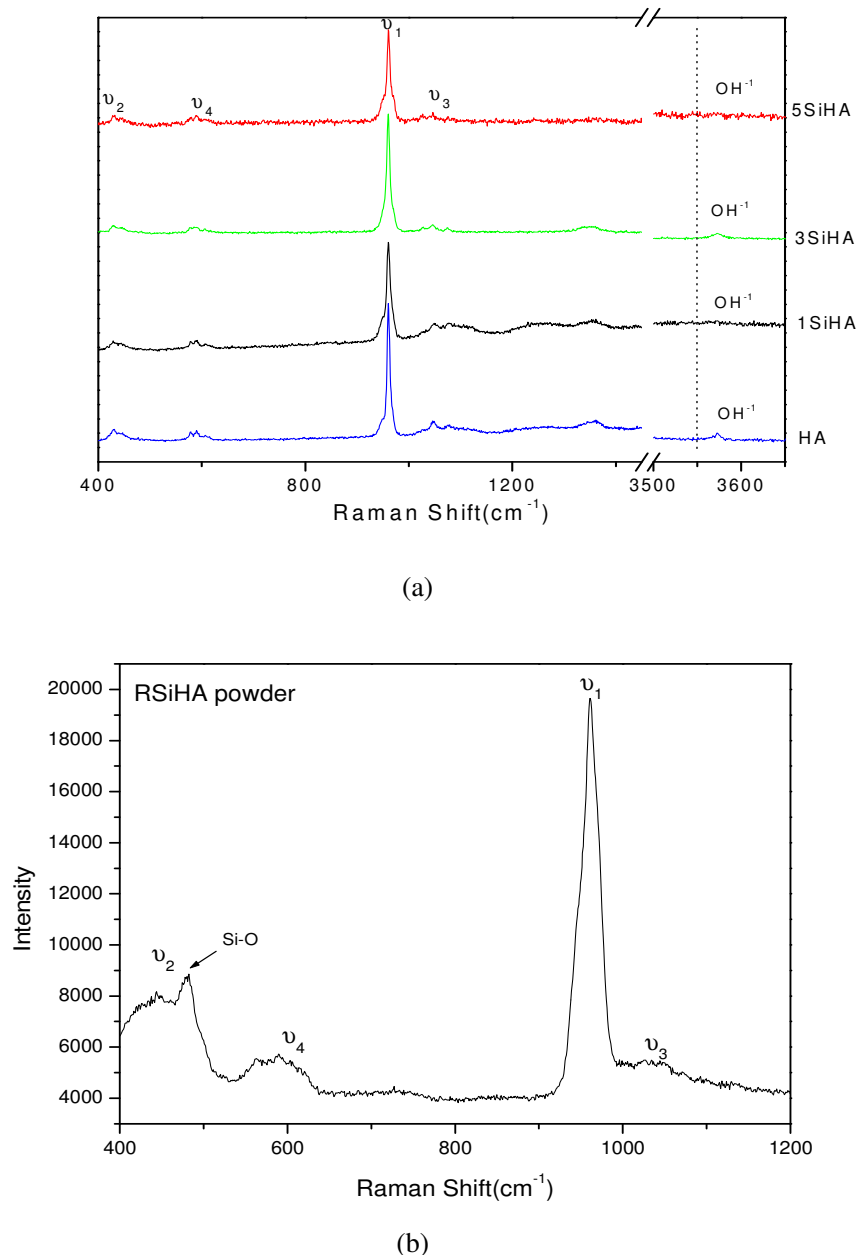


Figure 6.11 Raman spectra: (a) SPS disks doped with different amount of silica; (b) RF plasma processed HA powders doped with 1wt% of silica.

6.3.1.2 Effect of silica on densification of SiHA

The SPS disks were cracked manually. The fracture surfaces were observed under SEM. The images were presented in Figure 6.12. It was found that the fracture modes were fully transgranular. Few pores were detected on the pure SD HA compact, while some intergranular pores occurred in the silica-doped compacts. As discussed

previously, the Si substitution caused the O^{2-} vacancies, and introduced the release of hydroxyl group from HA structure. Therefore, the presence of pores was detected in the disks. The decomposition of HA into β -TCP would also exist near to the pores. The higher the dopant level, the more the presence of pores. As shown in Figure 6.12, the grain sizes (less than 1 μm) of SiHA compacts were obviously finer than that of pure SD HA compacts (around 5 μm), which showed that silica could impede the grains boundary diffusivity in SPS disks. Similar results were also found by Gibson and Bonfield [118] workgroup. They reported that the lowest densities for SiHA disks were obtained for the highest level of silicon substitution. They mentioned that the silicon substitution was also shown to have a clear effect on the grain sizes of the sintered disks; for any given sintering temperature, the SiHA disks had a smaller grain size due to the higher activation energy of grain growth than that of stoichiometric HA ceramic [118].

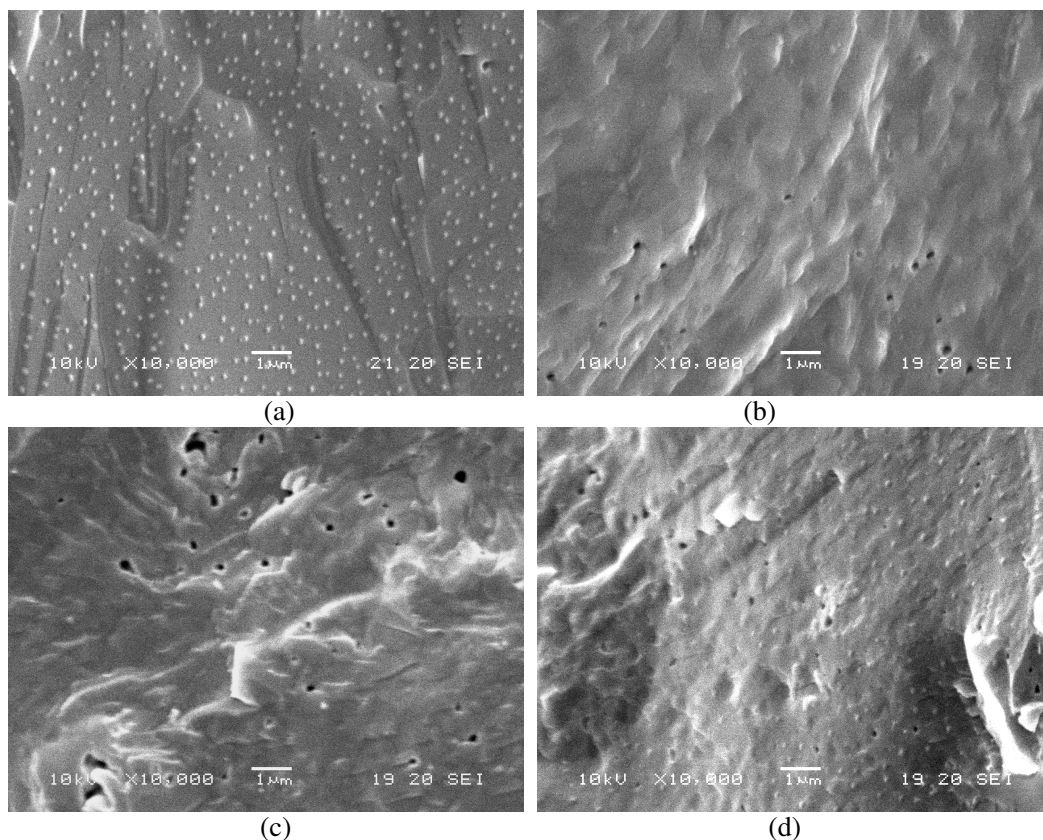


Figure 6.12 Fracture morphologies of SPS disks: (a) HA, (b) 1SiHA, (c) 3SiHA, and (d) 5SiHA.

Table 6.5 listed the average densities and relative densities of sintered specimen disks doped with different amount of silica. It was found that after sintering at 1000 °C for 3 min, the densities of sintered samples decreased as an increase in the doping silica. Although the presence of silica might contribute to the sintered density, the relatively small amounts should not be considered in this study. The formation of pores (in Figure 6.12) and the phase transformation of HA into β -TCP contributed mainly to the decrease of densities.

Table 6.5 Densities and relative densities of spark plasma sintering specimen.

(Theoretical density of HA was 3.156 g/cm³).

Doped silica wt%	Densities (g/cm ³)	Relative densities
0	3.09	97.91%
1	3.05	96.64%
3	3.01	95.37%
5	2.99	94.74%

Three measurements were averaged for each sample.

Figure 6.13 showed the dependence of Vickers hardness (H) and Young's modulus (E) on the amount of doping silica. These values reflected the combined effect of densities and grain sizes. The relatively low hardness obtained for the doped samples was mainly attributed to the low bulk density of the material. It was believed that the higher density had played a role in producing higher hardness values, where an increase in density could lead to an increase in hardness.

The E value of sintered SD HA without silica was around 89 GPa. With the introduction of 1 wt % of silica, the E value slightly dropped to 84 GPa and it increased from 84 GPa to 100 GPa with an increase in doping silica from 1 wt % to 5 wt %. As the sintered densities of SiHA were all slightly less than that of SD HA, the improved E could be attributed mainly to the presence of silica impeding the grain

coarse. These SPS compacts were expected to have a great potential in the applications of dentistry and orthopedics in the future.

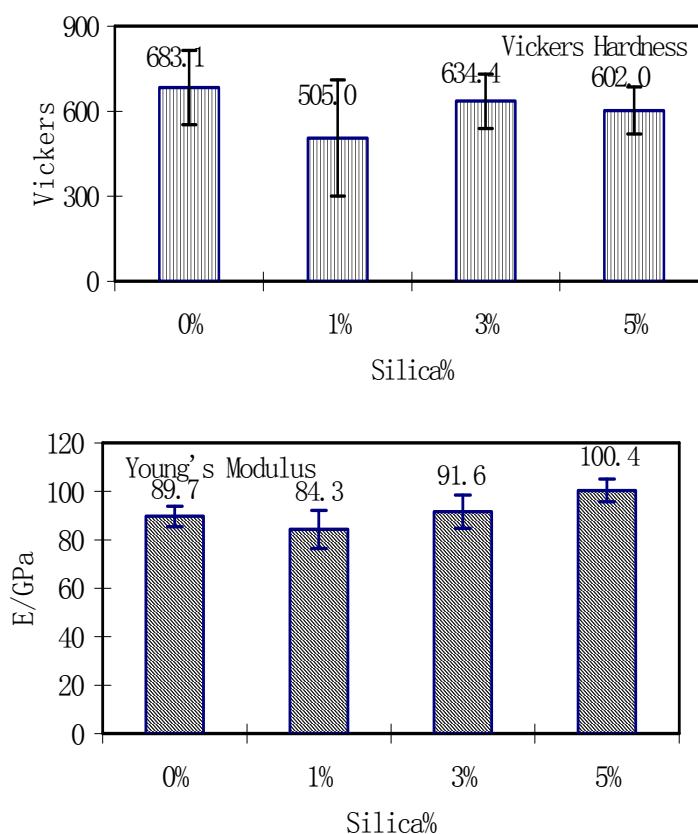


Figure 6.13 Vickers Hardness (H) and Young's Modulus (E) of the SPS disks doped with different amount of silica. Ten measurements were averaged for each sample.

6.3.1.3 Shrinkage behavior

Figure 6.14 (a) and (b) revealed the shrinkage behavior of the r1SiHA and 1SiHA powders during the heating up to 1200 and 1100 °C, respectively. It was found that the densification of r1SiHA started at 897 °C. It stopped shrinking at around 1062 °C. While the sintering for 1SiHA powder started at 718 °C, and continued to 859 °C. The difference in sintering between r1SiHA and 1SiHA could be attributed to the difference in agglomerates as shown in Figure 6.15.

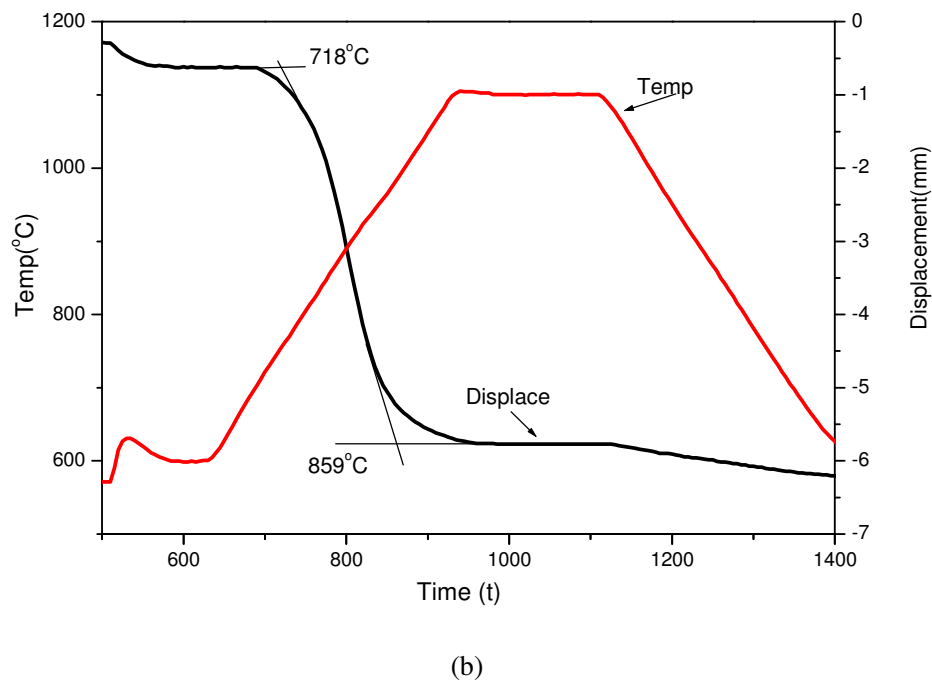
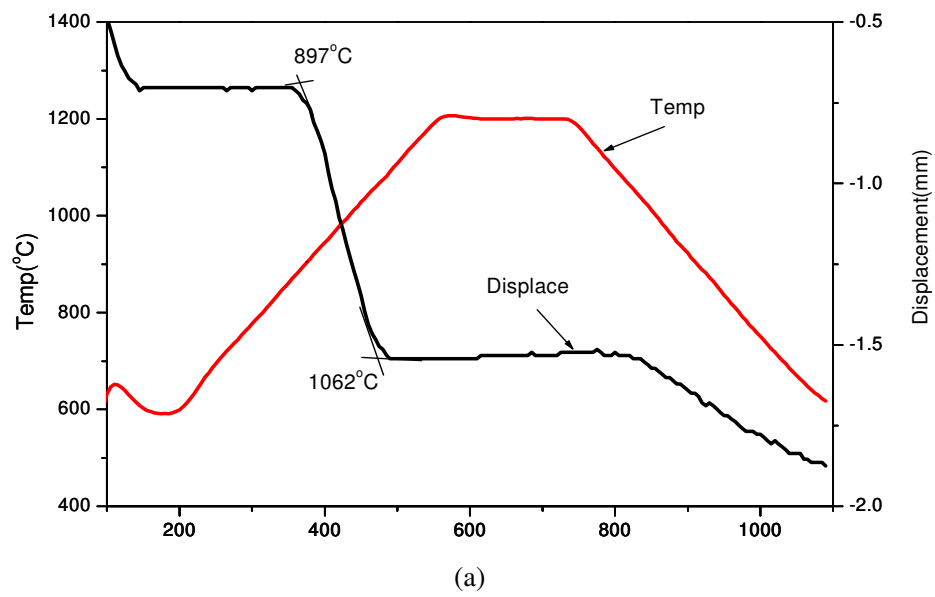


Figure 6.14 Kinetic curves of spark plasma sintering:

(a) RF plasma processed 1SiHA powders; (b) Spray dried 1SiHA powders.

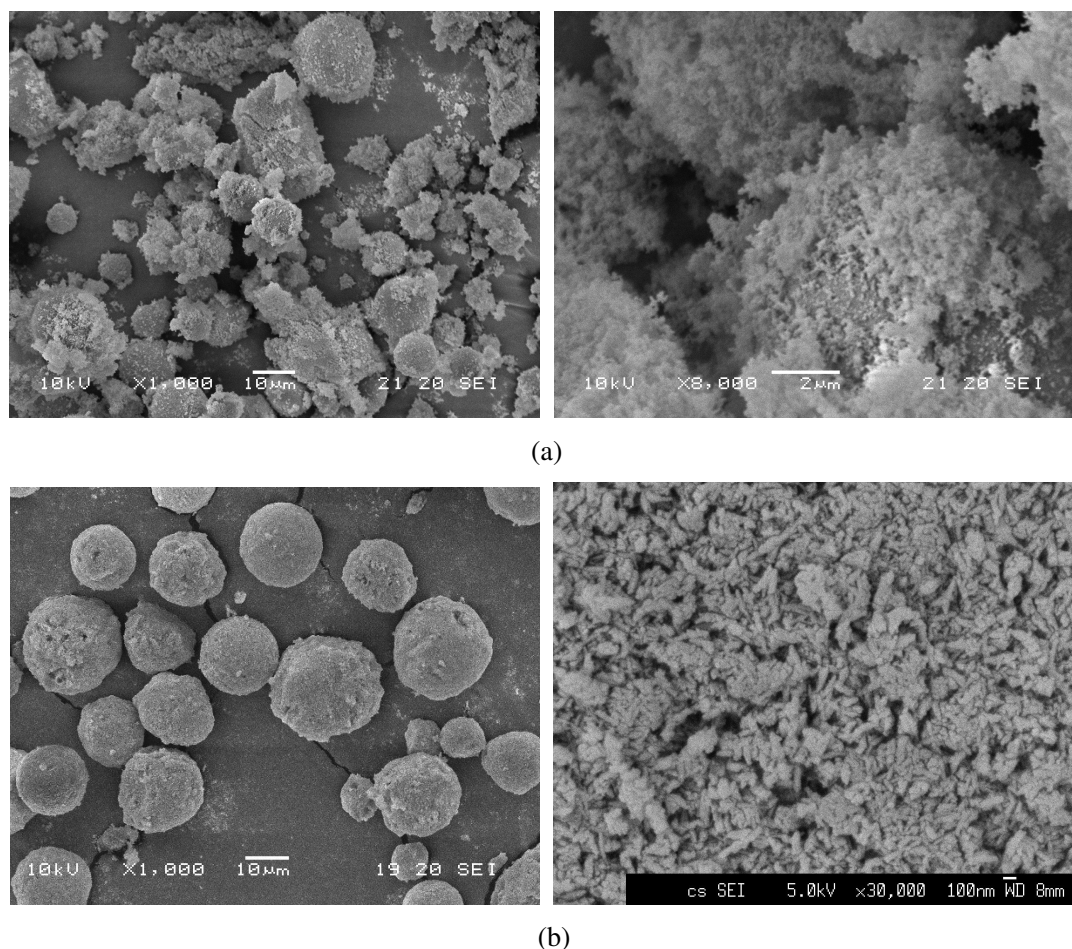


Figure 6.15 SEM images of the powders used for SPS processing:

(a) RF plasma processed prSi; and (b) spray dried p1SiHA.

Table 6.6 listed the particle size distribution of the prSi and p1SiHA. The prSi powders had relatively smaller particle size distribution than that of spray dried p1SiHA. The micron sized particles in RF plasma processed powders were mainly made of denser nano-structured material when compared with the relatively loose structure within the spray dried powders. The dense structure of prSi powders would result in the formation of the large inter-agglomerate pores in the green compact. The loose agglomerate in the spray dried powders could be destroyed during the formation of the compact.

Table 6.6 Particle size distribution of the r1SiHA and 1SiHA powders ($d_{0.1}$, $d_{0.5}$, $d_{0.9}$ refer to the measured particle size of 10%, 50% and 90% of the powder particles).

powders	$d_{0.1}(\mu\text{m})$	$d_{0.5}(\mu\text{m})$	$d_{0.9}(\mu\text{m})$
r1SiHA	3.98	12.09	28.73
1SiHA	6.01	17.41	37.81

Three measurements were averaged for each sample.

6.3.1.4 XPS analysis of silica doped CaP disks

The tetrahedral SiO_4^{4-} and PO_4^{3-} groups presented similar vibrations. It was very difficult to distinguish these similar structures by quantitative matching. Therefore, it was not definite whether the apparent fit to apatite indicated that this compound was actually present, or simply point to the presence of some intermediate material of similar structure.

Balas et al [117] used XPS to investigate the possible replacement of PO_4^{3-} by SiO_4^{4-} in silicon-contained apatite. In the current study, XPS was also applied to detect the replacement possibility of silicate and carbonate. Figure 6.16 showed the XPS wide scan of the elements present in powder sample of prSi and sintered SiHA disks. Ca 2p, Ca 2s, P 2s, P 2p, O 1s, C 1s and Si 2p were identified for all testing conditions.

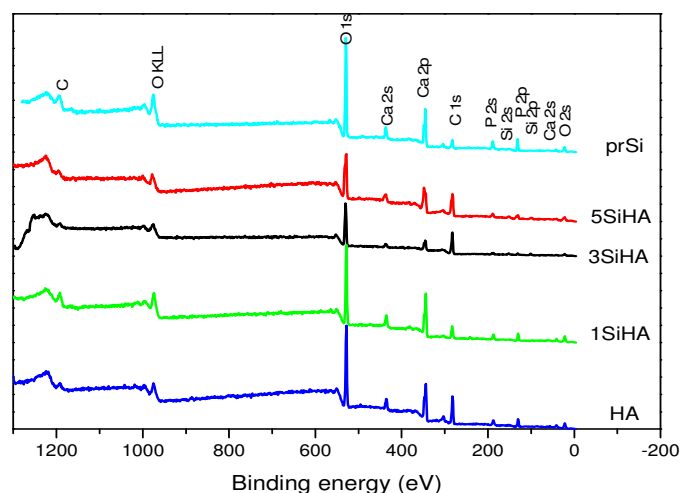


Figure 6.16 XPS spectra of SPS specimen sintered at 1000 °C for 3 min.

Typical narrow scanned XPS spectra of 3SiHA ceramic were presented in Figure 6.17. The P 2p peak was symmetric, which indicated that its binding energy was quite stable in apatite. It was referenced at 133.6 eV. The Ca 2p spectrum showed a doublet with Ca 2p_{3/2} at 347.5 eV and Ca 2p_{1/2} at 351.1 eV. The O 1s peak showed an asymmetry, and it was fitted using the peak deconvolution approach. It was decomposed into three components. The main component at 532.1 eV corresponded to the O linked only to a phosphorous atom as in PO₄³⁻ ions. The second at higher energy (534.0 eV) was attributed to Si-O peak. The lowest peak at 535.2 eV corresponds to C-O peak. The C 1s was deconvoluted to three peaks which correspond to aliphatic carbon atoms (284.5 eV), α -carbon atoms (285.6 eV) and carbonate (288.8 eV), respectively. The Si 2p spectrum had decomposed into 103.5 and 102.3 eV, with an area intensity ratio of 281.1 : 140.3 (about 2:1). As reported by Mekki et al [162], the binding energy of SiO₄⁴⁻ in sodium silicate was centered at 102.0 \pm 0.2 eV. According as peak of SiO₂ was centered at around 103.5 eV, the most intense component in the current specimen was assigned to amorphous Si-O₂. Thus the higher oxidation peak was attributed to silicon atoms belonging to isolated SiO₄⁴⁻. This analysis by XPS had been able to confirm conclusively that the silicon did exist as a tetrahedral silicate, SiO₄ group, in the SPS disks and RF plasma processed powders.

Table 6.7 listed the binding energies obtained from different compacts. These results indicated the substitution possibility of silicon in the phosphate position in the apatite structure after SPS and/or RF plasma processing. The presence of SiO₄⁴⁻ and carbonate corresponded to the enlargement of lattice parameters of apatite in the samples after SPS processing.

Table 6.7 Binding energies obtained from XPS of prSi and SiHA disks.

Samples	Ca 2p	O 1s	C 1s	Si 2p
HA	347.5	531.3	285.1	
	351.0	532.8	286.6	
1SiHA	347.4	531.1	285.0	102.3
	350.9	532.7	286.9	
		529.8		
3SiHA	347.5	532.1	284.5	102.3
	351.1	534.0	285.6	
		535.2	288.8	
5SiHA	347.2	531.2	282.3	101.4
	350.8	532.7	285.2	
			286.6	
prSi	347.2	530.9	284.5	102.1
	350.7	532.6	286.2	
			288.4	

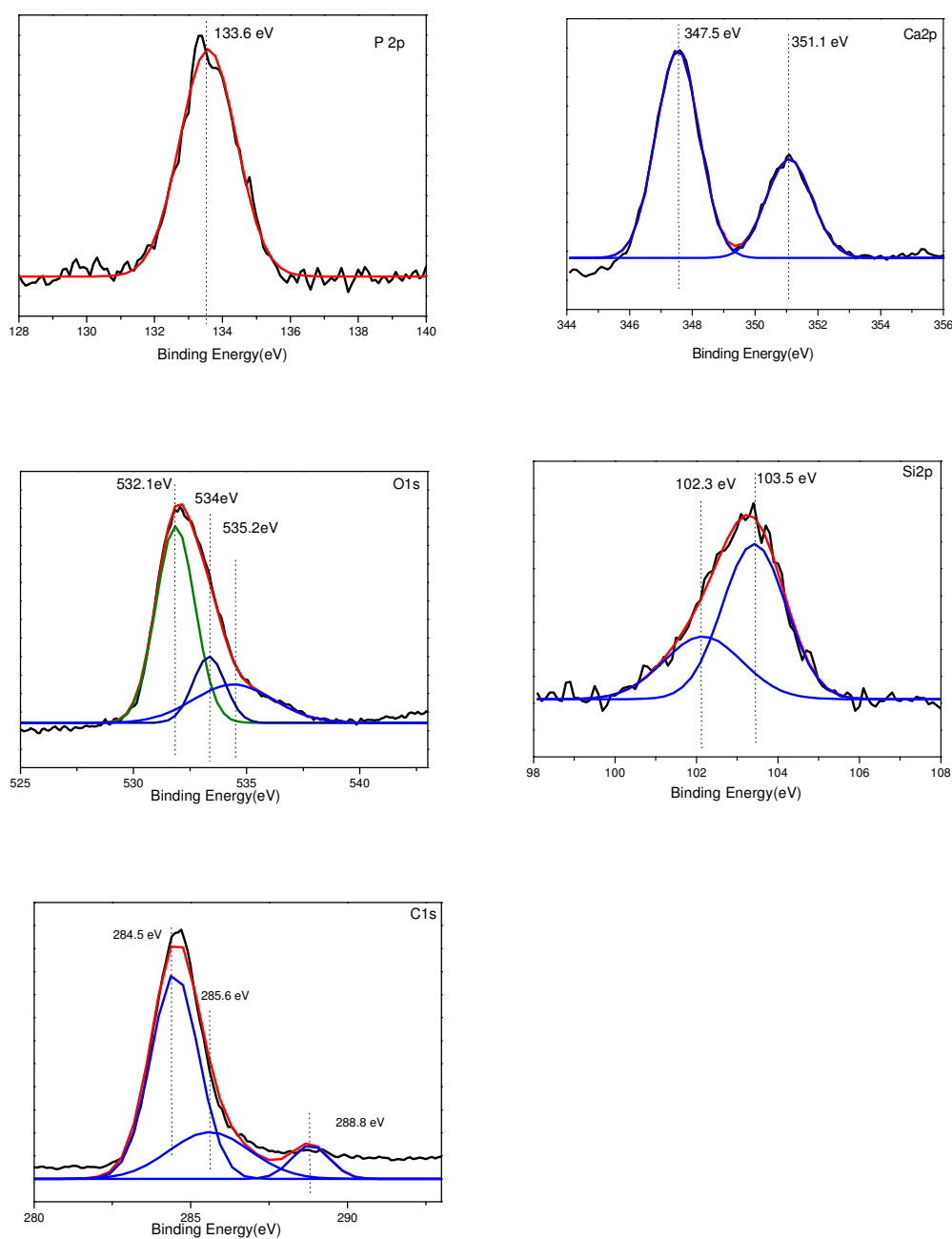


Figure 6.17 Binding energies of P2p, Ca2p, O1s, Si2p and C1s in 3SiHA ceramic.

6.3.2 Discussion

6.3.2.1 Sintering behavior analysis

As discussed previously, the spray dried powders were made of nano needle shaped particles. Before sintering, these nanometer sized powders were heavily agglomerated leading to two types of pores in the green body: intra-agglomerate pores (micron) and intercrystalline pores (nanometric) within the agglomerate (shown in Figure 6.18). During the sintering step, the elimination of the inter-agglomerate pores needed high temperatures that also encouraged grain growth, which was incompatible with the aim of keeping the sintered grain size in the nanometer regime. In this study, it showed that the initial sintering occurred within agglomerates or particle domains. The intra agglomerate pores first disappeared. Then the shrinkage of each agglomerate resulted in the growth of inter-agglomerate pores.

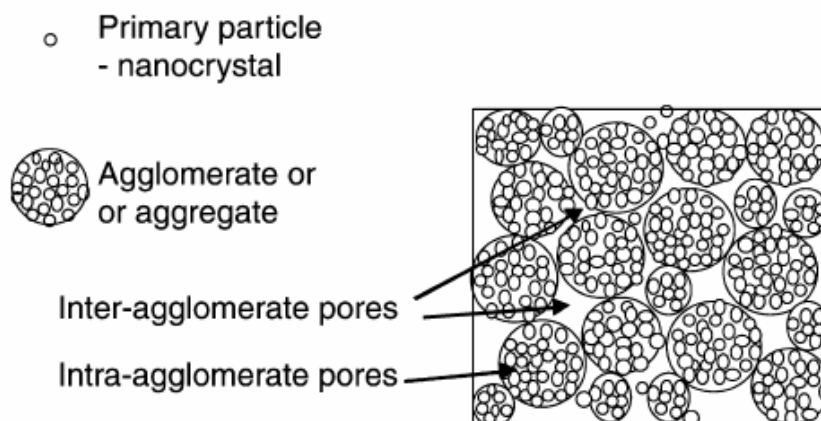


Figure 6.18 A schematic illustration of primary particles (nanocrystalline), an agglomerate and packing of agglomerates [163].

Further sintering led to the grain growth of sintered parts and the rearrangement between grains and pores. The pores reduced in size. They were eventually eliminated

in the second sintering stage, which were caused in the continuous electric current discharging process [164]. During this stage, local plastic deformation, near the inter-particle contacts, and/or uniform plastic deformation throughout powders occurred on unsteady heat flow conditions. At the final sintering stage, disappearance of isolated pores was caused by the mechanism of power law creep. The grain growth became a predominant phenomenon.

As observed in Figure 6.14, the densification of the spray dried powder started at lower temperature when compared with that of the RF plasma processed powders. This should be attributed to the high surface energy and loose nature associated with the spray dried powder. The intra-agglomerate pores would dominantly form in the spray dried powder. This type of pore was similar to the particle size, which could be readily eliminated at low sintering temperature. Since the low fraction of fine particles in the RF plasma processed powders, the inter-agglomerate pores in these denser particles would predominately control the sintering. Therefore, these pores could not be immediately removed, and needed to be sintered at higher temperature.

6.3.2.2 Phases analysis

As shown in Figure 6.10 (a), it was found that the presence of silica caused the decomposition of HA into β -TCP. Ruys et al [165] reported similar detection. They suggested the HA decomposition temperature was reduced from the usual range of ~1300 to 1400 °C down to ~750 to 1150 °C in the presence of the additives such as Al_2O_3 , SiO_2 and C. The reduction in decomposition temperature varied according to the composition of additives.

In this study, the amorphous precipitated silica did not form a strong chemical bond

with apatite, which became less stable due to the high temperature under the SPS process. The SPS process caused a localized increase in temperature, which introduced some liquid phase of silica. The presence of liquid phase would reduce interfacial energy, and promote the transformation of apatite phase to relatively unstable β -TCP phase. The presence of β -TCP increased susceptibility to slow crack growth, but its dissolution rate was very limited. Its presence would also improve the poor biodegradation characteristics of HA disks, and induce the natural bone ingrowth for extended periods without changing the osteoconductive properties of HA.

Both Raman spectra and changes in lattice parameters had indicated the silicon substituted possibilities in SiHA disks after SPS step. Investigation in XPS provided complementary information to prove the substitution possibility of silicate into phosphate positions. The role that the silicon substitution was playing on the sintering process of HA could be determined by considering the effect that sintering additives have on HA and the effect that other ionic substitution had on the sintering/densification of HA. The effects of a range of sintering additives on the sintering of HA have been reported [159]. Sintering additives, or aids, should be clearly separated from ionic substitution. This was because that they were typically as discrete second phase in the disks, as opposed to an ionic species that entered the crystal structure. Sintering aids, which were used to enhance the densification, were typically compounds with low melting points that promote liquid-phase sintering. Silica as sintering aids [159] in the traditional sintering of HA had proved to form liquid phase by the melting of this sintering aid. The fact that silicon was being substituted into HA might suggest that it could be feasible that silicon was actually forming a secondary phase. This secondary phase would behave as a sintering aid. From the composition of the SiHA samples, if any other secondary phase was

possible it would probably be a calcium silicate phase, which had a melting point above 1400 °C.

Considering the effect of other ionic substitutions on the sintering/densification of HA powders might provide a clear insight into the behavior observed with silicon substitution in the present study. The sintering of carbonate-substituted HA, where carbonate groups substituted for phosphate (B type) groups or phosphate and hydroxyl (AB type) groups, had been reported extensively [166]. All of these studies reported that the carbonate substitution had the effect of drastically reducing the sintering temperature required to achieve near full density by an order of 200-400 °C, when compared with HA. The carbonate substitution also had the effect of reducing the grain size of the final ceramic. The mechanism that described the enhanced sintering of these B type and AB type carbonate-substituted HA was probably a combined factor of increased vacancy concentration due to the substitutions. In contrast, however, where carbonate substituted for only hydroxyl groups, A type, there was no difference in the sintering behavior compared with stoichiometric HA [167]. The A type substitution did not generate the same number of vacancies as B type or AB type. It limited the mobility of OH groups that were instrumental in the densification, and thus reduced the sintered densities of the obtained disks.

In the present study, Raman spectra, lattices parameters and XPS results had proved that B type silicon substituted possibilities in SiHA disks after SPS step. But the vacancies in hydroxyl site must be introduced to maintain charge balance, while no cation vacancies were introduced. Therefore, the hydroxyl groups in SiHA interacted more strongly with the calcium or silicate groups as compared with HA disks. Thus, the mobility of the hydroxyl groups in SiHA would be improved. Dense

disks could be produced when a high enough sintering temperature was reached. However, it should be considered that the HA might decompose into other calcium phosphates at high processing temperature.

6.4 Chapter summary

In this chapter, the sintering properties of RF plasma processed and spray dried powders using a SPS system were investigated and discussed. The results demonstrated that RF plasma processed powders were effectively sintered to high densities with enhanced bio-mechanical properties through the SPS system. The presence of silica in the disks introduced decomposition of HA into other phases after sintering. Raman spectra, lattice parameters and XPS results proved that there were about 1/3 of silicate substituted into the phosphate position in the obtained SPS disks and RF plasma processed prSi powders. The powder morphology and the aggregation were the main factors controlling sintering behavior. The characteristics developed by agglomerates were closely related to the powder processing techniques.